A Protease-initiated Model of Wound Detection

By

James Thomas O'Connor

Dissertation

Submitted to the Faculty of the

Graduate School of Vanderbilt University

in partial fulfillment of the requirements

for the degree of

DOCTOR OF PHILOSOPHY

in

Cell and Developmental Biology

February 28, 2022

Approved:

Andrea Page-McCaw, Ph.D.

Matthew Tyska, Ph.D.

Ian Macara, Ph.D.

Jared Nordman, Ph.D.

M. Shane Hutson, Ph.D.

This is why science and mathematics are so much fun:

you discover things that seem impossible to be true,

and then get to figure out why it’s impossible for them not to be.

- Vi Hart

Acknowledgements

First, I want to acknowledge that, while my name may be alone on the front of this dissertation, it would not have been possible without the combined efforts of everyone that has contributed to this project over the past few years. This project's success is not a result of my work alone, but also work from Erica Shannon, Aaron Stevens, Bushra Akbar, Kimi LaFever Hodge, James White, Ivy Han, Jasmine Su, Neil Narayanan, Ty McCleery, Hannah Kim, Lila Nassar, Wes Edrington, Casey Gailey, Lilia Merbouche, and Elizabeth Ruark. This truly collaborative project could never have been completed by a single person, and each of these scientists contributed extremely valuable time and effort, without which this story would not exist. I especially want to thank Erica, for laying the foundations, Bushra, for performing many of the most crucial experiments of this entire project, and James W., Ivy, and Jasmine for ensuring this project continues even after I finish.

I want to thank Andrea Page-McCaw, for being the best mentor I could have asked for. She exemplifies the best aspects of a scientist: enthusiasm, curiosity, and an unparalleled willingness to collaborate and share ideas and information. She has never treated her students as merely subordinates, but as colleagues, always eager to hear their perspectives and ideas. Most importantly, she believed in my abilities as a scientist long before I did myself.

I want to thank Shane Hutson for his co-mentorship. Throughout graduate school, I have continually recounted how lucky I have been to have not one, but two supportive PIs that have taught me so much. The continued collaboration between the Page-McCaw and Hutson labs has been inspiring to me and exemplary of what I feel science should be like.

I want to thank all the members of my committee, Matt Tyska, Ian Macara, Jared Nordman, and Shane Hutson, for continually listening, steering my project in the right direction, giving actionable feedback, and giving me confidence in the value and impact of my data.

I want to thank all of my other mentors along the way. To Mr. Jazak and Mrs. Barton, my high school biology teachers, who first helped me to see biology, not as random terms that needed memorizing, but as real processes happening inside of each of us every single moment. To Basilia Zingarelli, Paul Urayama, and Ann Hagerman, my first PIs, who gave me the introduction to lab science that propelled me forward to become the scientist I am now.

I want to thank all the members of the Page-McCaw lab, especially James W., Kimi, and Indrayani who have been with me for the majority of my time here, your friendship and support me have kept me sane throughout this journey. Thank you so much for always being there for me (and for putting up with me).

I want to thank my mom and dad, for believing in me, for supporting me, for constantly reiterating that there is no limit to what I can accomplish, and for loving me unconditionally, even when I fail. I want to thank my brother Andrew for constantly pushing me to be better, and instilling in me a passion to never give up and to always improve.

Finally, I want to thank Yannan Huang, the most incredible person I know. I cannot thank you enough for supporting me, through all of the ups and downs of grad school, from awards and publications to late nights spent in the lab. Even while you are away in medical school facing your own battles, you still find the time to help me with mine. I am constantly inspired by your beauty, intelligence, and passion to accomplish every one of your goals. You make me strive to be better, every single day. Thank you.

TABLE OF CONTENTS

	Page
Dedication	ii
Acknowledgements	iii
List of Tables	vi
List of Figures	vii
List of Abbreviations	viii
Chapters	
1. Introduction	1
Mechanisms of cytosolic calcium increase	2
Additional cytosolic calcium modulators	5
Wound-induced cytoskeletal reorganization	5
Damage-Associated Molecular Patterns and Downstream Damage Responses	6
Vertebrate and invertebrate wound repair	8
2. Drosophila pupal case dissection for laser ablation and live imaging of the notum	11
Summary	11
Preparations	12
Preparation one, Method one – Staging the pupae	12
Preparation one, Method two – Staging the pupae	14
Step-by-step Method Details	14
Major step one – Removing pupae from the vial	14
Major step two – Dissecting the pupal case	17
Major step three – Mounting the dissected pupae	20
Major step four – Wounding and live imaging the pupae	24
Troubleshooting	27
Chapter 2 Figure	
3. Zones of Cellular Damage Around Pulsed-Laser Wounds	31
Abstract	31
Introduction	32
Results	35
Discussion	41
Conclusions	46
Chapter 3 Main Figures	48
Supporting Information	54
4. Proteolytic activation of Growth-Blocking Peptides triggers calcium responses through the GPCR Mthl10 during epithelial wound detection.	55
Abstract	55
Introduction	56
Results	57
The distal calcium response signals to release calcium via IP_3	58
The distal calcium response requires the GPCR Mthl10	60
Mthl10 is activated by Gbp1 and Gbp2	61
Gbps and Mthl10 are required for calcium waves in wing discs	63
Gbps are activated by multiple proteases	64

Enzymatic generation of a diffusible signal explains wound-size dependence 64
Computational model identifies key role for cell lysis over time 68
Discussion 70
Two superimposed mechanisms increase cytoplasmic calcium around wounds 71
Other upstream regulators of wound-induced calcium 72
Functions of the Gbp/Mthl10 induced calcium increase around wounds 74
Limitations of the Study 75
Chapter 4 Main Figures 78
Supporting Text 90
Reaction-Diffusion Model of the Distal Calcium Response 90
Chapter 4 Supplemental Figures 108

5. Additional modulators of wound-induced calcium signaling 116

Introduction 116
PLCβ Overexpression Alters Calcium Responses 117
SERCA, STIM, and PMCA Modulate the Calcium Response 117
Mechanosensitive Ion Channels Are Not Required for the Calcium Response 119
Mechanosensation May Play a Sensitizing Role in the Calcium Response 120
Conclusions 121
Chapter 5 Figures 123

6. Wound-induced changes in cytoskeleton and epithelial tension 126

Introduction 126
Myosin localization rapidly changes after wounding 127
Myosin relocalization is correlated with increases in cytosolic calcium 127
Discussion 128
Chapter 6 Figures 130

7. Additional downstream wound responses 133

Introduction 133
Wounding induces cell cycle changes in cells proximal to the wound 133
Multinucleate syncytial cells form after wounding 134
Immune cells infiltrate the wound site in a Gbp-independent manner 135
Chapter 7 Figures 137

8. Discussion 143

Timeline of *Drosophila* pupal wound responses 143
Calcium signaling dynamics and roles 146
Damage-induced activation of proteases 147
Comparisons to human wound repair 149
Summary and future studies 150

Materials and Methods 152

Drosophila melanogaster husbandry 152
Method details 156
Quantification and statistical analysis 162

References 168

LIST OF TABLES

Page

1. Source flies obtained for these studies 152

2. Complete genotype for each figure panel. 154

LIST OF FIGURES

Page

Chapter 2, Figure 1: Calcium signaling data obtained after wounding using this methodology 30

Chapter 3, Figure 1: mCherry.NLS reports nuclear envelope integrity 47
Chapter 3, Figure 2: Several zones of damage are evident around pulsed-laser wounds. 48
Chapter 3, Figure 3: Histones reveal that within the region of nuclear membrane damage, some nuclei have intact chromatin whereas nuclei closer to the center have disrupted chromatin. 49
Chapter 3, Figure 4: Cell borders are disrupted following wounding 50
Chapter 3, Figure 5: The first expansion of calcium extends about 20 μm from the region of plasma membrane damage, independent of wound size. 51
Chapter 3, Figure 6: Each zone of damage can be estimated given one of them. 52
Chapter 3, S1 Figure: Some cells with nuclear membrane damage recover. 53
Chapter 3, S2 Figure: The region of Ecadherin loss expands over 90 minutes. 53

Chapter 4, Figure 1. Wounds trigger calcium release via the G_q pathway. 78
Chapter 4, Figure 2: The distal calcium response requires the GPCR Methuselah-like 10 (Mthl10). 80
Chapter 4, Figure 3: The distal calcium response requires either Gbp1 or Gbp2. 81
Chapter 4, Figure 4: Gbp peptides and *Drosophila* extracts elicit calcium responses in wing discs through Mthl10. 83
Chapter 4, Figure 5: *Drosophila* extract and proteases require Gbps to elicit calcium responses. 84
Chapter 4, Figure 6: Reaction-diffusion (RD) model for epithelial wound detection. 85
Chapter 4, Figure 7: Reaction-diffusion (RD) model predictions and experimental validations. 87
Chapter 4, Figure S1: Wounds signal calcium to proximal cells through gap junctions and to distal cells through IP_3. 108
Chapter 4, Figure S2: Gbps 4 and 5 are also sufficient to elicit calcium responses in wing discs. 109
Chapter 4, Figure S3: Results of simultaneously fitting the reaction-diffusion model to four selected experimental samples. 110
Chapter 4, Figure S4, related to Figure 6: Results of fitting the reaction-diffusion model to four selected experimental samples. 111
Chapter 4, Figure S5: Parameter variation effect on RD model output. 112
Chapter 4, Figure S6: Radial analysis of calcium signaling. 113

Chapter 5, Figure 1. PLC Overexpression increases the cellular calcium response 123
Chapter 5, Figure 2. Various calcium modulators change the wound-induced calcium response. 124
Chapter 5, Figure 3. Cortical tension modulator SqhEE sensitizes cells to the distal calcium response 125

Chapter 6, Figure 1. The wound-induced actomyosin pursestring forms independently of Gbp1 and Gbp2. 130
Chapter 6, Figure 2. Wounds cause relocalization of myosin 131
Chapter 6, Figure 3. Cell contraction occurs in tandem with increased calcium fluorescence. 132

Chapter 7, Figure 1. Cells proximal to the wound preferentially enter G2/M phase of cell cycle during wound repair 137
Chapter 7, Figure 2. Cells proximal to the wound undergo cell-cell fusions to become giant multinucleate syncytia. 138
Chapter 7, Figure 3. Syncytia formation is increased in larger wounds. 139
Chapter 7, Figure 4. Types of *srp*- expressing cells visible 6 hours after wounding. 140
Chapter 7, Figure 5. Δ*Gbp1,2* does not noticeably affect the wound-induced immune response. 141

LIST OF ABBREVIATIONS

- “Calcium” in this study always refers to calcium ions, Ca^{2+}
- Mthl10 = methuselah-like 10
- Gbp = Growth-blocking peptides
- IP_3 = inositol 1,4,5-trisphosphate
- PLCβ or PLC21C = Phospholipase C beta
- SERCA = sarcoplasmic/endoplasmic reticulum Ca2+-ATPase
- PMCA = plasma membrane calcium ATPase

CHAPTER 1

INTRODUCTION

When an organism is injured, the damaged tissue rapidly responds to repair the injury and restore proper functionality. Epithelial tissue, which separates the inside of the body from the outside world, acts as a barrier to keep the body intact and to keep pathogens out[1]. The epithelial barrier is the body's first line of defense against environmental threats making it especially vulnerable to damage. As such, epithelial cells have evolved to respond to the damage that will inevitably occur. When epithelial tissue is damaged, the cells transition from a stationary and quiescent state to a migratory or proliferative state to restore barrier function, preventing infection or excess blood loss[2–5]. To properly respond to injury, cells surrounding a wound must sense the damage and transduce the signaling pathways that result in repair. What is the main cellular information received to initiate wound repair? Are there any universal wound signaling pathways that are consistently activated by multiple different kinds of damage? And what downstream responses are carried out by the cell to ensure proper and complete wound repair?

The earliest conserved response in cells around a wound is a dramatic increase in cytosolic calcium that propagates outward from the wound site to surrounding cells[6–17]. In epithelial tissue, this calcium signaling begins within seconds of damage, informing surrounding cells that a wound has occurred and leading to downstream wound responses[6–10]. Because an increase in cytosolic calcium is rapid, conserved, and necessary for the wound response, it has been recognized as a critically important wound-induced signal[7,8,15–17]. For this reason, calcium signaling in the early response to wounds has been well-studied in a variety of model organisms for many years, but the research has often led to seemingly conflicting data about the wound-induced initiators of calcium signaling and the role calcium plays in the downstream wound

responses. This dissertation will synthesize the current literature with my own research on calcium signaling in the early response to wounds to parse the variety of known initiators of cytosolic calcium signaling and the numerous wound response pathways calcium has been found to impact.

Mechanisms of cytosolic calcium increase

Calcium is maintained at approximately 10,000-fold lower concentration in the cytosol than in either the extracellular space or intracellular stores such as the endoplasmic reticulum (ER)[18,19], meaning mechanisms for cytosolic calcium entry sit on a hairpin trigger for activation; allowing calcium entry from either the extracellular space or intracellular stores will cause a rapid and dramatic change in cytosolic calcium concentration. Accordingly, the entry points for calcium into the cytosol are tightly regulated and multiple mechanisms exist to actively pump calcium out of the cytosol to maintain this dramatic concentration gradient. Broadly, there are four potential methods for an increase in cytosolic calcium: 1) direct entry from extracellular space through plasma membrane damage, 2) entry from extracellular space through ion channels, 3) release from the endoplasmic reticulum through the IP_3 Receptor or ryanodine receptor, and 4) entry from neighboring cells through gap junctions.

1) A breach in the plasma membrane allows extracellular calcium to rush into the cytosol directly. This is often associated with damage to a single cell, such as a Xenopus oocyte that is injured severely enough to have membrane rupture, but not severely enough to be completely destroyed[20,21]. However, damage to a multi-cellular tissue can also cause extracellular calcium influx directly through plasma membrane damage after wounding via mechanical perturbation[22], scratching[13], or pulsed-laser ablation[14]. In the latter case, pulsed-laser ablation creates a cavitation bubble that expands and contracts on the order of microseconds, causing shear stress along the tissue resulting in a variety of cellular damage, including plasma membrane

micro-tears[14,23,24]. The damage created to tissues by pulsed-laser ablation is explored further in Chapter 3.

2) A more common method of extracellular calcium entry into the cytosol is through plasma membrane calcium ion channels. These channels are numerous and diverse, allowing for a variety of gating mechanisms for the cell to more precisely control calcium entry. Calcium-specific ion channels can be voltage-gated (as in the Ca_v channels)[25], ligand-gated (as in the 5-HT_3 receptor channel[26], mechanically-gated (as in Piezo)[27–29], or gated-by protein-protein interactions (as in Orai)[18,30,31]. Perhaps even more notable are the Transient-receptor potential (TRP) ion channels that, while not specific to calcium, play a very important role in gated calcium entry into the cytosol upon a variety of extracellular stimuli, including voltage, ligands, light, taste, pain, temperature, and mechanical change[32–36]. The diversity of the TRP channels accentuates the versatility of calcium in a variety of important cell responses. In response to wounding specifically, TRPm has been well-studied as a potential initiator of extracellular calcium entry in response to damage. Previous studies have shown that TRPm is required for proper calcium signaling after wounding, with knockdown of TRPm impairing (though not eliminating) the wound-induced calcium signaling, leading to a decreased cytoskeletal repair response and decreased inflammatory response[6,7]. The claims of TRPm significantly impacting wound-induced calcium signaling are explored further in Chapter 4.

3) The most common method for calcium release from intracellular stores into the cytosol is through the IP_3 Receptor on the endoplasmic reticulum, which is activated by Inositol 1,4,5-trisphosphate (IP_3)[37,38]. The canonical pathway for IP_3 creation is as follows: an extracellular ligand binds to a G-protein coupled receptor (GPCR), which activates the alpha subunit of the Gq protein, activating Phospholipase C beta (PLCβ) to hydrolyze Phosphatidylinositol 4,5-bisphosphate (PIP_2) into IP_3, which binds to the IP_3 Receptor (IP_3R) on the ER leading to a release of calcium into the cytosol[37–40]. The Gq signaling cascade has been well studied in the context of wounds. Multiple previous studies have implicated the Gq-pathway

in wound-induced calcium signaling[9,13,16,17,41,42], though the identity of the GPCR and ligand remains somewhat elusive. One favored hypothesis is the diffusible ligand is ATP, released from wounds, activating a calcium response through P2Y GPCRs[13,17,43], though this response is conserved in animals lacking P2Y receptors (such as *Drosophila*). Another candidate is the calcium-sensing receptor (CaSR), which was shown to promote a wound-induced intracellular calcium response to promote keratinocyte adhesion, differentiation, and survival in mice[16]. Further study of the GPCR/Gq signaling pathway in response to wounding, is described in Chapter 4.

This well characterized Gq-signaling cascade also produces other 2nd messengers besides IP_3 and calcium–diacylglyceride, for example, which is produced in the hydrolysis of PIP_2 into IP_3, stimulates activation of protein kinase C, which acts as a vitally important kinase for a variety of calcium dependent cellular behaviors[37,39,44,45]. Additionally, a similar signaling cascade can be initiated by receptor-tyrosine kinases (RTKs), which activate Phospholipase C gamma (PLC γ) to create IP_3 and DAG in a similar manner to Phospholipase C beta (PLCβ)[46,47]. ER calcium release can also occur through the ryanodine receptor, which is more often associated with calcium signaling in the brain and muscle through release from the sarcoplasmic reticulum[48,49], but has recently shown to potentially play a role in barrier homeostasis and wound healing[50,51]. Further study of wound-induced ER calcium release is described in Chapter 4.

4) Gap junctions are known to play a role in propagation of calcium signaling throughout a tissue, but this often does not occur by calcium travelling directly through gap junctions. In general, IP_3 is more transmissible through gap junctions than calcium[52–54], causing one cell to activate a calcium response by IP_3-mediated ER calcium release, followed by junctional transmission of IP_3, leading to a new IP_3-mediated ER calcium release in the neighboring cell[55,56]. This leads to propagation of calcium signaling in a tissue, though not by calcium itself diffusing. In fact, a dramatic increase in cytosolic calcium is known to close gap junctions,

uncoupling cell-cell communication[55]. However, in other cases, cytosolic calcium can overcome this decreased transmissibility and diffuse to neighboring cells through gap junctions[57,58]. In the context of a wound, calcium waves have been shown to travel from cell-to-cell through gap junctions, even in contexts where IP_3 is not produced, demonstrating that wound-induced calcium can diffuse from one cell to a neighbor[13,14].

Additional cytosolic calcium modulators

Once cytosolic calcium is increased, the cell rapidly attempts to modulate this calcium signal by returning the cell to its homeostatic state, either by pumping calcium back into the ER or out into the extracellular space. For example, after calcium release from the ER, the sarco/endoplasmic reticulum Calcium-ATPase (SERCA) pump actively works to transport cytosolic calcium back into the ER[59,60]. Meanwhile, both plasma membrane Calcium ATPase (PMCA) and the sodium/calcium exchanger (NCX) send cytosolic calcium out into the extracellular space[61–63]. After an IP_3R-mediated calcium release from the ER, some calcium is inevitably lost to the extracellular space due to action from PMCA and NCX before all calcium can be pumped back into the ER through SERCA. If this were to occur multiple times, the ER would soon become depleted of calcium. To prevent this, the protein STIM senses when the ER calcium concentration is low and opens the ion channel Orai, allowing some extracellular calcium back into the cytosol to prevent ER calcium depletion[18,31]. In this way, the cellular proteins work in harmony to modulate cytosolic, organelle, and extracellular calcium levels to maintain calcium concentration homeostasis. These calcium modulators are explored in greater detail in Chapter 5.

Wound-induced cytoskeletal reorganization

Upon injury, the epithelial cells around the wound sense the severity and location of the damage and change their behavior to repair it. This includes migrating inwards to fill in the

wound and dividing to replenish the cells lost to the wound. Migration requires force, often associated with a dynamic change in the tissue cytoskeleton, leading to relocalization of actin and myosin into a pursestring to cinch the wound closed[6,64–68], and into filopodia/lamellipodia to aid in migratory crawling[67–69]. In general, the pursestring cinches multicellular wounds mostly shut, at which point filopodia reach across to filopodia on the opposite side to seal the remaining portion of the wound closed; the activity of the small GTPase Rho is required for pursestring formation while the small GTPase cdc42 is required for filopodia formation, and absence of either GTPase slows wound repair[67,68]. Intracellular calcium is a known modulator of GTPases[70], and has been shown to be upstream of GTPase activity leading to actomyosin pursestring formation after wounding in Xenopus oocytes[20,71]. Thus, it makes sense for wound-induced calcium signaling to act upstream of GTPases to relocalize actin and myosin into filopodia or pursestrings to aid in repair. Additionally, calcium has been found to stimulate the formin INF2, which leads to depolymerization of cortical actin and polymerization of f-actin near the ER, dramatically restructuring cellular actin in less than one minute, in what has been termed a "calcium-mediated actin reset"[72]. Each of these studies show calcium as a vital upstream regulator of actin and myosin dynamics in the first minutes after wounding, leading to a model that calcium is important for rapid cytoskeletal restructuring that allows for proper wound repair.

Damage-Associated Molecular Patterns and Downstream Damage Responses

Beyond simply calcium and cytoskeletal regulators, there are a number of molecules that are commonly found in the extremely early stages of wound repair, that may act upstream, downstream, or completely independently of cytosolic calcium. These include ATP[13,17,43,73], reactive oxygen species[7,11,74,75], nitric oxide[76,77], and damage-associated molecular patterns (DAMPs) that are, as the name suggests, molecules regularly associated with damage that act to promote a wound response[78,79]. More technically, DAMPs constitute molecules secreted by dead/dying cells to trigger an epithelial or immune damage response while "alarmins" are

molecules secreted by living cells near wounds to do the same thing[80]. DAMPs and alarmins can be a variety of molecules, from proteins such as high-mobility group box protein-1 (HMGB1) that can activate an immune response[81,82], and induce cell migration[83], proinflammatory cytokines such as Interleukin-1 alpha (IL1α) that acts as a potent immune cell chemoattractant following wounding[84,85], or S100s that are known calcium-binding proteins that can increase potent antimicrobial activity and activate NADPH Oxidase to produce reactive oxygen species[86,87].

In contrast to most DAMPs, reactive oxygen species (ROS) such as O_2^{-}• or H_2O_2 are much simpler molecules, but still very important for the wound response. ROS are most often associated with deleterious effects, such as increased aging or cancer[88,89]. However, ROS can also elicit potent inflammatory responses that recruit immune cells to the wound[7,90] and can lead to targeted cell death that is important for destroying damaged cells no longer fit to survive[75]. Interestingly wound-induced ROS has been shown to be released from the mitochondria in a calcium dependent-manner after uptake of cytosolic calcium into the mitochondria through the mitochondrial calcium uniporter (MCU)[74], or created by the NADPH Oxidase DUOX that also requires an increase in cytosolic calcium[7,11]. In both cases, the reactive oxygen species play a crucial role in the inflammatory response, and wound healing in general, as a downstream response to increased cytosolic calcium immediately after wounding.

In addition to activating ROS to induce a proinflammatory wound response, calcium has also been shown to activate cytosolic phospholipase A_2 ($cPLA_2$) after zebrafish tailfin injury, which creates proinflammatory eicosanoids that also act as chemoattractants for immune cells to the wound site[8,91]. This process was shown to be calcium dependent, and occurs as a direct result of cellular and nuclear swelling leading to an interesting conclusion that $cPLA_2$ activation (and potentially wound-induced calcium signaling itself) occurs in a mechanosensitive manner[8]. As mentioned above, extracellular calcium entry into the cytosol can occur through a mechanosensitive ion channel such as Piezo or certain TRP-channels, or perhaps if the

mechanical stress were severe enough to disrupt the plasma membrane's impermeability and cause microtears. Additionally, calcium is necessary but not sufficient to activate $cPLA_2$ without mechanical stress[8], meaning other methods of cytosolic calcium increase not accompanied my mechanical stress may not be able to properly activate $cPLA_2$. This is just one example of how a single signaling ion, calcium, may yield certain downstream responses in some instances but not others.

It is apparent that wound-induced calcium does not initiate a single downstream wound response, but many, likely simultaneous, wound response pathways. Though these pathways may diverge from a single signaling ion, calcium, their eventual goal converges on induction of epithelial migration/proliferation and/or recruitment of immune cells to the wound site to clear debris and fight potential infection. One well-studied pathway that is required for a variety of cellular responses is c-Jun N-terminal Kinase (JNK) pathway. JNK is required for proper wound repair[92,93], and is activated after injury in both epithelia to promote survival through polyploidization and cell cycle stalling in G2-phase[94,95] and in astrocytes to upregulate glial fibrillary acidic protein and modulate glial scarring, the latter of which was shown to be in a calcium-dependent manner[96]. Another well-known wound/pathogen response pathway is the Toll/NFκB pathway (TLR pathways in mammals), which is perhaps the most important pathway in the upregulation of inflammatory cytokines, immune response genes, and in the production of antimicrobial peptides[97–99]. Toll is activated by the ligand spätzle after proteolytic cleavage from a pro-peptide form into an active form[98–101]. Interestingly, both serine proteases and intracellular calcium are able to activate the Toll pathway, leading to wound response genes, with DUOX and ROS acting as likely intermediates between calcium and spätzle activation[102,103].

Vertebrate and invertebrate wound repair

Wound repair is significantly more complex in mammals than in invertebrates. Mammalian skin not only has multiple different epithelial layers and cell types, but also a more

intricate immune system and a highly complex vasculature. Nevertheless, the cell types and behaviors involved in human skin wound repair have been well characterized[4,5,104,105]: briefly, destroyed epithelial cells release DAMPs, while nearby wounded epithelial cells experience an increase in cytosolic calcium and release of alarmins; exposed blood vessels and platelets initiate the coagulation cascade, forming a blood clot at the wound site[106–108]; the DAMPs and alarmins recruit leukocytes, namely circulating neutrophils and resident mast cells, to the wound site, where they secrete more proinflammatory cytokines and ROS to recruit more neutrophils and macrophages to fight off invading pathogens and clear debris; fibroblasts activate and differentiate into myofibroblasts to rapidly secrete and deposit new extracellular matrix[109]; epithelial cells begin to migrate and proliferate under the scab to fill in the wound, with mouse models indicating the cells nearest the wound margin mostly migrate while cells slightly more distal from the wound margin proliferate[110]; the wound resolves with properly formed epithelial layers (though usually thickened at the former wound site) and the dried scab/eschar falls off; a fibrotic scar of imperfect extracellular matrix may remain; leukocytes and myofibroblasts undergo apoptosis after they are no longer needed.

While the description of mammalian wound repair is very detailed on a clinical level, there are still unanswered questions about the molecular mechanisms of each step, including how to get wounds to heal faster, how to regenerate tissue that has failed to heal, and how the cellular behaviors of wound repair (migration, proliferation, and inflammation) properly terminate given those same behaviors are dysregulated in deadly diseases such as cancer. To answer these questions, it is advantageous to employ a model organism that can be genetically manipulated, reproducibly injured, and extensively monitored. For this reason, this project has used the *Drosophila* pupa as its model organism. *Drosophila* are genetically tractable, with genetically-expressed fluorescently-tagged versions of a variety of proteins, the *Gal4/UAS* system allowing for tissue specific gene expression, and inducible knockdowns of nearly every gene publicly available[111]. Specifically, the pupa is extremely useful because it is stationary for

multiple days[112], with a monolayer epithelium easily accessible through a simple dissection that allows for laser wounding and simultaneous live imaging of wound signaling and the entirety of the closure process (See Chapter 2). Furthermore, although many of the same cellular behaviors that occur in mammalian wounds are conserved, there are far fewer relevant cell types (namely epithelial cells comprising a single monolayer, hemocytes, and fat body cells) to monitor in order to glean a relatively complete understanding of the *Drosophila* pupal wound response. In this way, this dissertation seeks to expand on the work of Erica Shannon[14] to give a complete understanding of the upstream initiators and downstream responses of cytosolic calcium signaling in *Drosophila* pupal wounds.

CHAPTER 2

DROSPHILA PUPAL CASE DISSECTION FOR LASER ABLATION AND LIVE IMAGING OF THE NOTUM

This chapter is adapted from: O'Connor, JT., Shannon, EK., Hutson, MS., Page-McCaw, A., Drosophila pupal case dissection for laser ablation and live imaging of the notum. *Star Protocols* (in review)

SUMMARY

This protocol demonstrates how to remove the pupal case to image the pupal notum (dorsal thorax) in vivo. This technique is amenable to laser wounding and simultaneous imaging for the entire duration of the pupal stage. This is especially useful for pupae expressing genes in the domain of pnr-Gal4, in the center of the notum, because it allows for comparison of control and experimental regions. When ablation is targeted at the border of gene expression, the symmetry of the wound response can be monitored in the control and experimental domain. For complete details on the use and execution of this protocol, please refer to O'Connor, et al[113].

Before You Begin

The protocol below describes specific steps using pupae with the following genotype, but could be used for Drosophila of any genotype:

ActinP-GCaMP6m / + ; pnr-Gal4, UAS-mCherry.NLS, tubP-Gal80^{TS} / +

This genotype will yield pupae with the calcium indicator GCaMP6m expressed ubiquitously, and the red nuclear marker mCherry.NLS expressed in the hourglass shaped pnr domain under conditional temperature-sensitive control. In (O'Connor et al., 2021)[113], *UAS-RNAi* lines were crossed into this system to knock down genes of interest exclusively in the experimental *pnr*-domain while maintaining an adjacent internal control. To inactivate Gal80^{TS} and activate *UAS*-mediated gene expression, the experimental samples were kept at 29°C for 4-5 days before

experimentation. Note the time reported in Preparation one is at 29°C, and therefore the pupae will age faster than if kept at a lower temperature.

PREPARATIONS

Preparation one, Method one – Staging the pupae. Timing: [1–6 hours before]

Rationale: Staging the pupae is necessary to get reproducible results. In this protocol, we aim to experiment exclusively on pupae between ~12–18 hrs after puparium formation (APF) at 29°C. At 12 hrs APF, the pupal head everts and the pupa is no longer "liquidy", and thus can survive without its case. At 18 hrs APF, the notum no longer lies as flat against the cover slip, and the thoracic bristles begin to be visible, potentially obscuring imaging. Staging is important because pupae look similar by eye between 12 and 48 hrs APF at 29°C, and therefore are difficult to identify.

Need: Dissection scope, marker, vial of 3rd instar larvae or pupae.

1. Under a dissection scope, identify and classify each pupa in a vial according to three categories:
    a. White prepupae, 0-1 hrs APF at 29°C, P1–P2 (Bainbridge and Bownes, 1981)[112], which are white like 3rd instar larvae, but have become stationary and have everted anterior spiracles. Mark the outside of the vial where the white prepupa is adhered using a permanent marker to make a small identifying mark, such as a "/".
    b. "Liquid" pupae, 1–12 hrs APF at 29°C, P2–P4, where the outside case has turned brown. Inside the case, the pupa is fragile and appears almost entirely liquified. Mark the outside of the vial for these pupae with a second identifying mark, such as an "X".

c. “Solid” pupae, 12+ hrs APF at 29°C, P4(ii) onward, where the head of the pupa has everted and the body has solidified. A small gap has appeared between the head of the pupa and the anterior spiracles. Mark the outside of the vial for these pupae with a third identifying mark, such as a “•”.

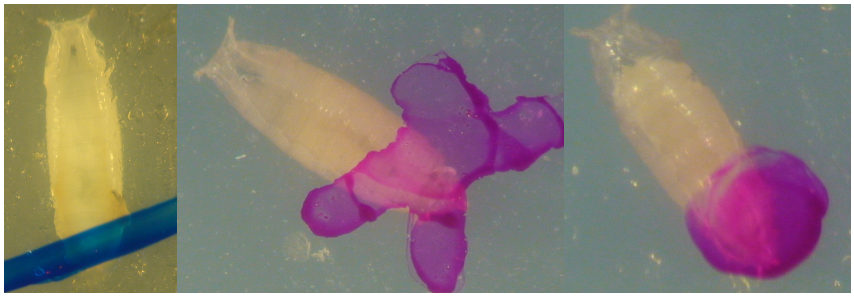

2. Return the vial to its original temperature (29°C, here). Make note of when these pupae were marked.
3. No more than 6 hours later, when you are ready to dissect the pupae, re-evaluate the pupae that had previously fallen into the category of “liquid” pupae marked with an “X”. If they are now “solid” pupae, they can be used for experimentation.
    a. Any “solid” pupa that was “liquid” 6 hours prior now falls between 12–18 hrs APF, and therefore is at the proper time point.
    b. Note: if your experiment requires a more precise time point, say 12–15 hours, then the liquid pupae would need to be re-evaluated no more than 3 hours after initial marking. This staging process is amenable to your experiment’s needs.

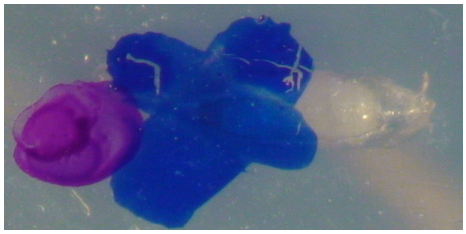

4. To stage the pupae that are still liquid, as well as the newly liquid pupae that were previously larvae, repeat Steps 1–3, using a different colored permanent marker.

Preparation one, Method two – Staging the pupae. Timing: [12–17 hours before]

Need: Dissection scope, permanent marker, vial of 3rd instar larvae or pupae.

1. Under a dissection scope, identify, classify, and mark **every single** pupa in the vial according to the same categories as Preparation one, Method one. This time it is vital to be sure all pupae in the vial are marked and none have been accidentally missed.
2. Return the vial to its original temperature (29°C, here). Make note of when these pupae were marked.
3. No more than 17 hours later, when you are ready to dissect the pupae, re-evaluate all the pupae in the vial. If they were previously white prepupae and are now "solid" pupae, or if they were previously unmarked (because they were larvae during previous staging) and are now "solid" pupae, they can be used for experimentation.
    a. Any "solid" pupa that was a white prepupa 12–17 hours prior now falls between 13–18 hrs APF, and therefore are at the proper time point.
    b. Any "solid" pupa that was previously unmarked must have been a larva at the time of marking, now falls between 12–17 hrs APF, and therefore is at the proper time point.

STEP-BY-STEP METHOD DETAILS

Major step one – Removing pupae from the vial. Timing: ~10 minutes

This step will get properly staged pupae out of their vial, onto double sided tape, and ready for dissection.

1. Place a piece of double-sided tape lengthwise on the center of a microscope slide as shown below, so that the tape begins about one-half inch onto the slide and ends with a small tab overhanging the slide's edge. The tab will allow the tape to be easily lifted from the slide later.

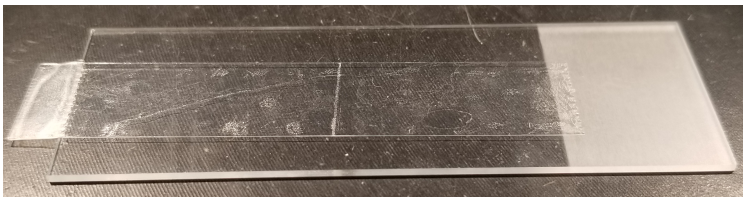

2. Use the dull flat-ended probe to very gently pry the staged pupae off the side of the vial.
    a. Very gently maneuver the flattest part of the probe underneath the pupal case, then lift it away from the vial.

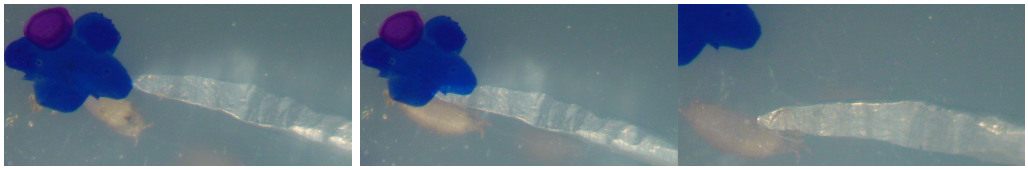

    b. **CRITICAL**: The posterior end of the pupa is generally more resilient to being prodded than the anterior side, but the entire pupa is fragile. If the pupa is popped, it should be discarded.
    c. When the pupa lifts away from the vial, it should stick to the probe and can be carried over to the region of the microscope slide not covered with double-sided tape.

3. Use the fine-tipped forceps to gently pinch the pupa between their anterior spiracles, where the gap between the pupa's head and its case has formed, and place it about one inch onto the double-sided tape.

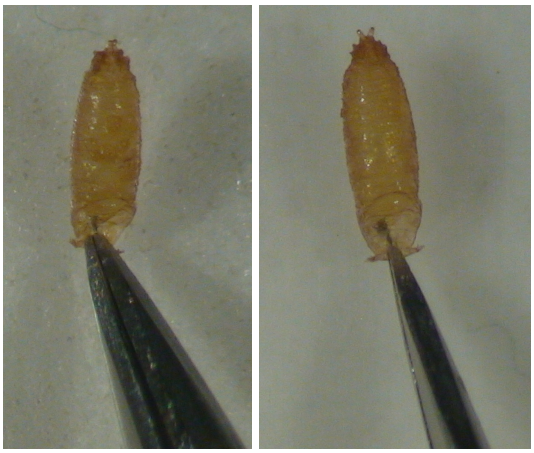

4. With the forceps closed, press down very gently on the posterior end of the pupa to adhere it to the tape as firmly as possible. If they are not adhered, they will lift off the tape during dissection.

5. Place each pupa side-by-side with about two pupa-widths separating them.

   a. Arrange the pupae so all the heads are approximately level with each other.

b. If possible, arrange them with the largest pupa in the center and the smallest pupae on the ends (See Troubleshooting Problem 4).

6. (Optional) To dissect pupae of different genotypes on the same slide, collect all the pupae of one genotype on the tape and label with a permanent marker, then repeat Steps 1–6 with pupae of another genotype.

Pause Point: If needed, this is a pause point before the dissection step, but remember the pupae are still aging.

Major step two – Dissecting the pupal case. Timing: ~20 minutes

This step will dissect away the pupal case, revealing the head and thorax.

1. Under a dissection scope, rotate the entire slide 90° so that anterior faces right if dissecting right-handed (left if dissecting left-handed), and zoom in so the pupae are very large.
2. Use the extra-sharpened forceps to grab the operculum, gently pull it away, and discard it. It should easily pull away from the rest of the case.

3. Press down the newly exposed inside area of the ventral case to the double-sided tape. This will aid in the pupa remaining adhered to the tape when dissecting away the rest of the case.

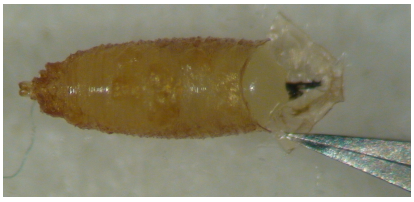

4. Gently insert one tip of the forceps between case and the pupa, and slowly slide the forceps posteriorly. The forceps should be inserted lateral to the midline to prevent puncturing the thorax upon entry, but medial and dorsal enough not to risk puncturing the pupal wing upon forceps insertion. Maintain the forceps at an angle parallel to the pupa and try to keep the tip of the forceps hugging the underside of the case to prevent puncturing the pupa.

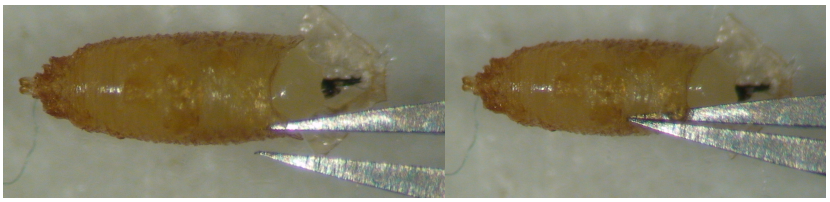

5. Once the tip of the forceps is inserted approximately one-third to one-half of the way down the pupal case, gently pinch the forceps together to perforate/snip the case. Gently

unwrap that portion of the case over the pupa, and adhere the unwrapped portion of the case to the double-sided tape, revealing the dorsal thorax (notum) of the pupa.

6. Unwrap the remaining portion of the case on the opposite side (on the left-right pupa axis), and adhere the unwrapped portion of the case to the double-sided tape.

7. Avoid puncturing the pupae during Steps 4–6, as shown below. If a pupa is punctured, hemolymph will bleed through the epithelium and make the sample unusable. Discard and remove this pupa and continue to the next one. Do not be discouraged if this occurs multiple times when first learning this technique (See Troubleshooting Problem 2).

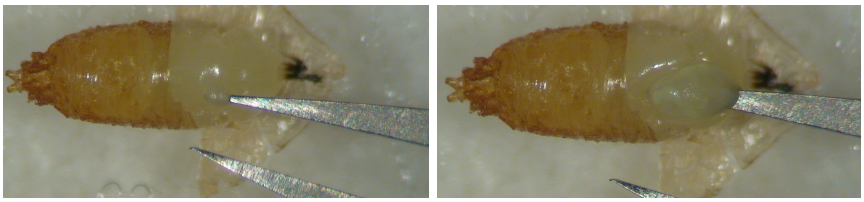

8. Repeat this process for all pupae on the slide.

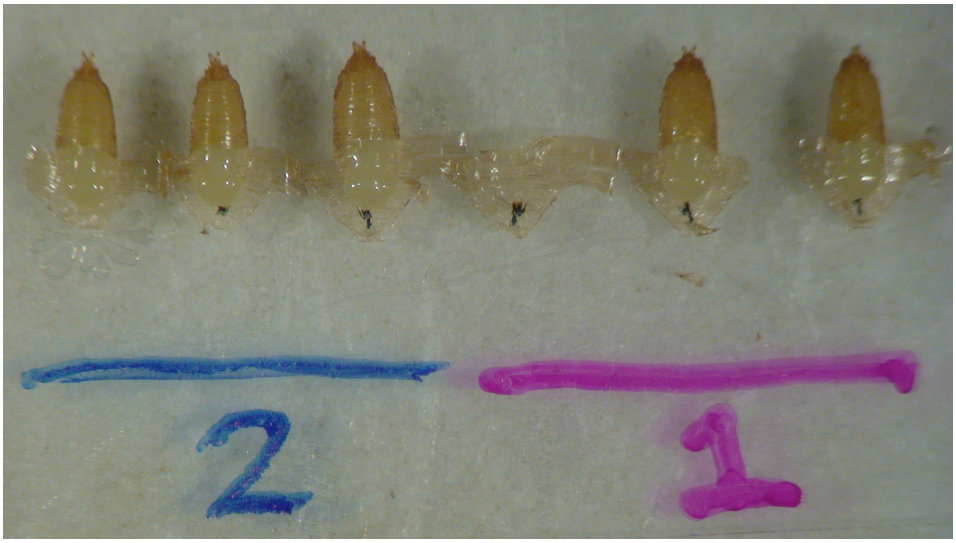

Major step three – Mounting the dissected pupae. Timing: ~10 minutes

This step will get the dissected pupae mounted on cover glass to image the notum.

1. Prepare a large cover glass (35 X 50-1 used here in landscape orientation) by placing two pieces of double-sided tape on top of each other on the lower half of the cover glass. The pupae will be placed so that the tape acts as a riser, raising the abdomen and tilting the head downward onto the glass.

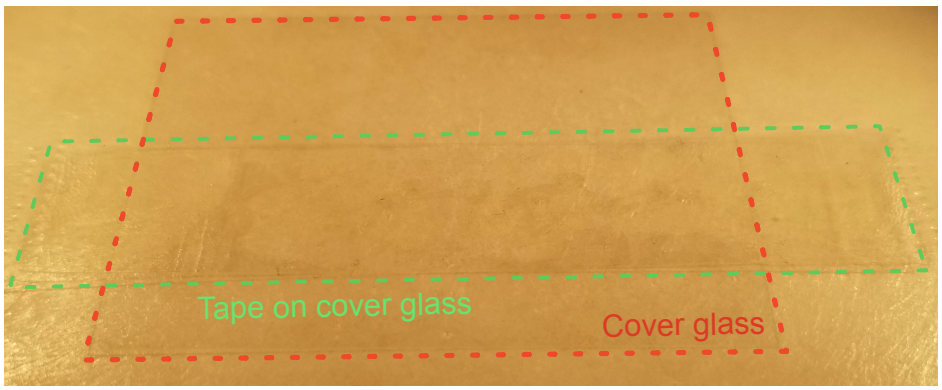

2. Any overhangs can be trimmed with scissors.

3. Carefully remove the double-sided tape with the pupae from the microscope slide by pulling up on the tab previously overhanging the slide. Ensure the pupae are not harmed, and the tape does not curl back and stick to itself.

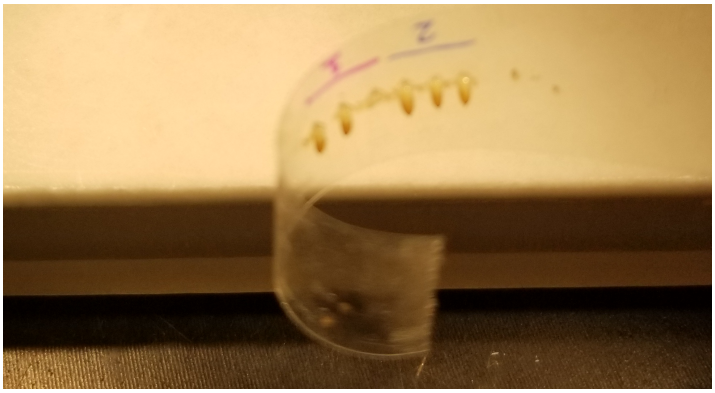

4. **CRITICAL:** Gently lay the tape with pupae onto the cover glass with tape so that: a) the exposed nota of all the pupa are pressed against the cover glass and b) the remnants of

the posterior pupal cases are laid on the cover glass' tape riser. The riser underneath the abdomen act as a fulcrum, levering the head and thorax down just enough to be easily pressed directly against the glass. Do not press the tape down completely against the cover glass on the side nearest the posterior of the pupae; leave a small opening posterior to the pupae for air to enter and escape (See Troubleshooting Problem 3).

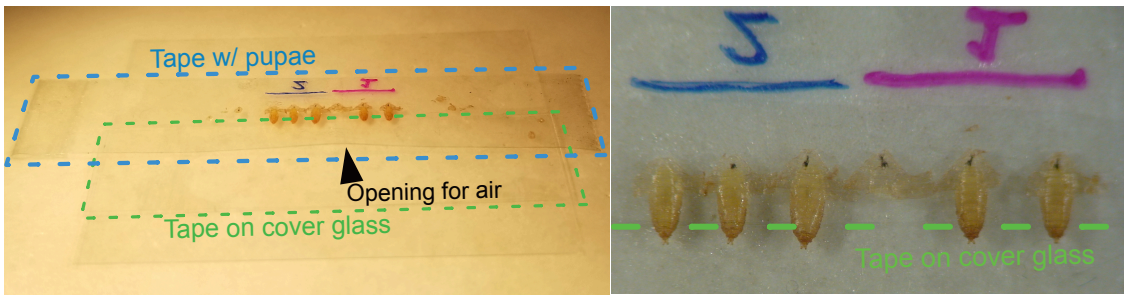

5. To ensure the nota are pressed against the cover glass, use the handle of the forceps to gently press the pupa-containing tape against the cover glass nearest to the anterior side of the pupae, as well as on the left and right sides of the pupae. As more of the tape is pressed, the head and thorax will gradually be pressed against the glass as well. The leverage gained by propping the abdomen up on the tape riser aids in tilting the head and thorax against the glass. Be careful not to press too close to the head of the thorax, for risk of popping the pupa and killing it (See Troubleshooting Problem 3).

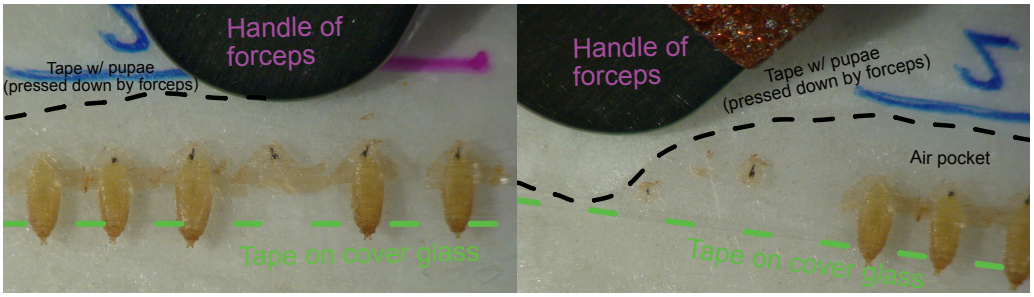

   a. Occasionally flip the slide over to check how much of the notum has been pressed down, being careful not to drop the slide and crush the pupae. The notum will have a visible "pressed against glass" effect.

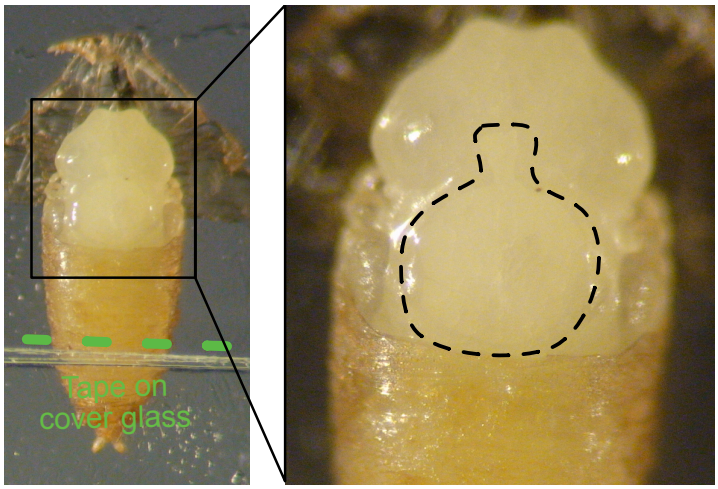

6. (Optional) For long-term imaging, drape a dialysis membrane over the opening posterior to the pupae, and seal the membrane against the pieces of tape that have already been pressed down. Sealing up the sample this way continues to allow gas exchange with minimal pupal desiccation.

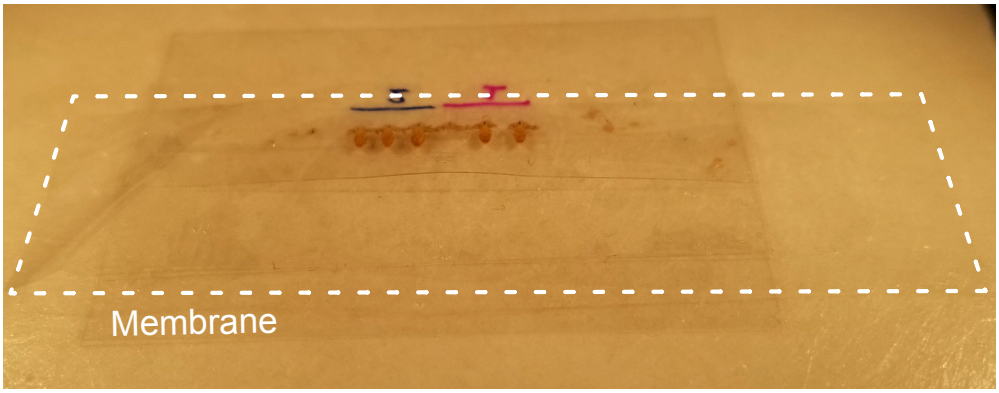

7. Any overhanging pupal tape or membrane can be carefully cut away. The final sample can be imaged immediately or transported in an empty cover glass box.

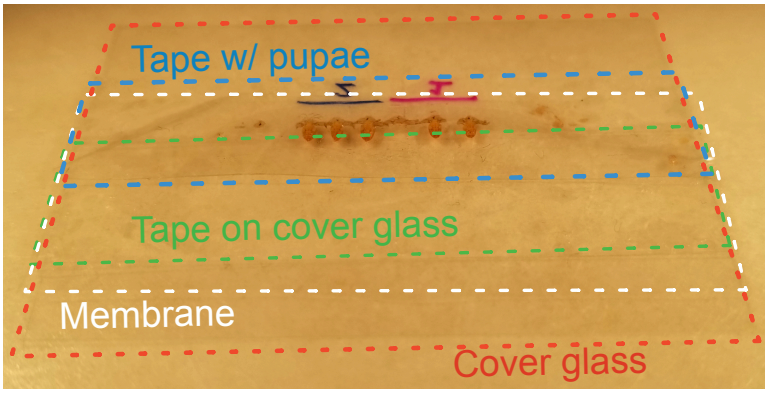

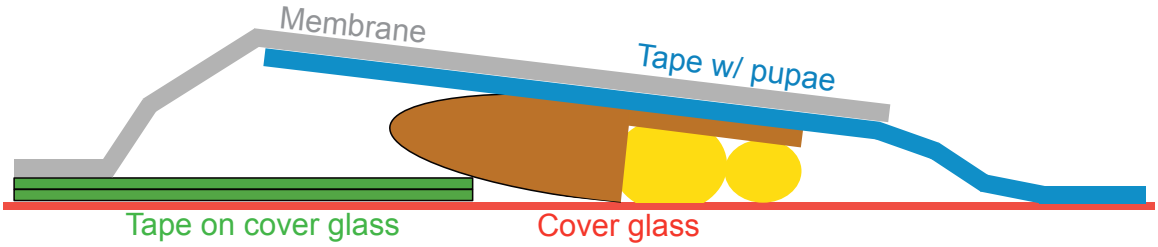

8. Pupae mounted in this manner will develop normally and about 90% survive to adulthood, even after being wounded [113]. After eclosion, the pupae will attempt to crawl out, and get stuck on the tape, demonstrating they survived to adulthood (See Major Step 4-7).

Major step four – Wounding and live imaging the pupae. Timing: ~1 hour, varies by experiment

This step will wound the pupae by pulsed-laser ablation and simultaneously image the epithelial cells. A prerequisite is a laser ablation system attached to the microscope of choice, as described in (Kiehart, et al. 2006) [114]. The following steps will demonstrate how to wound on the border of *pnr-Gal4* gene expression, as in (O'Connor, et al. 2021)[113] using pupae of the following genotype:

ActinP-GCaMP6m / + ; pnr-Gal4, UAS-mCherry.NLS, tubP-Gal80^{TS} / +

1. Mount the slide on an inverted microscope for imaging.
    a. In the example shown, live imaging is performed on a Zeiss LSM410 raster-scanning inverted confocal microscope with a 40x, 1.3 NA oil objective. In this setup, our laser ablation rig was designed to ablate in the same plane as imaging. Here we use a Q-switched Nd:YAG laser (5 ns pulse-width, Continuum Minilite II, Santa Clara, CA). Laser pulse energies were on the order of 1 μJ, but should be adjusted in order to optimize consistent wound sizes.

2. Move the stage to aim the laser to the desired region of the pupa. In this case, the laser ablates at the center of the frame, so the stage is aligned accordingly.
    a. Here the goal is to wound on the border of *pnr-Gal4* expression domain, which is visualized by *UAS-mCherry.NLS*. Thus, we align the stage so the border of mCherry.NLS expression is in the center of the frame (Fig. 1A). Set the camera settings accordingly and save this single-frame image.
3. To image and wound simultaneously, begin taking a time series in the relevant fluorescent channel before wounding (Fig. 1B, first panel).
    a. Here the goal is to visualize intracellular calcium via the genetically encoded calcium sensor GCaMP6m, expressed ubiquitously in the pupa. In this time series, we take a frame every ~2 seconds allowing for the visualization of intracellular calcium before, during, and after wounding.
4. Once baseline images are taken, ablate the sample and continue imaging.
    a. Here, the GCaMP6m calcium sensor immediately fluoresces in the cells proximal to the wound as extracellular calcium rushes into damaged cells around the wound [14] confirming ablation has occurred.
5. Continue monitoring the sample after wounding until the relevant biological phenomenon has been completely observed.

a. Here, we observe the calcium response for approximately 5 minutes after wounding (Fig. 1B).

6. Compile the time series into a movie. Annotate using the mCherry.NLS image to delineate the Gal4-expression domain from the internal control domain (Fig. 1, yellow line).

7. The slide of pupae can be removed and maintained for the duration of pupal development. The pupae will complete development, eclose as adults, attempt to crawl out of their case, and get stuck on the tape, showing clearly which pupae survived to adulthood. Control pupae generally survive even large wounds around 90% of the time when mounted and wounded in this manner [113].

   a. Here, 1 of 2 pupae from genotype 1 (experimental) completely survived to adulthood while 3 of 3 pupae from genotype 2 (control) completely survived to adulthood.

TROUBLESHOOTING

Problem 1: Expression of the *UAS-Gene of interest* causes lethality before or during the pupal stage.

Potential solution: The inclusion of *tubP-Gal80^{TS}* is important for the cases where gene of interest is lethal to the animal when expressed under *pnr-Gal4* expression prior to the pupal stage. *TubP-Gal80^{TS}* allows for gene expression to be controlled by maintaining the animals at 18°C for an extended amount of time, and minimizing the amount of time the gene is expressed at 29°C. Though it requires optimizing, some pupae that would normally die at the pupal stage can be temperature switched at the 2nd or 3rd instar larval stage and survive early pupal stages, but still achieve a sufficient expression by the time experimentation occurs. Additionally, expression of genes that are embryonic lethal, but not harmful to larvae or pupae, can be performed by maintaining the P1 parents at 18°C and temperature switching the larvae to 29°C to begin gene expression after hatching.

Problem 2: Difficulty in dissecting the case without killing the pupa

Potential solution:

As mentioned in Major Step 2-7, the pupae are very fragile at this stage and learning to properly remove the case can be difficult. When first learning, practice on older pupae that are less fragile and easier to dissect. Be sure the forceps are very sharp. Experiment with multiple grips that allow you to slide the forceps between the pupal body and case as consistently as possible. Finally, be sure the pupa is firmly adhered to the double-sided tape so it is not pulled off when you attempt to snip the case.

Problem 3: Difficulty in mounting the pupae so the nota are fully pressed against the glass, without killing them

Potential solution:

As mentioned in Major Step 3-4 and 3-5, the two extra pieces of tape placed on the cover glass are very important to act as a fulcrum levering the head and thorax of the pupae downwards so the nota can be pressed against the glass. The pupa should be aligned with the tape on the cover glass such that only the posterior-most ~20% of the pupa is the resting against the tape. From there, the act of pressing the tape with pupae on the side nearest the anterior of the pupae will press the head and notum down against the cover glass while the most posterior end of the pupa will remain propped in the air.

If the nota will not get pressed against the cover glass in this way, experiment with additional or fewer pieces of cover glass tape or propping the pupa further up/further down the abdomen (i.e. so that more or less of the pupa is resting against the tape).

Problem 4: When mounting the pupae, some pupae get pressed too much and die before others are sufficiently pressed enough against the glass.

Potential solution:

Spacing the pupae father apart on the slide in Main Step 1–5 can also help with this problem. Additionally, as mentioned in Major Step 1-5b, arranging the pupae on the slide such that the largest (either by length or volume) pupae are in the center may help avoid this problem. Larger pupae will require less tape to be pressed down in order for the notum to be sufficiently pressed against the glass. Conversely, smaller pupae require more tape to be pressed down in order for the notum to be sufficiently pressed against the glass. By extension, larger pupae will also die first if the tape is pressed down too much. Therefore, a small pupa mounted in between two larger pupae will be very difficult to sufficiently press against the glass without also killing the larger pupae. Instead, by having the largest pupae in the center and the smaller pupae arranged on the sides, you can press down more of the tape to the left and right

of the pupae to sufficiently press all of the pupae against the glass without over-pressing and killing the largest pupae.

Acknowledgments

This work was supported by the National Institute of General Medical Sciences (1R01GM130130 to A.P.-M.and M.S.H.), the National Institute of Arthritis and Musculoskeletal and Skin Diseases (R21AR072510 to A.P.-M.). E.K.S. was supported by the National Cancer Institute (5T32CA119925) and J.T.O. was supported by the National Institute of Child Health and Human Development (T32HD007502) and the American Heart Association (19PRE34410069 to J.T.O.).

Author contributions

Conceptualization – JTO, EKS, APM; Data curation – JTO; Funding acquisition – JTO, EKS, APM, MSH; Investigation – JTO, EKS; Methodology – JTO, EKS; Project administration – APM, MSH; Resources – APM, MSH; Software – MSH; Supervision – APM, MSH; Visualization – JTO; Writing (original draft) – JTO; Writing (review & editing) – JTO, APM.

Chapter 2 Figure

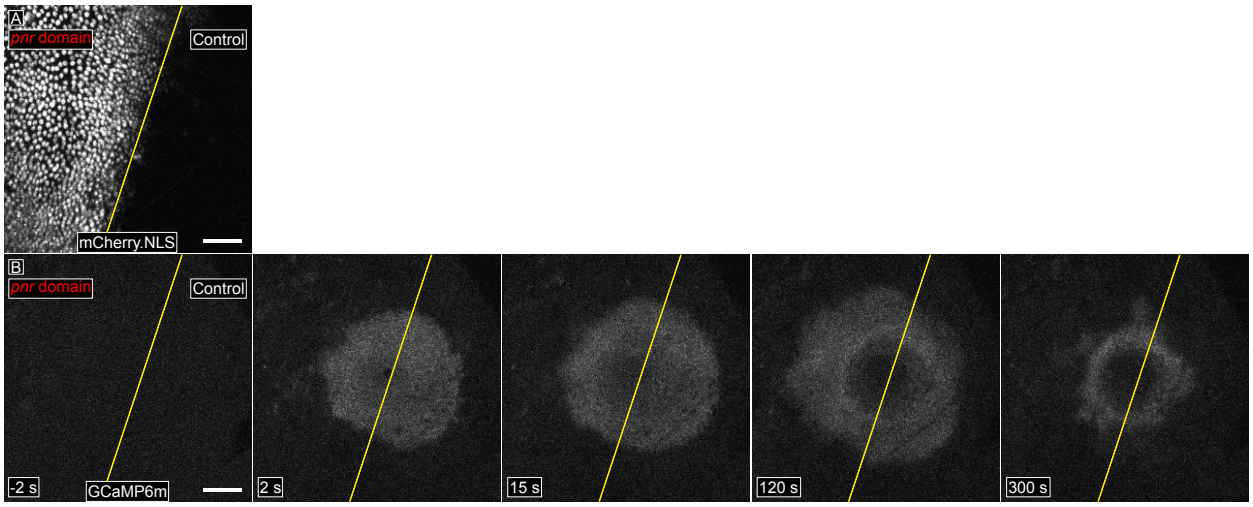

Chapter 2, Figure 1: Calcium signaling data obtained after wounding using this methodology. A) The right side is an internal control domain; the left side shows *UAS-mCherry.NLS* driven by *pnr-Gal4,* delineating the domain of *pnr* expression, which can be used to drive a variety of genes of interest. The yellow line demarcates the border. B) Time lapse of the ubiquitously expressed calcium sensor GCaMP6m, used to monitor calcium signaling over time following wounding. The yellow line is copied from the placement in A. Scale bar = 50 µm.

CHAPTER 3

ZONES OF CELLULAR DAMAGE AROUND PULSED-LASER WOUNDS

This chapter is adapted from: O'Connor, JT., Akbar, FB., Hutson, MS., Page-McCaw, A., Zones of Cellular Damage Around Pulsed-Laser Wounds. *PLOS One*. 2021. 16(9): e0253032.

ABSTRACT

After a tissue is wounded, cells surrounding the wound adopt distinct wound-healing behaviors to repair the tissue. Considerable effort has been spent on understanding the signaling pathways that regulate immune and tissue-resident cells as they respond to wounds, but these signals must ultimately originate from the physical damage inflicted by the wound. Tissue wounds comprise several types of cellular damage, and recent work indicates that different types of cellular damage initiate different types of signaling. Hence to understand wound signaling, it is important to identify and localize the types of wound-induced cellular damage. Laser ablation is widely used by researchers to create reproducible, aseptic wounds in a tissue that can be live-imaged. Because laser wounding involves a combination of photochemical, photothermal and photomechanical mechanisms, each with distinct spatial dependencies, cells around a pulsed-laser wound will experience a gradient of damage. Here we exploit this gradient to create a map of wound-induced cellular damage. Using genetically-encoded fluorescent proteins, we monitor damaged cellular and sub-cellular components of epithelial cells in living *Drosophila* pupae in the seconds to minutes following wounding. We hypothesized that the regions of damage would be predictably arrayed around wounds of varying sizes, and subsequent analysis found that all damage radii are linearly related over a 3-fold range of wound size. Thus, around laser wounds, the distinct regions of damage can be

estimated after measuring any one. This report identifies several different types of cellular damage within a wounded epithelial tissue in a living animal. By quantitatively mapping the size and placement of these different types of damage, we set the foundation for tracing wound-induced signaling back to the damage that initiates it.

INTRODUCTION

The field of wound repair and regeneration has long sought to connect the signals emanating from wounds to the behavioral changes undertaken by cells around the wound. In response to wounds, tissue-resident cells transition from a stationary and non-proliferative state to a migratory or proliferative state [4,66,68,110], whereas immune cells migrate from outside the tissue to clear debris and fight infection by pathogens entering through the wound [7,90,115–117]. Ultimately, the signals emanating from wounds must be derived from the damage itself; however, only a few studies have characterized the damaged tissue on a cellular/sub-cellular level to understand the distinct types of damage created by wounds [23,24,118,119]. Importantly, our previous studies have found that multiple signaling pathways are initiated around the same time within the same wound, and further, that distinct types of cellular damage initiate each signaling pathway. Specifically, cell lysis leads to the release of cellular proteases, which cleave and activate cytokines in the vicinity of the wound, which in turn signal to surrounding cells through G-protein coupled receptors [113]. However, even before cytokine signaling is evident, cells with a different type of damage – torn plasma membranes – initiate calcium signaling, as extracellular calcium floods in through damaged membranes and out through gap junctions to undamaged neighboring cells [14]. Together, these studies suggest that understanding the origin of wound-induced signaling requires identifying and categorizing different types of cellular damage induced by wounding. In this study, we attempt to solve this problem by classifying various zones of damage around epithelial wounds visualized using genetically-encoded fluorophores,

and mathematically defining the relationships between these zones of damage to create a map of the characteristic cellular damage experienced by a tissue following a wound.

It may be impossible to develop a useful map of cellular damage around ordinary trauma wounds experienced in the natural world, as the types of damage would be irregularly arrayed and would not be sufficiently reproducible to identify patterns. However, researchers often employ laser-induced wounding, which has advantages compared to other methods of wounding because of its ability to make reproducible, radially-symmetric, aseptic wounds in a tissue while simultaneously imaging [6,7,9,11,14,16,20,21,68,74,120–124]. Two types of lasers are used to damage tissues – continuous wave lasers and pulsed lasers – which make very different types of cellular damage. A continuous wave laser delivers energy to the sample on the order of milliseconds to seconds, and in doing so delivers a high amount of thermal energy to both the ablated region and the surrounding tissue, causing burning and/or explosive ejection of cellular debris from the sample [23]. In contrast, a pulsed laser delivers energy with pulsewidths on the order of femtoseconds to microseconds, dramatically decreasing the thermal energy transfer to the surrounding tissue [23,125]. A pulsed laser superheats only the focal spot, vaporizing it into a bubble of gas known as a cavitation bubble, which expands and contracts within microseconds, causing mechanical (but not thermal) damage to the surrounding tissue [23,24,126,127]. Although continuous lasers were often used through the 1980s, pulsed lasers have become more widely used over the last three decades because of the shorter thermal event, delivering energy so rapidly as to destroy and remove hot tissue before the heat can be transferred, thus reducing thermal damage to the surrounding tissue and removing burn damage as a confounding variable in studying wound signaling and repair [125,126]. Although other methods of wounding have been utilized in wound repair studies, namely puncture [9,128,129], pinch [130,131], scratch wounding [13], or complete amputation [10,90,132], these methods can introduce experimentally-induced variability that hinders reproducibility.

Previously, our labs used pulsed-laser wounding on an epithelial monolayer in living *Drosophila* pupae to understand wound-induced repair signals, specifically how calcium is increased in the cytosol of cells around wounds [14]. Unexpectedly we found that the laser-induced cavitation bubble damages the plasma membranes of epithelial cells around the wound margin, creating microtears that allow extracellular calcium to flood into damaged cells within milliseconds of wounding. To study this phenomenon, we varied the laser energy and found that cavitation bubble area matched the areas of extracellular calcium entry, membrane depolarization, and extracellular dye entry, three indicators that plasma membrane integrity was lost in the tissue damaged by the cavitation bubble [14]. Many of the cells with plasma membrane damage were able to repolarize and survive, demonstrating that not all damaged cells die. Other reports have demonstrated loss of plasma membrane integrity of cells around wounds made by multiple types of injury [13,21,22,119,124,133]. Indeed, in these studies many of these cells with plasma membrane damage survived and were able to restore membrane integrity [21,119]. Thus, these previous studies show there are *at least* two populations of cells that experience damage following a wound: cells near the center of the wound that are damaged so severely that they are destroyed and cells distal from the center of the wound that are damaged but ultimately survive and participate in the repair process. In this study, we identify several more types of cells that are damaged by laser wounds; specifically, we monitored initial laser-induced rupture, delayed cell lysis, nuclear membrane damage, plasma membrane damage, chromatin disruption, Ecadherin loss, and a calcium expansion outward from the wound site. The severity of damage was inversely correlated with radius from the wound center, and by varying wound size, we find that these regions of damage are arrayed in predictable and reproducible patterns around the wound.

RESULTS

We chose *Drosophila melanogaster* (fruit flies) for wounding studies because they are genetically tractable, with numerous existing strains expressing genetically-encoded fluorescently-tagged proteins easily visualized during live imaging. We analyzed wounds in the pupal notum, the epithelial tissue on the dorsal thorax of the pupa, easily accessible after partially removing the pupal case [6] (Chapter 3, Figure 1A). Wounds were administered by pulsed-laser ablation, allowing simultaneous wounding and imaging *in vivo*. Because the pupa is stationary, it can be easily mounted, wounded, and imaged for extended periods of time (hours to days) and still survive to adulthood.

Using the *Gal4/UAS* system [111], we drove expression in the pupal notum of the fluorescent protein mCherry with a nuclear localization signal (mCherry.NLS) to visualize live epithelial nuclei. In unwounded animals, mCherry.NLS fluorescence is normally punctate but becomes diffuse during cell division, later re-appearing as two separate punctae (Chapter 3, Figure 1B). Since mCherry.NLS is a freely-diffusible fluorescent protein carrying a nuclear localization signal, this pattern indicates that mCherry.NLS diffused into the cytosol during nuclear membrane breakdown (Chapter 3, Figure 1C).

Upon pulsed-laser ablation, the mCherry.NLS fluorescence was lost at the wound center within the first two frames after ablation (usually ~2 seconds). Because the fluorophore was lost from both the nucleus and the surrounding cytoplasm (orange circle, Chapter 3, Figure 2A'), this loss of fluorescence indicates cell destruction and rupture. We term this immediate loss of mCherry the **region of laser-induced rupture.** This region includes the area of the laser focus and plasma formation where photochemical damage destroys macromolecular structures (~ 1 μm in diameter, [24]) as well as the area of the most severe cavitation-driven shear stress, which causes immediate cellular destruction. Note that the region of laser-induced rupture is nonetheless much smaller than the maximum area of the cavitation bubble (see below) [24,134]. In

the wounds made for this study, the size of laser-induced rupture ranged between 10 and 30 μm in radius.

Within 90 seconds after pulsed-laser ablation, the mCherry.NLS signal changed in two distinct ways. First, the region devoid of mCherry signal increased in size, indicating that even after ablation, cells continue to lyse (compare Chapter 3, Figure 2A,B). No fluorescence signal returned to this region until late in the repair process when distal cells migrated in to repair the wound. This larger area of cell death we term the **region of delayed cell lysis** based on the complete loss of mCherry.NLS by 90 seconds after wounding (red circle, Chapter 3, Figure 2B'). Both the initial laser energy and the ensuing cavitation bubble may contribute to cell lysis in this area.

Second, beyond the delayed cell lysis area, the mCherry.NLS became diffuse, no longer confined to the nucleus but still remaining in the tissue (light blue circle, Fig 2B'), similar to its appearance during mitosis (Chapter 3, Figure 1B). Interestingly, later in the repair process the mCherry signal returned to the nucleus in some of these cells, indicating that some of these cells survive (Chapter 3, Figure S1). We concluded that these cells have undergone damage to the nuclear membrane, causing the previously nuclear-localized mCherry to be released from the nucleus into the cytosol (Chapter 3, Figure 2B). We term this the **region of nuclear membrane damage**.

To understand how these zones of damage compared with other types of damage we had already characterized, we compared the mCherry.NLS patterns with those of GCaMP, a ubiquitously expressed genetically encoded cytoplasmic calcium reporter. Our previous work demonstrated that within the first frame after pulsed-laser ablation, cells near the wound exhibit an increase in GCaMP fluorescence. This region of immediate GCaMP fluorescence indicates the region where the plasma membrane is torn by the laser-induced cavitation bubble, allowing the rapid influx of extracellular calcium [14]. The cavitation bubble expands and collapses within

microseconds, and extracellular calcium enters through microtears in the plasma membrane within ~10 milliseconds, increasing its concentration over the next few seconds as more calcium enters the cell [14]. Thus, the immediate GCaMP signal indicates the **region of plasma membrane damage** (green circle, Chapter 3, Figure 2C'). Although the GCaMP signal is still dim in the first frame after wounding, the first frame provides the most accurate measure of the area of plasma membrane damage because the calcium diffuses outward to neighboring cells through gap junctions over the next 15-20 seconds, enlarging the area of GCaMP6m fluorescence beyond the region of plasma membrane damage [14].

After measuring the radii of these four well-defined regions in multiple samples with varying wound sizes, we found the four regions maintained the same ascending size order within every sample: Laser-induced rupture < delayed cell lysis < nuclear membrane damage < plasma membrane damage (Chapter 3, Figure 2D). To determine whether there was a consistent relationship between the radii of each region, we analyzed how each of these four regions related to one another in wounds of various sizes and graphed the six relationships (Chapter 3, Figure 2E-H). This analysis revealed that the radius of each zone was linearly correlated with the radius of each other zone, with an R^2 value for each of the trendlines lying between 0.78 and 0.92. Importantly, these results show that each laser-induced wound creates reproducible regions of damage around a single wound, and all of these regions can be reasonably estimated after measuring the radius of a single one. Not only were adjacent zones of damage related linearly, but also the linear relationship was maintained even between laser-induced rupture and plasma membrane damage, the smallest and the largest zones of damage respectively (Fig 2J).

To better understand the nuclear membrane damage, we co-expressed mCherry.NLS and a GFP-tagged histone variant, His2Av-GFP. Unlike mCherry.NLS, the GFP-tagged histone is a fusion protein incorporated into chromatin, regardless of cell cycle stage or nuclear envelope integrity. Therefore, we could track nuclear destruction independently of nuclear

membrane damage. At 5 minutes after wounding, there were many intact, well-ordered, His2Av-GFP-containing nuclei within the region of nuclear membrane damage, confirming that the nuclear membrane, but not necessarily chromatin, are damaged in this region (Chapter 3, Figure 3A-C). However, toward the center of the wound there were some misshapen punctae of His-GFP (Chapter 3, Figure 3A-C). We term this the **region of chromatin disruption**, which we measured and compared to the regions of delayed cell lysis and nuclear membrane damage (Chapter 3, Figure 3A-C). We found that the chromatin disruption region was much smaller than the nuclear membrane damage region (Fig 3D) and was similar in size to the region of delayed cell lysis (Chapter 3, Figure 3E). These results demonstrate that even after cell lysis, the His-GFP and chromatin do not freely diffuse. Further, they raise the possibility that delayed lysis and chromatin disruption are related. Although the best-fit equation relating these two zones had a slope less than one (Chapter 3, Figure 3D), a simple y=x relationship between the regions of chromatin disruption and delayed cell lysis had an R^2 of 0.84, which shows the two regions indeed correlate very well with each other.

To monitor individual cells in addition to individual nuclei, we co-expressed the mCherry.NLS fluorescent marker with GFP-tagged Ecadherin to visualize nuclei and cell borders simultaneously. Interestingly, a new region of damage was evident after wounding as a region of **immediate Ecadherin loss**. This region was evident starting at the first frame after wounding, although we often measured it at 5 min after wounding as the radius of clear Ecadherin loss does not significantly change within this time (Chapter 3, Figure S2), and because this allowed time to switch the objective from the 40x ablation objective to a 63x objective for higher-resolution imaging. The Ecadherin labeling along cell borders appeared disrupted within a radius smaller than the region of nuclear membrane damage (yellow and light-blue circles respectively, Chapter 3, Figure 4A-C,E), and surprisingly, smaller than the region of delayed cell lysis where cells had completely lost mCherry.NLS signal (yellow and red circles respectively, Chapter 3, Figure 4A-D). The stability of Ecadherin complexes in adherens

junctions at least transiently withstood damage such as cell lysis and release of cytoplasm, but over the next hour, the region of Ecadherin loss expanded (Chapter 3, Figure S2). This latter gradual loss of Ecadherin may be similar to the endocytosis of Ecadherin observed at the margin of wounds in fly embryos [12,135], but endocytosis is not fast enough to drive the immediate loss of Ecadherin evident as soon as the first frame after wounding (Chapter 3, Figure S2).

Given that Ecadherin may remain for some time along the borders of lysed cells and that it may be endocytosed and removed from the borders of cells that are nonetheless intact, we wanted to determine the relationship between the gradual loss of Ecadherin and cell lysis. To do so, we imaged pupae co-expressing Ecadherin-GFP and mCherry.NLS for 90 minutes following wounding. Many adherens junctions that initially appeared as intact cell borders started breaking down around 30 minutes and were gone by 90 minutes (Chapter 3, Figure S2), disassembling throughout the region of delayed cell lysis more or less simultaneously. The region where Ecadherin complexes were dismantled (Chapter 3, Figure S2, yellow asterisks) spanned the entirety of the delayed cell lysis region determined by mCherry.NLS (Chapter 3, Figure S2, red circle) as well as one to two cell diameters into the region of nuclear membrane damage (Chapter 3, Figure S2, light blue circle). Thus, the Ecadherin/adherens junctions within the delayed cell lysis region that appear stable five minutes after wounding represent the carcasses of dead/dying cells that do not survive the repair process.

The last damage-induced landmark we analyzed was the progression of the cytoplasmic calcium signal outward from the wound within the first seconds after wounding, measured as an increase in the radius of GCaMP fluorescence. After extracellular calcium enters cells through plasma membrane damage, that initial influx of calcium expands outward to neighboring cells through gap junctions within 15 seconds following wounding [14,113]. We have termed this the **first calcium expansion**, so called because there is an independent second calcium response later [113]. Although the first calcium expansion does not represent a type of cellular damage, it may represent damage-induced information transmitted to nearby cells, and we were interested

to see how it compared in size to the damage itself. We compared the radius of the first calcium expansion to the radius of plasma membrane damage and found that it was positively correlated with a trendline of slope near 1, but with a y-intercept of 19 μm (Fig 5). This linear relationship suggested that regardless of wound size, the initial influx of calcium travels about 20 μm outward to the next 2-4 neighboring cells, which experience this wound induced calcium signal even though they are ostensibly undamaged.

By analyzing these fluorescent proteins, we have identified seven concentric zones of damage surrounding a single laser wound. These zones of damage are linearly related to one another by the 11 equations in Figs 2-5 derived from the observed data (observed data is provided in S1 Dataset). Further, these 11 equations can be combined to relate any two zones of damage (Chapter 3, Figure 6A; see Materials and Methods), allowing a reasonable estimation of the radius and 95% confidence interval of all the zones of damage from any one of them. To do this, we provide an Excel book (S2 Dataset) that describes the 42 linear equations required to approximate any of the zones of damage from a measurement of a single zone (sheet 1: Total Equations List). Further, seven subsequent Excel sheets are provided to allow the user to input a radius of one zone of damage and output the approximate radius and confidence intervals for the remaining six zones of damage (sheets 2-8). As an example, we calculated these damage regions for laser-induced rupture radii of 10, 20, or 30 μm, corresponding to small, medium, or large wounds made in this study (Chapter 3, Figure 6B). In doing so, we found the radii of the four inner-most regions of damage were clustered extremely tightly together in small wounds (10 and 20 μm laser-induced rupture), such that their radii are less than a single cell diameter (~7 μm) apart from each other. Thus, around small wounds, it is not meaningful to distinguish those four different regions of laser-induced rupture, immediate Ecadherin loss, chromatin disruption, and delayed cell lysis. However, in larger wounds with greater than 20 μm of laser-induced rupture, the seven regions of damage and wound signaling separate from each other and resolve into the same ascending size order: laser-induced rupture

< immediate Ecadherin loss < chromatin disruption ~ delayed cell lysis < nuclear membrane damage < plasma membrane damage < first calcium expansion.

DISCUSSION

These data show that a wound induced by pulsed-laser ablation causes tissue damage in a graded pattern and not in a uniform manner. Damage is most severe at the center of the wound, which is the focal point of the laser, and is progressively less severe with distance from the center. Importantly, cellular damage encompasses a region much larger than the area where cells are entirely destroyed, and many damaged cells recover and participate in wound repair.

From a spatial perspective, the zones of damage are arranged in a fixed order. Laser wounding involves a combination of photochemical, photothermal, and photomechanical effects, each falling off at a different rate with distance. Each type of damage is likely triggered by one or more particular effect at specific energy or stress thresholds. The first and most central visible zone of damage is the immediate **laser-induced rupture** of cells. At the very center of the wound, the highest laser power drives multiphoton ionization, plasma formation and ultimately molecular recombination that destroys biomolecules[134]. Just slightly further out, stresses from the rapidly expanding cavitation bubble and shock wave destroy macromolecular assemblies. Together these types of damage would appear as a region devoid of mCherry.NLS fluorescence in the first frame after wounding. This region of immediate laser-induced rupture may be the same as the region of **immediate Ecadherin loss**; perhaps the loss of Ecadherin represents one specific type of macromolecular destruction. Although both these regions are recognized by a loss of fluorescence, this loss is more than photobleaching. We note that some molecules retain fluorescence within this area, such as histone-GFP, which retains its fluorescence even though the morphology is disrupted (discussed below).

Moving outward from the center of the wound, the next region of damage is the region of **delayed cell lysis**, identified by the area that loses mCherry.NLS fluorescence in the minutes after wounding. We had expected cell lysis to be an immediate response to damage, but it appears instead that damage triggers lysis in many cells over the course of minutes [113]. It is noteworthy that the region of **immediate Ecadherin loss** is smaller than the region of delayed cell lysis within the first five minutes after wounding. A potential explanation is that Ecadherin is present in stable macromolecular complexes at the junctions, and therefore may appear intact even if the corresponding cell has lysed. Interestingly, Ecadherin appears to be disassembled over a much larger area during the next 90 minutes, with disassembly happening around the lysed cells and intact borders remaining only around cells that survive and participate in the wound response (Chapter 3, Figure S2). Previous studies in embryos have reported that Ecadherin is rapidly endocytosed from the wound margin within minutes of wounding, and the endocytosis of adherens junctions is essential for building the actin-myosin purse-string[12,135]. The loss of Ecadherin from the proximal border of the closest surviving cells in pupal wounds could be a similar response; however, the earliest loss we observed is distinct, as are the losses over the next hour from cells that lyse[136]. Our results raise the possibility that in addition to functional remodeling of the cell-cell junctions that occurs in cells that participate in the repair process, Ecadherin-GFP removal after wounding may also represent the removal of cellular debris.

The region of delayed cell lysis largely overlaps with the region of **chromatin disruption**, assessed after lysis. It may be that chromatin appears disrupted because a cell no longer protects it; conversely, perhaps damage to the chromatin propels cell lysis. The question of whether the regions of delayed cell lysis and chromatin disruption represent the same region brings up the issue of the resolution of detection. Although the damage profile may cause a gradient in damage to molecules, our limit of detection is a single cell, with a diameter of about 5-10 μm. Thus, two regions of damage that differ by less one-cell diameter cannot be

distinguished and may have no functional difference for the tissue response to the wound. From this perspective, it may be useful to consider the regions of delayed cell lysis and His-GFP disruption to be the same.

The next distinct zone is **nuclear membrane damage**, identified by the cloud of mCherry.NLS that leaves the nuclear compartment and floods the cytoplasm when laser-induced stresses compromise nuclear membrane integrity. In addition to nuclei, we expect other membrane-bound organelles to be damaged by similar amounts of stress in this same region. In the more central zones of laser-induced rupture/immediate Ecadherin loss and delayed cell lysis/His-GFP disruption, all the cells die. In contrast, in the zone of nuclear membrane damage, some cells die but most cells recover and participate in wound closure (Chapter 3, Figure S1 and S2). The actomyosin purse-string that forms at the wound margin likely segregates the cells that will survive and repair from those that will die [6,66,68].

The most distant zone of cellular damage is the zone of **plasma membrane damage**. In this region, the mechanical shear force of the cavitation bubble rips the plasma membrane, and this zone is identified by the immediate GCaMP fluorescence from extracellular calcium flooding into the cytoplasm. In a previous study, we analyzed this zone extensively [14] and found that it correlates with both an area of membrane depolarization and area of permeability to extracellular dyes. On kymographs, we visualized calcium entering into cells through distinct spots within this region. Cells with damaged plasma membranes in this region are able to repair the damage; indeed, the extracellular calcium is probably an important trigger for initiating plasma membrane repair [20,21]. As we demonstrated previously, the influx of calcium is not contained within the damaged cells, and calcium expands through gap junctions to neighboring cells in a process we call the **first calcium expansion**. Although not technically a zone of damage, this landmark is caused by damage. Interestingly, the first expansion was a constant distance, about 20 μm, out from the region of plasma membrane damage. This result implies

that the first expansion is entirely determined by the initial influx, and the 20 μm distance is likely determined by the kinetics of calcium buffering and re-uptake systems.

The radii of the regions of cellular damage are linearly related, in surprisingly simple relationships that we did not expect at the outset. We derived equations relating the regions of damage, and we expect these equations will be useful in estimating each region of damage when only one is known. For example, any freely diffusing fluorescent molecule expressed in cells can reveal the area of initial laser rupture and/or delayed cell lysis, depending on the timing of data acquisition; from either of these data points, estimates for the regions of stable protein complex destruction (Ecadherin loss), nuclear membrane damage, and plasma membrane damage, and the region of high initial calcium can all be calculated.

From a temporal perspective, the initial laser pulses and following cavitation bubble cause immediate and complete cellular destruction at the very center of the wound, and simultaneously they cause a loss of nuclear membrane integrity in cells farther out, and a loss of plasma membrane integrity in cells still farther away. Next, in the milliseconds to seconds following wounding, the first known intercellular wound signal – calcium – floods into damaged cells and then travels to neighboring cells, notifying unwounded nearby cells of the damage that has just occurred. Finally, over the next minute or two, a region of delayed cell lysis appears around the initial laser-induced rupture, where cells lose their cytoplasmic contents.

It is interesting to speculate whether each zone of cellular damage evaluated here might correspond to a specific downstream repair behavior initiated by the organism in response to the wound. For example, the delayed cell lysis region may be associated with a region of protease release and/or ligand activation leading to a GPCR-mediated calcium response in the minutes following a wound [113]. The zones of calcium signaling may be similar to the zones of increased reactive oxygen species [7,90,137] and/or actin remodeling [6,20]. The debris left behind in the center of wound and visualized in Histone-GFP and Ecadherin-GFP samples may represent a type of debris that is cleared away by immune cells later in the repair process [138–140].

The results of this study expand on an earlier study by Hellman, et al. [118], which identified 3 separate regions of damage after laser wounding in cell culture: a region of destruction at the center, a necrosis region of cells that die progressively over time, and a region of “molecular delivery” whereby wounded cells become permeable to the extracellular space. These seem qualitatively similar to our identified regions of laser-induced rupture, delayed cell lysis, and plasma membrane damage, respectively, which here we have shown in a living animal. Additionally, we report a nuclear membrane damage region and characterize sub-cellular damage markers using genetically-encoded fluorophores. Whereas Hellman, et al. analyzed how regions of damage varied with laser energy [118], our focus is on how the regions of damage correlate with each other, with the goal of estimating the distinct regions for any pulsed-laser wound.

CONCLUSIONS

This study analyzed wounds made by pulsed-laser ablation, which creates reproducible and orderly wounds, with the regions of damage arranged in a reproducible manner. In trauma wounds caused by puncture, crush, or pinch wounds, all the types of damage examined in this study are expected to occur but without precise spatial patterning, rendering them difficult to identify and analyze. Thus, pulsed-laser ablation is a valuable research tool, allowing distinct regions of damage to be resolved through microscopy, and offering the opportunity to relate each type of damage with specific cellular responses.

When an epithelial barrier is breached, the cellular landscape is dramatically altered and must be repaired to avoid exposure to pathogens or loss of internal fluid [9,15]. Although some cells at the center of a wound may be destroyed immediately or lost progressively, many partially damaged cells around the wound survive and respond by initiating the repair process, indicating that both cellular repair and tissue repair programs are activated by the same wound

[6,110,133]. Undamaged cells farther out also receive instructive cues from the wound, recruiting them to participate in the repair process as well [6,110,141,142]. To understand how damage initiates repair, it is critical to understand the types of damage present around a wound. However, little work has been done to characterize damaged tissue on a cellular/sub-cellular level and understand how the epithelial architecture is altered in the immediate aftermath of wounding. By characterizing zones of cellular damage, we have provided insight into what kinds of cellular changes occur to the tissue in the moments following wounding. As we have recently reported, some of these specific regions of damage initiate specific signals, and probably more have yet to be discovered. Ultimately, cellular damage itself acts as an input stimulus for the eventual behavioral output. Future studies will explore how these damage-induced cellular alterations initiate the repair process.

Acknowledgements

We thank Kimi LaFever Hodge for making fly stocks and maintaining flies when the lab was shut down for the pandemic. Erica Shannon made the initial observations of the diffuse nuclear mCherry signal. We thank Aaron Stevens and James White for helpful conversations. Some fly lines were obtained from the Bloomington Drosophila Stock Center and Kyoto Stock Center.

Author Contributions

Conceptualization: J.O.C., A.P.M., M.S.H; Formal Analysis: J.O.C., F.B.A.; Investigation: J.O.C.; Resources: A.P.M., M.S.H.; Data Curation: J.O.C., F.B.A.; Writing – Original Draft: J.O.C., A.P.M.; Writing – Review & Editing: J.O.C., A.P.M., M.S.H; Visualization: J.O.C., F.B.A.; Supervision: A.P.M., M.S.H; Funding Acquisition: J.O.C., F.B.A., A.P.M., M.S.H.

CHAPTER 3 MAIN FIGURES

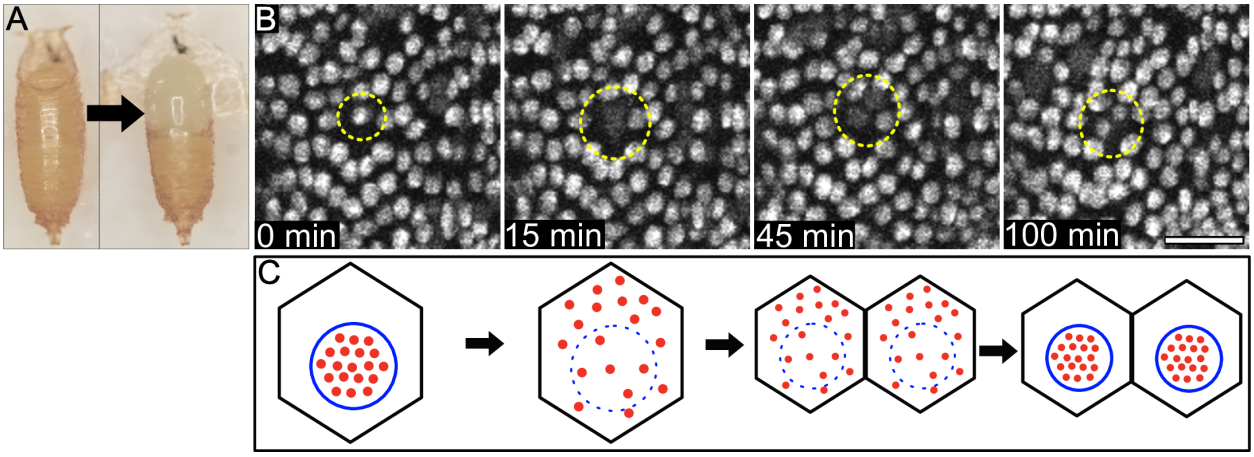

Chapter 3, Figure 1: mCherry.NLS reports nuclear envelope integrity.
(A) An intact *Drosophila* pupa (left) and one prepared for imaging with the pupal case partially removed (right), exposing the pupal notum. (B) Interphase nuclei in unwounded tissue are labeled by mCherry.NLS driven by the *Gal4/UAS* system. During mitosis, the fluorescence signal evident at 0 min disperses when the nuclear envelope breaks down, seen within circles in panels at 15 min and 45 min, before reappearing as two distinct/punctate nuclei at 100 min. (C) A schematic showing the diffusion of mCherry.NLS out of the nucleus during mitosis and its concentration in nuclei again after the nuclear envelope reforms in the daughter cells. Thus, the localization of mCherry.NLS reports nuclear membrane integrity. Scale bar = 25 μm.

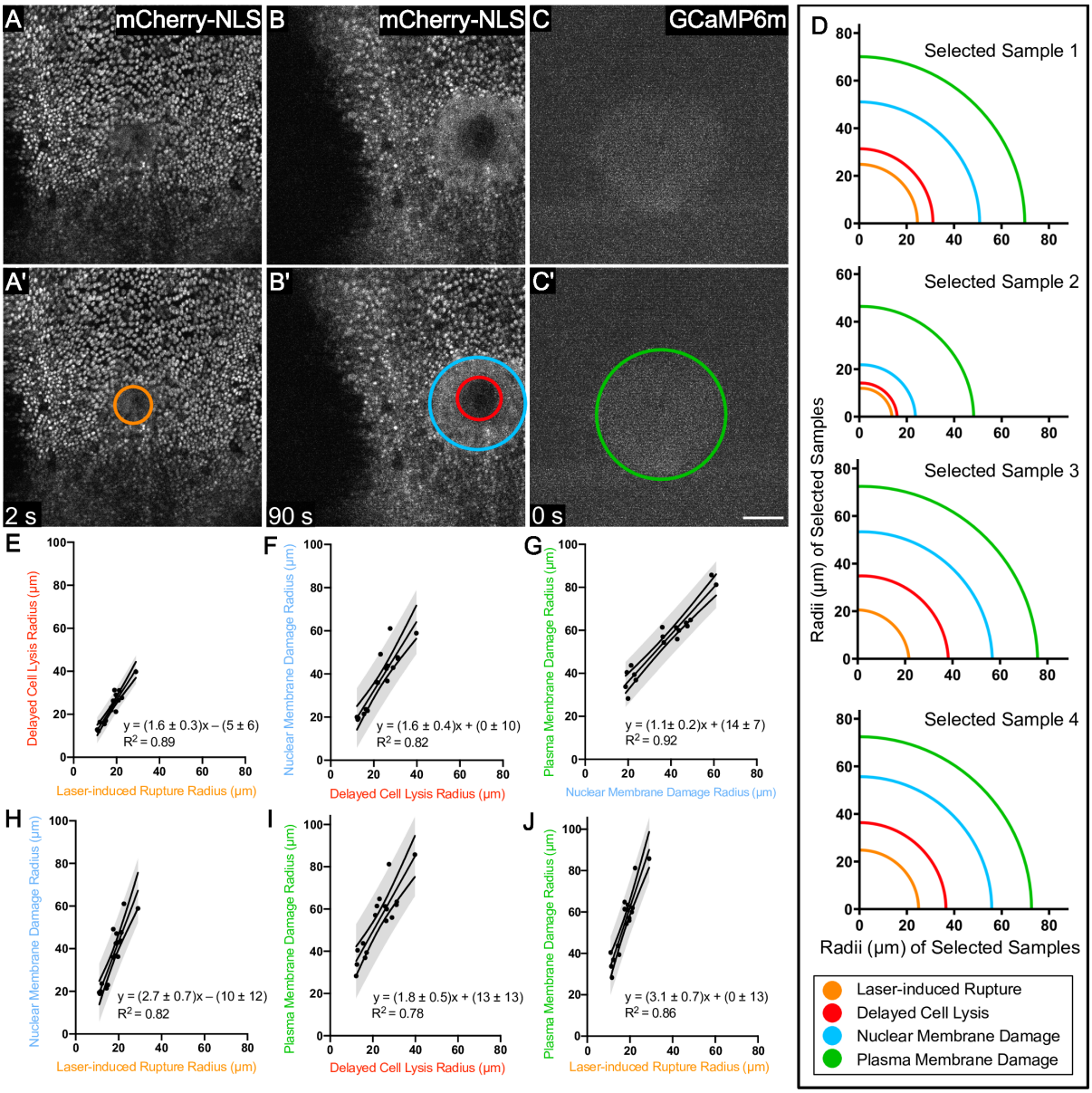

Chapter 3, Figure 2: Several zones of damage are evident around pulsed-laser wounds. (A) The region of laser-induced rupture is observed as the area of disrupted mCherry.NLS within the first two frames after wounding (here 2 seconds), annotated with an orange circle in A'. (B) The region of delayed cell lysis is observed as the complete loss of mCherry.NLS at 90 seconds, (red circle in B') and the region of nuclear membrane damage is observed as a diffuse, non-nuclear mCherry.NLS signal (light blue circle in B'), maintained within the cells by the plasma membrane at 90 seconds after wounding. (C) The region of plasma membrane damage is observed as an increase in cytoplasmic calcium levels immediately after wounding (green circle in C', as reported by GCaMP6m, a fluorescent calcium indicator, in the first frame after wounding (here 0 seconds). In this region, the wound creates microtears in the plasma membrane, allowing immediate influx of extracellular calcium. All images are of the same wound; the frame is shifted in B,B'. (D) Actual measurements of radii in four different samples demonstrates a consistent relationship between these regions; as any one of these regions increases in radius, the others likewise increase in radius. Panels E-J quantify this trend with 95% prediction bands. n = 17 pupae. Scale bar = 50 µm.

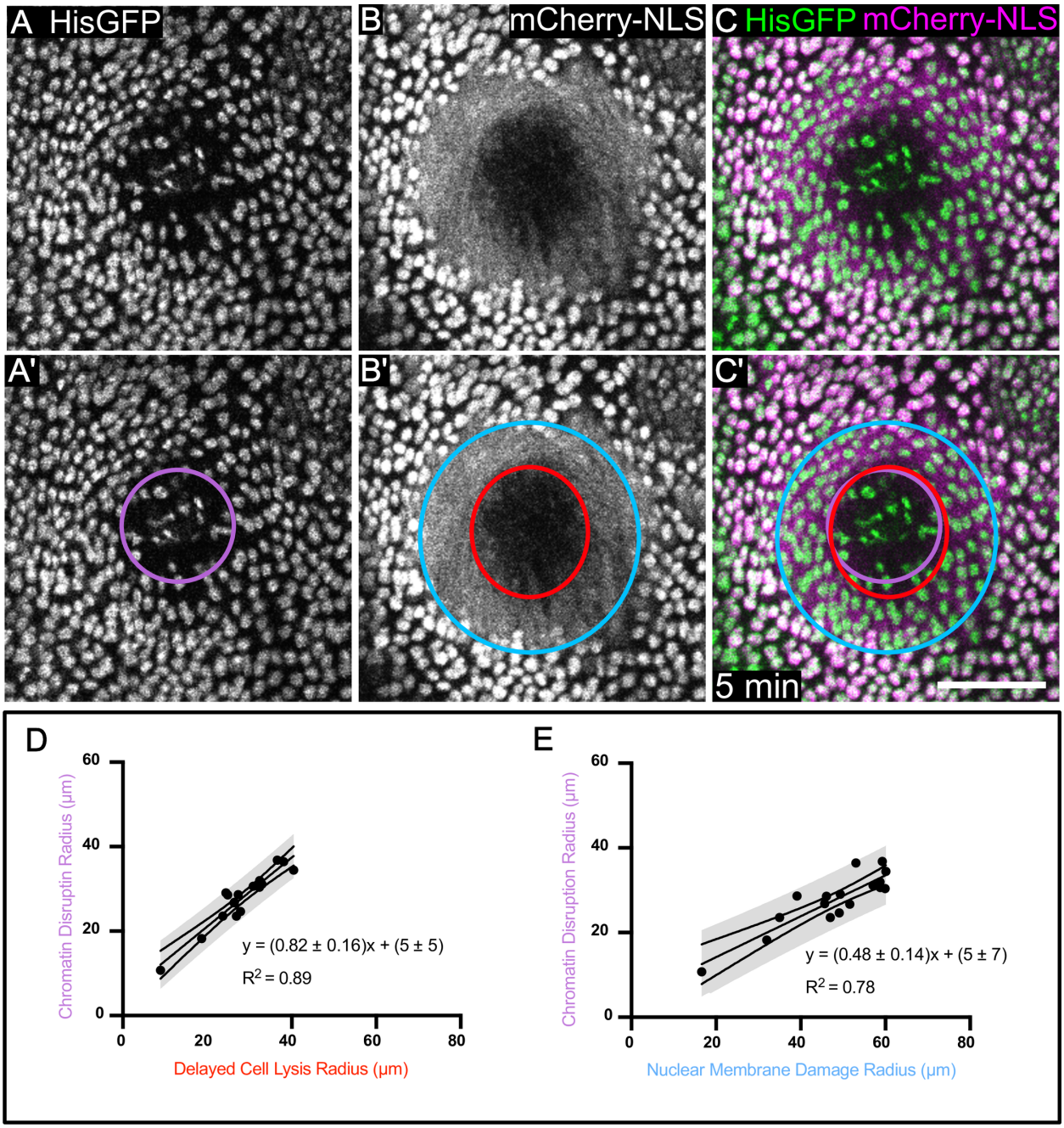

Chapter 3, Figure 3: Histones reveal that within the region of nuclear membrane damage, some nuclei have intact chromatin whereas nuclei closer to the center have disrupted chromatin.

(A) His2Av-GFP, which labels histones in chromatin, reveals a damage region with misshapen chromatin and decreased fluorescence, indicated with a purple circle in A'. (B) mCherry.NLS in the same wound reveals the region of nuclear membrane damage, (blue circle in B') and the region of delayed cell lysis (red circle in B'). (C) The overlay of His2Av-GFP with mCherry.NLS shows that the region of chromatin disruption is much smaller than the region of nuclear membrane damage, but similar in size to the region of delayed cell lysis. (D-E) The relationships between the region of chromatin disruption and the regions of nuclear membrane damage (D) and of delayed cell lysis € are linear. The 95% confidence interval is indicated. n = 17 pupae. Scale bar = 50 µm.

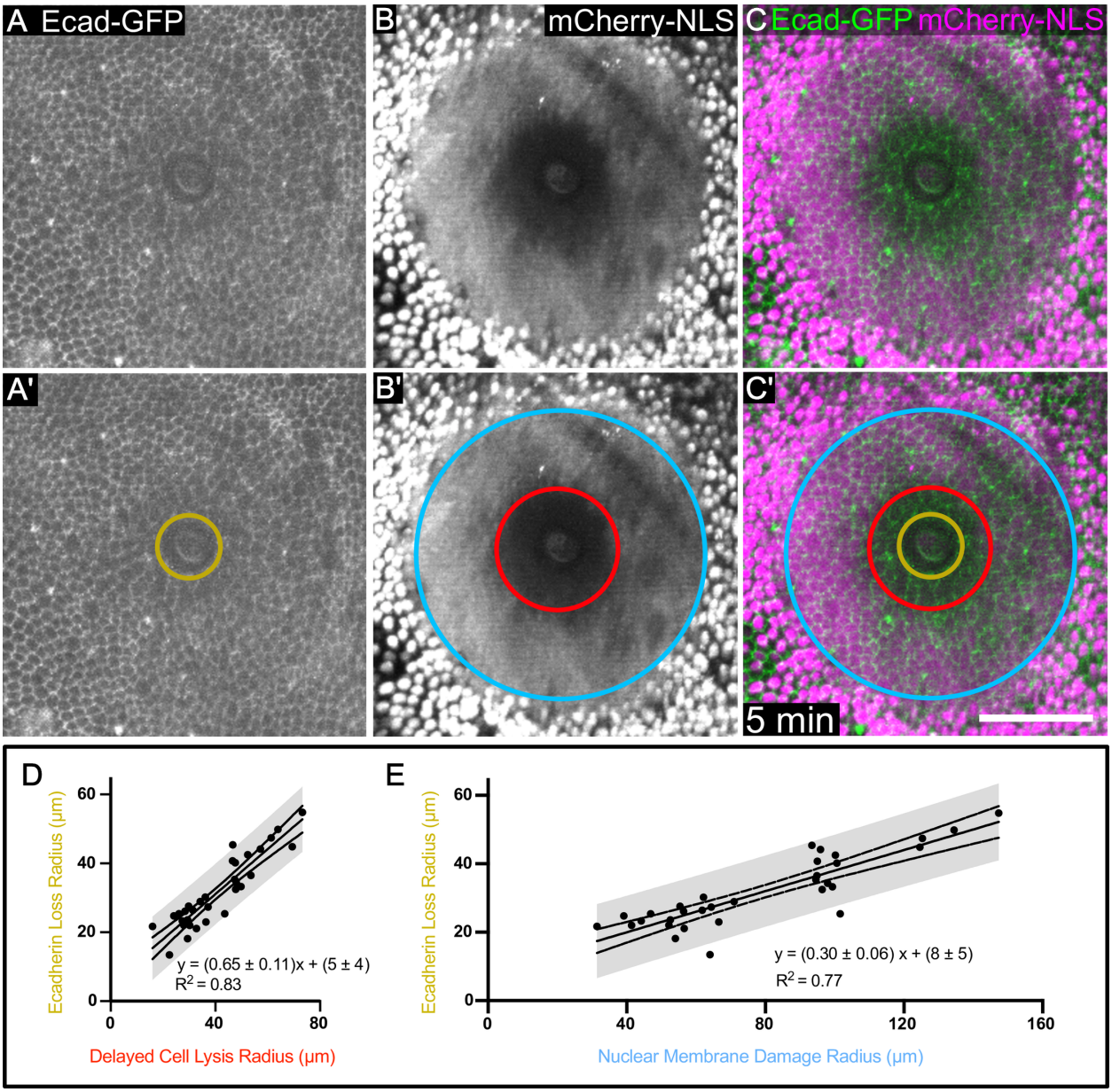

Chapter 3, Figure 4: Cell borders are disrupted following wounding.
(A) Genetically encoded Ecadherin-GFP marks cell borders and reveals damage around a pulsed-laser wound. The region of immediate Ecadherin-GFP loss is indicated with a gold circle in A'. (B,C) The region of immediate Ecadherin loss is distinct from and within the regions of delayed cell lysis (red circle) and nuclear membrane damage (blue circle). (D) The relationship of the radius of delayed cell lysis to the radius of immediate Ecadherin loss is linear. (E) The relationship of the radius of nuclear membrane damage to the radius of immediate Ecadherin-loss is linear. 95% prediction interval is indicated in D,E. n = 32 pupae. Scale bar = 50 µm.

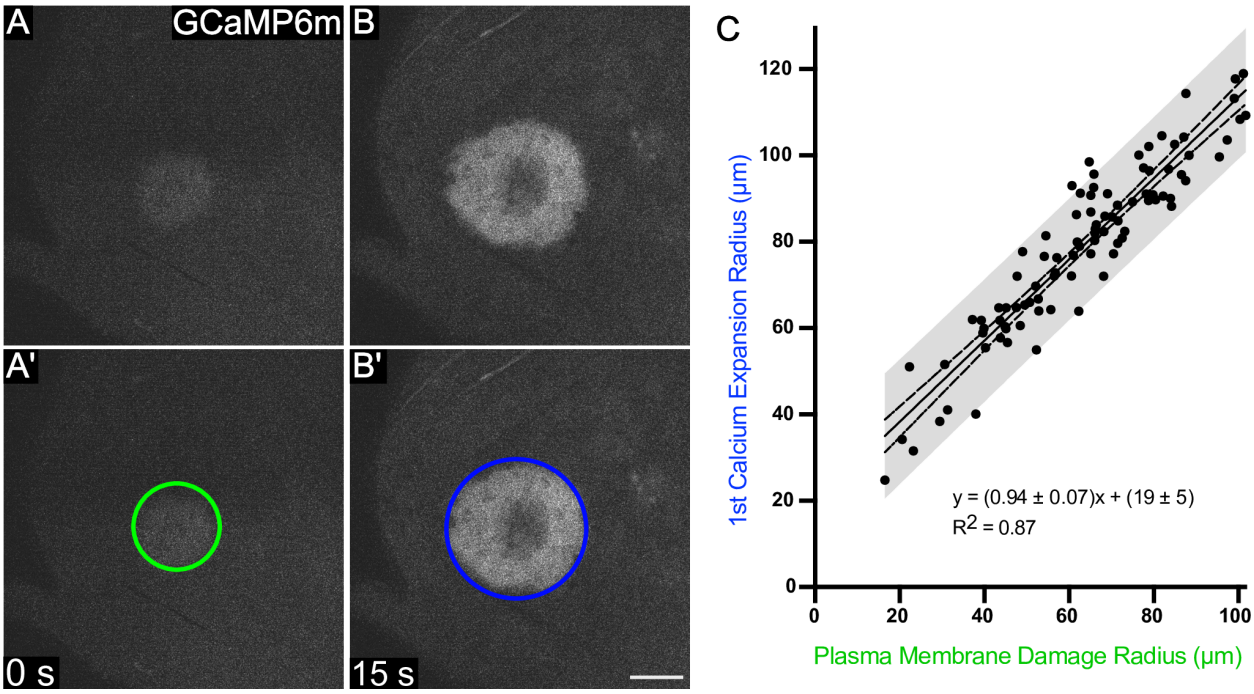

Chapter 3, Figure 5: The first expansion of calcium extends about 20 µm from the region of plasma membrane damage, independent of wound size.
(A) The influx of calcium immediately after wounding identifies cells with plasma membrane damage. This region is observed by an immediate increase in GCaMP fluorescence, indicated by a green circle in A'. (B) The calcium radius increases over the next ~15 seconds[14], and the maximum first expansion region is indicated with a dark blue circle in panel B'. The relationship between the plasma membrane radius and the first expansion radius is linear. Because the slope is ~1, the y-intercept of 19 indicates that the 1st expansion radius is expected to be ~20 µm larger (~2 to 4 cell diameters) than the radius of plasma membrane damage, regardless of wound size or laser energy. n = 92 pupae. Scale bar = 50 µm.

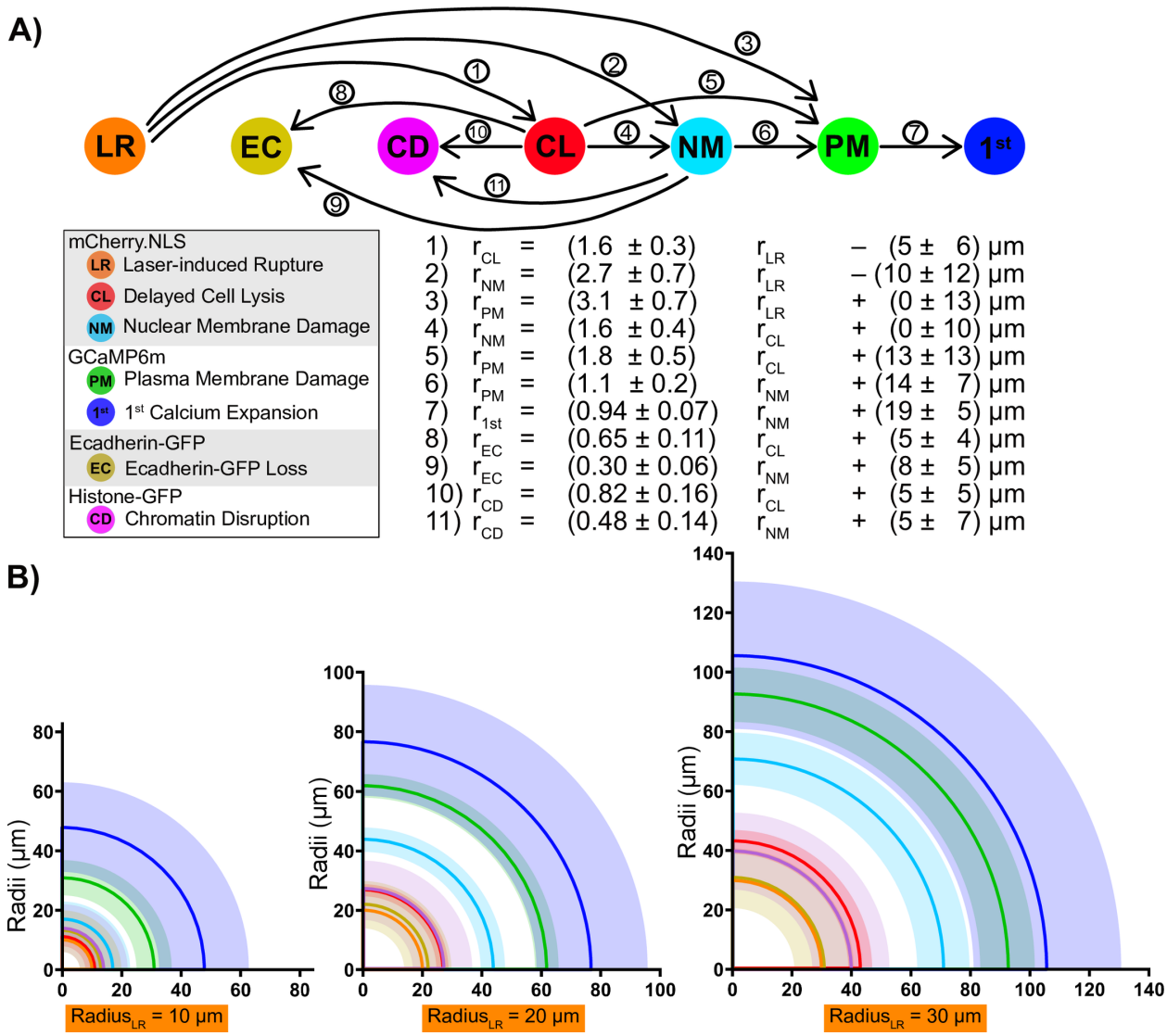

Chapter 3, Figure 6: Each zone of damage can be estimated given one of them.
(A) Schematic of how to calculate each zone of damage value from a given one, with each of the eleven linear equations displayed below corresponding to the arrows above. Arrows go from independent variable (x) to dependent variable (y), corresponding to equations 1–11 derived in Figs 2-5. The complete set of 42 equations necessary to relate each of the 7 zones of damage were derived according to the Materials and Methods and are provided in S2 Dataset. (B) Three hypothetical wounds are indicated, each with a different initial laser-induced rupture radius (10, 20, or 30 μm). The equations in S2 Dataset were used to derive the radii of the six other zones of damage from the given laser-induced rupture radius. The 95% confidence intervals are displayed for all values. With a radius of 10 μm, the first four regions overlap (laser-induced rupture, immediate Ecadherin loss, chromatin disruption, delayed cell lysis). Because the average cell diameter in this tissue is ~7 μm, the overlap suggests that these four regions may be within one cell diameter. As the wound gets larger, the regions become more distinguishable.

SUPPORTING INFORMATION

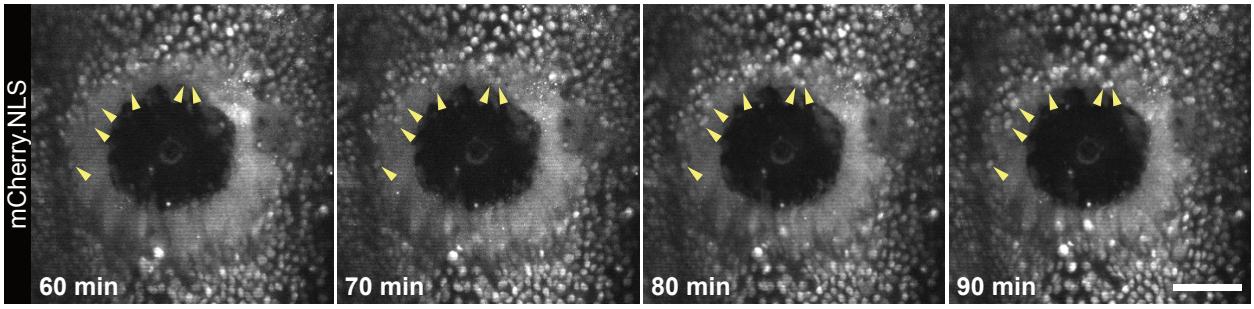

Chapter 3, S1 Figure: **Some cells with nuclear membrane damage recover.** Timelapse depicting diffuse mCherry.NLS signal from the region of nuclear membrane damage at 60 minutes returning to nuclei and becoming punctate at 90 minutes post-wound (arrowheads). This process occurs progressively over the course of 2-3 hours after wounding and the arrowheads represent a small selection of the nuclei around a wound that undergo this behavior throughout the repair process. Scale bar = 50 µm.

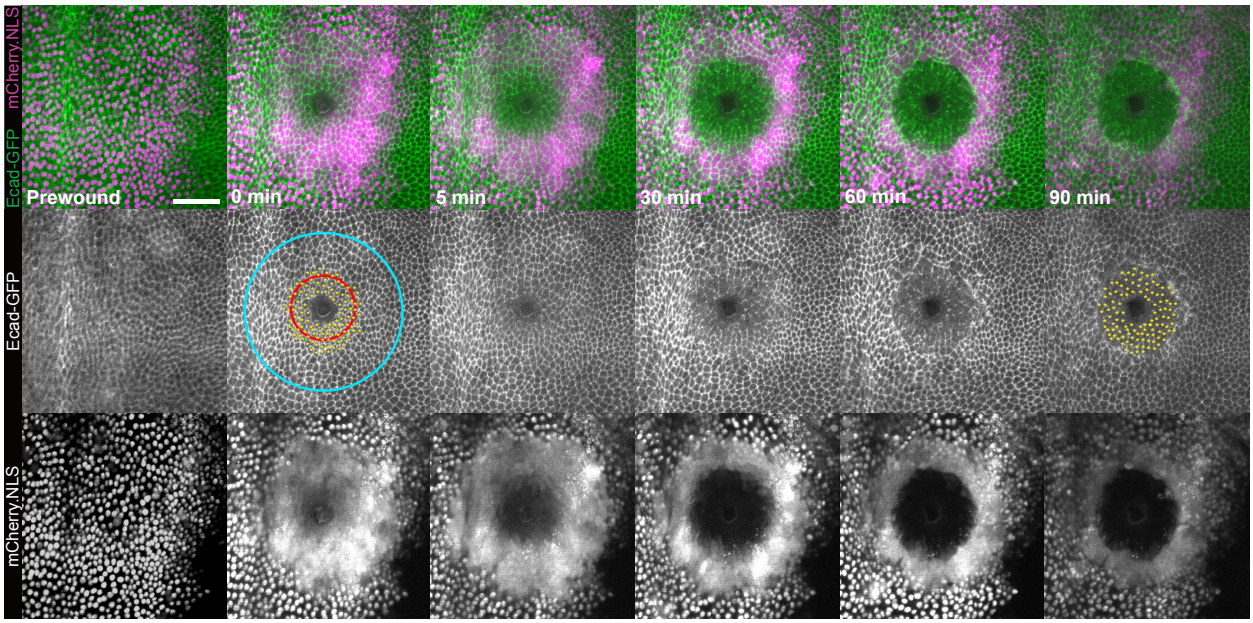

Chapter 3, S2 Figure: The region of Ecadherin loss expands over 90 minutes.

Timelapse of Ecadherin-GFP (green) and pnr>mCherry.NLS (magenta) following wounding, from S1 Movie. Immediately after wounding (0 min), Ecadherin is lost from the center of the wound and looks substantially similar by 5 min after wounding, as analyzed in Fig 4; by 90 minutes, the region of Ecadherin loss is much larger. During these ~90 minutes, Ecadherin-GFP appears to be gradually lost evenly across the region of delayed cell lysis (red circle), which was estimated by the loss of mCherry.NLS at 5 min. Cells that appear intact at 0 and 5 min but eventually lose Ecadherin have clearly died (labeled with yellow asterisks at 0 and 90 min). The region of nuclear membrane damage (blue circle) is evident by mCherry.NLS escaping from the nucleus immediately after wounding. Some cells with nuclear membrane damage recover whereas those closer to the center die, as illustrated by their recovering the mCherry.NLS signal and maintaining Ecadherin-GFP. n = 5 pupae. Scale bar = 50 µm.

Chapter 3, S1 Movie, S1 Dataset, or S2 Dataset, can be found in the supplementary material of O'Connor, et al. *PLOS One* 2021.[136]

Chapter 3, S1 Movie: The region of Ecadherin loss expands over 90 minutes.

Timelapse movie of Ecadherin-GFP (green) and pnr>mCherry.NLS (magenta) over 90 minutes following wounding. Movie shows Ecadherin gradual loss in cells that initially appeared intact**.**

Chapter 3, **S1 Dataset**

Minimal data set containing the radius determined for each sample used in this study, organized by Figure. This dataset also includes the values for the linear regression analyses used to derive Equations 1–22.

Chapter 3, **S2 Dataset**

Data set containing Equations 1–42, which can be used to approximate any zone of damage from a single known zone. Sheet "Total Equations List" lists all 42 equations with the necessary information to derive confidence intervals when using these equations. The other seven sheets allow the user to enter a single known radius value for one of the respective zones of damage in cell "B1", and the approximate radii of the remaining six zones of damage will be automatically calculated in cells "B4–B9", with 95% confidence intervals and expected ranges automatically calculated in cells "C4–E9".

CHAPTER 4

PROTEOLYTIC ACTIVATION OF GROWTH-BLOCKING PEPTIDES TRIGGERS CALCIUM RESPONSES THROUGH THE GPCR MTHL10 DURING EPITHELIAL WOUND DETECTION

This chapter is adapted from: O'Connor, JT., Stevens, AC., Shannon, EK., Akbar, FB., LaFever, KS., Narayanan, NP., Gailey, CD., Hutson, MS., Page-McCaw, A. Proteolytic activation of Growth-Blocking Peptides triggers calcium responses through the GPCR Mthl10 during epithelial wound detection. *Dev Cell*. Volume 56, Issue 15, 9 August 2021, Pages 2160-2175.

ABSTRACT

The presence of a wound triggers surrounding cells to initiate repair mechanisms, but it is not clear how cells initially detect wounds. In epithelial cells, the earliest known wound response, occurring within seconds, is a dramatic increase in cytosolic calcium. Here we show that wounds in the *Drosophila* notum trigger cytoplasmic calcium increase by activating extracellular cytokines, Growth-blocking peptides (Gbps), which initiate signaling in surrounding epithelial cells through the G-protein coupled receptor, Methuselah-like 10 (Mthl10). Latent Gbps are present in unwounded tissue and are activated by proteolytic cleavage. Using wing discs, we show that multiple protease families can activate Gbps, suggesting they act as a generalized protease-detector system. We present experimental and computational evidence that proteases released during wound-induced cell damage and lysis serve as the instructive signal: these proteases liberate Gbp ligands, which bind to Mthl10 receptors on surrounding epithelial cells, and activate downstream release of calcium.

INTRODUCTION

When a tissue is wounded, the cells surrounding the wound rapidly respond to repair the damage. Despite the non-specific nature of cellular damage, there is remarkable specificity to the earliest cellular response: cells around the wound increase cytosolic calcium, and this damage response is conserved across the animal kingdom [6–17]. The calcium response is not limited to cells at the wound margin, but extends even to distal cells [6–8,10]. Multiple molecular mechanisms have been identified that regulate wound-induced gene expression or cell behavior downstream of calcium [6–8,10,20,96,130,143,144], but the upstream signals remain unclear. How exactly do cells detect wounds? Here we investigate the molecular mechanisms by which a wound initiates cytosolic calcium signals.

The immediate increase in cellular calcium in turn initiates repair or defense responses. Calcium has been well-established as a versatile and universal intracellular signal that plays a role in the modulation of numerous intracellular processes. Several calcium-regulated processes are required for proper wound repair, including actomyosin dynamics [6,20,66,72,145,146], JNK pathway activation [96] and plasma membrane repair (reviewed in Cooper and McNeil, 2015). Unsurprisingly, an increase in cytosolic calcium is necessary for wound repair [9,10,13,20,143].

Nonetheless, there is less clarity on the mechanisms that trigger increased cytosolic calcium in cells near to and distant from the wound. In some cases, wound-induced cytoplasmic calcium enters from the extracellular environment, either directly through plasma membrane damage [13–15,20,96,143] or through calcium ion channels like TrpM [6,7,9]. In others, calcium is released from the endoplasmic reticulum (ER) through the IP_3 Receptor [9,13,16,17,41,42], and initiated by an unknown G-Protein Coupled Receptor (GPCR) or Receptor Tyrosine Kinase (RTK). Further, calcium responses can be initiated by mechanical stimuli alone [42,147–149]. Elucidating the mechanisms by which calcium signaling is triggered *in vivo* is critical to

understanding how wound information is transmitted through a tissue in order to change cellular behavior and properly repair the wound.

By live imaging laser wounds in *Drosophila* pupae, we previously showed that damaged cells around wounds become flooded within milliseconds by extracellular calcium entering through microtears in the plasma membrane [14]. Although this calcium influx expands one or two cell diameters through gap junctions, it does not extend to more distal cells. Strikingly, after a delay of 45-75 seconds, a second independent calcium response expands outward to reach a larger number of distal cells. Here we identify the relevant signal transduction pathway and receptor, the GPCR Mthl10. Downstream, signals are relayed through Gαq and PLCβ to release calcium from the ER. Upstream, Mthl10 is activated around wounds by the cytokine ligands Growth-blocking peptides (Gbps). Further, we provide experimental and computational evidence that the initiating event for the distal calcium response *in vivo* is a wound-induced release of proteases that activate the latent Gbp cytokines, cleaving them from inactive/pro-forms into active signaling molecules.

RESULTS

To investigate the calcium responses after wounding, we analyzed *Drosophila* pupae (Chapter 4, Figure 1A), which are amenable to live imaging *in vivo* because they are stationary throughout development. By partially removing the pupal case, we were able to access and wound the epithelial monolayer of the dorsal thorax, termed the notum (Chapter 4, Figure 1A, white box). After wounding and imaging, nearly all wild-type pupae recovered to eclose as adults.

The calcium responses observed after wounding are temporally and spatially complex and somewhat variable [14], making it more difficult to identify underlying mechanisms by comparing wild-type and mutant animals. To circumvent this problem, we exploited the radial

symmetry of the calcium response by manipulating gene expression on only one side of the wound, allowing us to assess symmetry in control versus experimental regions. We used the *Gal4/UAS* system to manipulate gene expression in the central region of the notum with *pnr-Gal4* (Chapter 4, Figure 1A'), and then wounded on the margin between the control and knock-down region, so that half the wound served as an internal control (Chapter 4, Figure 1B, C). We monitored the symmetry of the calcium responses with a ubiquitously expressed calcium reporter, *ActinP-GCaMP6m*, comparing the experimental (*pnr*) domain with the adjacent internal control. When no other genes are manipulated, the calcium signals remain radially symmetric about the wound (Chapter 4, Figure 1D, Movie 1).

The distal calcium response signals to release calcium via IP_3.

We first used this internally controlled system to knock down gap junctions, which we have previously shown to be required for the first calcium expansion [14]. As expected, the first expansion did not occur in the gap junction knockdown region but did in the control region (Fig. S1A). Importantly, the second distal calcium response still occurred in the gap junction knockdown region, although it appeared "speckled" because each cell transduced the signal independently of its neighbors (Chapter 4, Figure S1A), as has been reported previously [14,42,150]. This result indicated that the initiation of the distal calcium response requires neither gap junctions nor the first (gap junction-dependent) expansion.

To determine whether the calcium of the distal response was coming from internal stores within the cell, we knocked down IP_3 Receptor (IP_3R), which controls calcium release from the endoplasmic reticulum. Knocking down IP_3R on one side of the wound using our internally-controlled system demonstrated that it is absolutely required for the distal calcium response (Chapter 4, Figure 1E). Importantly, the effect was limited to the experimental domain, while the control domain calcium response remained intact. We confirmed this result with two

independent RNAi lines and an IP_3 sponge (Chapter 4, Figure S1B) and concluded that calcium is released from intracellular stores in an IP_3-dependent manner.

The IP_3 signal transduction pathway has been well studied. IP_3 is generated via hydrolysis of phosphatidylinositol 4,5-bisphosphate (PIP_2) into IP_3 and diacylglycerol (DAG), a reaction catalyzed by the enzyme phospholipase C beta (PLCβ). To test the role of PLCβ, we knocked it down on one side of the wound and found that PLCβ is required for the distal calcium response (Chapter 4, Figure 1F). This result was obtained with two independent RNAi lines. As the next step upstream, PLCβ is most commonly activated through the G_q-signaling pathway; activation of a G-protein coupled receptor causes the α-subunit of the G_q-heterotrimer (known as Gαq) to dissociate from its β and γ subunits to activate PLCβ. Indeed, previous literature studying IP_3-mediated calcium responses following injury have also implicated Gαq [9,43]. To test the role of G_q-signaling, we knocked down Gαq on one side of the wound and found that it was also required for the distal calcium response (Chapter 4, Figure 1G, Movie 2). These results demonstrate that the distal calcium response is transduced via the canonical G_q-signaling pathway.

Importantly, although all of the above experiments used laser wounding, we find that puncture wounds also had two distinct calcium waves: the first occurred immediately and required gap junctions; the second was delayed by tens of seconds and similarly required the G_q pathway (Chapter 4, Movie 3). Thus, the mechanisms underlying the two calcium responses appear to be general wound responses, not specific to laser ablation.

Interestingly, a modification of our internally controlled system suggests that wound-induced signals can diffuse in the extracellular space. Rather than wounding on the *pnr* domain border, we wounded in the middle of a *pnr* domain where Gαq was knocked down. As expected, no distal calcium response occurred within the knockdown domain, but the calcium response

did jump the gap of knockdown cells to suddenly appear in the even more distal control domain (Chapter 4, Figure 1H, Movie 4).

To quantify how gene knockdown alters the distal calcium response, we calculated the difference in maximum calcium-signal radius in the control and experimental regions (illustrated in Chapter 4, Figure 1E'). Each G_q-pathway knockdown significantly inhibited the calcium response (Chapter 4, Figure Fig. 1I). Taken together, the distal calcium response occurs through a G_q-signaling pathway likely activated by a diffusible signal.

The distal calcium response requires the GPCR Mthl10

The requirement of G_q suggested that the distal calcium response is initiated by a GPCR; however, given previous reports that the TrpM ion channel could alter the intensity of wound-induced calcium responses in the pupal notum [6,7,9], we first knocked down TrpM with either of two previously-used functional RNAi lines. Neither had a discernible effect on the timing or range of the calcium response: the experimental domain remained symmetrical to its internal control (Chapter 4, Figure 2A, D). Next, we knocked down candidate GPCRs, prioritizing receptors with known epithelial expression and G_q activity [151]. Previous cell-culture studies have implicated ATP as a ligand activating calcium after wounding [43], and a recent study in mice implicated ADP in intercellular calcium waves following viral infection [152]. We thus knocked down *AdoR*, the only *Drosophila* adenosine receptor, but it had no effect on the calcium response (Chapter 4, Figure 2B, D). We then knocked down the GPCRs *Tre1* or *TkR86C*, both implicated in wound responses [117,153], but they also had no effect on the calcium response (Chapter 4, Figure 2D). Strikingly, we were able to completely eliminate the distal calcium responses by knocking down the cytokine-activated GPCR *Methuselah-like 10 (Mthl10)*[154] (Chapter 4, Figure 2C, D, Movie 5). We confirmed this result with two independent RNAi lines. To test whether *Mthl10* is important for wound recovery, we measured pupal

survival after large wounds and found that *Mthl10* knockdown throughout the notum decreased pupal survival by ~30% (Chapter 4, Figure 2E).

Mthl10 is activated by Gbp1 and Gbp2

Mthl10 is known to be activated by a class of cytokines known as Growth-blocking peptides (Gbps), of which there are five in *Drosophila* [154,155]. Gbps are synthesized in the *Drosophila* fat body in a latent pro-peptide form, requiring proteolytic cleavage for activation [155–159]. Because Gbps are secreted (and thus not cell-autonomous), the internally controlled knockdown approach expressing an RNAi exclusively in epithelial cells would not be effective at testing their role; we instead needed to test homozygous Gbp knockout pupae. We used CRISPR to generate individual null mutants of *Gbp1* or *Gbp2* (hereafter referred to as $Gbp1^{\Delta}$ and $Gbp2^{3\Delta FS}$, respectively; Chapter 4, Figure 3A), and obtained the previously generated and homozygous viable strain *Df(2R)Gbp-ex67*, which has a small chromosomal deletion removing the neighboring genes *Gbp1* and *Gbp2* [160] (hereafter referred to as Δ*Gbp1,2;* Chapter 4, Figure 3A). Upon wounding these animals, we found the individual null mutants of *Gbp1* or *Gbp2* did not appear to have an altered calcium response compared to control (Chapter 4, Figure 3B–D). However, the Δ*Gbp1,2* pupae lacked a normal distal calcium response in 13 out of 14 pupae (Chapter 4, Figure 3E).

Because this method does not have an internal control, we analyzed the spatiotemporal dynamics of the distal calcium responses using the following metrics: (1) its relative spatial extent via $(R_{Max} – R_{1st})/R_{1st}$, where R_{Max} is the maximum calcium-signal radius and R_{1st} is the radius of the first expansion (illustrated in Chapter 4, Figure 3B'), which provides normalization for wound size (Chapter 4, Figure 3G); (2) its duration via the time over which the calcium-signal radius remained greater than R_{1st} (Fig. 3H); and (3) its start time (Chapter 4, Figure 3I). The spatial quantification showed that Δ*Gbp1,2* significantly reduces the radius of the distal calcium response. The vast majority of Δ*Gbp1,2* samples actually had values at or near zero because

there was no distal expansion. On the other hand, the individual null mutants had robust distal expansions that were not significantly different from controls (Chapter 4, Figure 3G). We obtained similar results for quantification of the distal calcium response duration: Δ*Gbp1,2* signal duration was significantly reduced compared to control (Chapter 4, Figure 3H), whereas that of the individual nulls was either unchanged (Gbp1$^{\Delta}$) or even increased (*Gbp2*$^{3\Delta FS}$). In those samples for which there was a distal calcium response, none of the nulls showed a significant difference in the response start time (Chapter 4, Figure 3I).

Taken together, this data shows that the absence of both *Gbp1* and *Gbp2* significantly decreases the response radius and duration, while that of *Gbp1* or *Gbp2* alone does not. Each extracellular ligand, Gbp1 or Gbp2, is independently sufficient to relay wound information to surrounding cells.

If Gbps are wound-induced signals that direct cells to increase calcium, then ectopic Gbp would be expected to activate a calcium response, even without a wound. Unfortunately, the pupal notum is protected by an impermeable cuticle that makes it impossible to add Gbp directly to the tissue, and it cannot be removed without wounding. We thus turned to larval wing discs, sacs of epithelial tissue that have no cuticle. We applied synthetic active-form Gbp peptides directly to wing discs *ex vivo* at varying concentrations. Excitingly, we found that both Gbp1 and Gbp2 elicited a strong calcium response in wing discs when added *ex vivo* at 5 nM or 50 nM, respectively (Chapter 4, Figure 4A, B). To test whether these responses were Mthl10-dependent, we mounted one control and one *Mthl10* knockdown disc side-by-side in a media bubble and added Gbp peptide to both discs simultaneously. As expected, the calcium responses were absent from the *Mthl10* knockdown discs (Chapter 4, Figure 4C, D, Movie 6). Finally, we asked whether the three other Gbps could elicit calcium in wing discs and found that Gbp4 and Gbp5 could elicit calcium consistently at 50 nM (and Gbp4 occasionally even at 5 nM), while Gbp3 was not effective, even at 50 μM, the maximum concentration tested (Chapter 4, Figure S2). Despite the activity of these other Gbps *ex vivo*, the loss of the distal calcium

response in the Δ*Gbp1,2* pupae indicates Gbp1 and Gbp2 are responsible for the calcium increase in the pupal notum.

Gbps and Mthl10 are required for calcium waves in wing discs

Previous studies have shown that wing discs cultured *ex vivo* displayed potent calcium responses upon exposure to fly extract [42,149,150]. Because fly extract is created by lysing and homogenizing whole flies, we hypothesized that it contained wound-induced signals that activate wound-detection pathways in wing discs to initiate calcium responses. Indeed, we observed the calcium response was *mthl10*-dependent by adding fly extract to control and *mthl10* knockdown wing discs simultaneously (Chapter 4, Figure 4F, H, Movie 7). Since extract of adult flies is predicted to contain both Gbp4 and Gbp5, which may be confounding variables, we also tested extract made from larvae, a stage that expresses only Gbp1-3 [155]; like adult extract, wild-type larval extract activated calcium responses in wing discs in an *mthl10*-dependent manner (Chapter 4, Figure 4G, H, Movie 7). This shows that, in addition to the distal calcium response following wounding, Mthl10 mediates the lysate-induced calcium response in wing discs.

To determine whether the calcium-activating signal in the extract is Gbp, we added extract made from either wild-type or homozygous Δ*Gbp1,2* larvae to either control or homozygous Δ*Gbp1,2* wing discs (Chapter 4, Figure 5A, B). We found that no calcium response occurs when Gbps are absent from both disc and extract (Chapter 4, Figure 5B, C, Movie 8), demonstrating that the calcium response to larval extract does indeed require Gbp1 and/or Gbp2. Surprisingly, as long as Gbp was present in either the extract or the disc, the extract was able to elicit a calcium response. (Chapter 4, Figure 5A-C, Movie 8). The former result is expected: extract made from wild-type larvae contains Gbp, which elicits calcium when applied to wing discs. The latter result is less intuitive and suggests that the wing discs themselves maintain a local supply of Gbp that can be activated by larval extract. If the discs already have

Gbp, then what does the extract provide to activate calcium? This result suggested that proteases in the extract are necessary to cleave latent pro-Gbp from the disc to elicit the calcium response.

Gbps are activated by multiple proteases

Bioinformatics analysis predicted that both pro-Gbp1 and pro-Gbp2 could release their active C-terminal peptides after cleavage by several unrelated proteases [161]. To confirm the activity of proteases in the lysate, we tried to inhibit them using broad-spectrum protease inhibitors, singly and in combination. Unfortunately, the inhibitors or the vehicle (DMSO) alone at high enough concentrations could themselves induce calcium responses in wing discs, stymieing our ability to use inhibitors in this experiment. As an alternative approach, we noted that the serine protease trypsin and the cysteine protease clostripain are both predicted to cleave Gbp1 [161]. To test their ability to activate calcium in wing discs, we added trypsin or clostripain to wing discs and found that each was sufficient to elicit a calcium response in control but not Δ*Gbp1,2* wing discs (Chapter 4, Figure 5D-F). Given that cell lysis is known to release multiple active proteases, our data suggest a model in which wound detection in the *Drosophila* notum depends on latent pro-Gbps in the extracellular space, acting as protease detectors, reporting the presence of wound-induced cell lysis via Mthl10 signaling.

Enzymatic generation of a diffusible signal explains wound-size dependence

This protease/Gbp/Mthl10 model is substantially more complex than the delayed-diffusion model of an unknown signal we presented previously [14]. That initial model was based on instantaneous release and diffusive spread of a single, unknown wound-induced signal. Although it lacked mechanistic detail, the prior model fit the data well and provided a useful parameterization of response dynamics: a total amount of signal released compared to its detection threshold (M/C_{th}), a back-propagated time delay $t_{0,min}$ at which calcium signals first

become apparent, and an effective diffusion constant α_{eff} describing the rate at which signal spreads distally. A close look at these fitted parameters shows that the time delay and effective diffusion constant have definite trends with wound size (Chapter 4, Figure 6F,F'; n = 26 wounds with diameters > 15 μm).

The delayed-diffusion model can describe these trends, but the description does not provide explanatory power. We find that α_{eff} increases linearly with wound diameter w:

$$\alpha_{eff} = (0.77 \pm 0.26\ \mu m/s)\ w - (8 \pm 11\ \mu m^2/s),$$

whereas the trend for $t_{0,min}$ is better described by a linear dependence on $1/w$:

$$t_{0,min} = (1500 \pm 700\ \mu m\ s)\ w^{-1} + (12 \pm 19\ s).$$

The coefficients of the w or $1/w$ term are non-zero (with p-values of 0.006 and 0.04, respectively). Although one can postulate explanatory hypotheses, the delayed-diffusion model itself provides no reason for the wound-size dependence of the response dynamics. We thus wanted to explore whether the observed trends would fall out naturally from a more detailed model based on the protease/Gbp mechanism.

To do so, we constructed a computational reaction-diffusion model as outlined in Chapter 4, Figure 6A, A'. In brief, wound-induced cell lysis releases proteases that enzymatically cleave extracellular pro-Gbps into their active forms, which then reversibly bind Mthl10 receptors. This abstraction treats all classes of proteases as a single pool of temporally and spatially varying protease activity. It also pools all Gbp family members, but does keep track of pro- and active forms. Because Mthl10 is membrane bound, and pro-Gbp2 physically interacts with collagen IV [162], both species are treated as stationary in the model, but released proteases and active Gbps are allowed to diffuse. The model is solved over time and a 2D radially symmetric space for six species – protease, free active Gbp, and receptor-bound Gbp (Chapter 4, Figure 6B), as well as pro-Gbp, protease::pro-Gbp complex and free receptor. Signaling downstream of the receptor is approximated as a threshold event that releases

calcium from intracellular stores when a given fraction of receptors are bound by ligand (Chapter 4, Figure 6C, dashed line). For complete mathematical details, see Chapter 4, Supporting Text.

As constructed, this model has nine free parameters including protease release characteristics, initial component concentrations, diffusion constants, and reaction rates (see Reaction-Diffusion Model supplemental text and Chapter 4, Figure S5). Given that experimental response dynamics are adequately fit by a simpler model using just three parameters, one should not expect fits of the more detailed model to place strong constraints on all parameters. Instead, the detailed model falls into the category of “soft” or “sloppy” behavior common in systems biology [163]: parameters are weakly constrained, often varying over orders of magnitude, but predictions of model output are nonetheless robust and useful. In an attempt to provide stronger parameter constraints, we did try simultaneous fitting of multiple experimental data sets using a set of nine shared parameter values. Such fits did not describe the data well (Chapter 4, Figure S3A). As a second attempt, recognizing that wound size varied among experiments, we also tried simultaneous, multiple-data-set fits using seven shared biochemical parameter values and two experiment-specific wound parameters; however, this additional flexibility was still insufficient (Chapter 4, Figure S3B). We thus proceeded with fits of the full nine-parameter model to individual data sets and used the resulting parameter sets as the basis for comparing further model predictions with experimental data.

We selected four typical distal calcium responses and fit each calcium signal radius versus time to the reaction-diffusion model using a constrained least-squares approach (see Chapter 4, Supporting Text). For each experimental response, we conducted 32 fits with different randomly selected sets of initial parameter guesses. We used the single best fit to estimate the variance and kept all fits for which the chi-squared statistic indicated an equivalently good fit at the 95% confidence level (3-7 fits for each experiment). A single experimental response and model fit are shown in Chapter 4, Figure 6D, and a full grid of all

good fits is shown in Chapter 4, Figure S4A. As expected for a “soft” model, the superset of parameter estimates from all good fits yields distributions for individual parameters that vary by orders of magnitude (Chapter 4, Figure S4B).

Despite these variations among best-fit parameters, the model makes robust predictions for its output’s dependence on wound size. For each set of best fit parameters (a set being a group of nine parameters that yield a good fit), we solved the model with all parameters fixed, save two that scale with wound size: the $1/e^2$ radius of the protease source, which scales linearly with wound radius; and the total amount of protease activity released, which scales as wound radius squared. With these two parameters scaled in this manner, the peak density of the protease source (activity released per unit area) is held constant. As the example in Chapter 4, Figure 6E shows, increasing wound size in the model yields smaller time delays and more rapid diffusion-like signal spread. To better compare to experimental trends, we parameterized the detailed model output in the same way as experimental data, i.e., by fitting its calcium signal radius versus time to the three-parameter delayed-diffusion model. The resulting wound-size dependencies fall out as two natural predictions of the detailed model. First, the parameterization shows that the effective diffusion constant in the detailed model output increases with wound size around every one of the widely varying best-fit parameter sets (each colored line in Chapter 4, Figure 6F). Although individual curves flatten out as α approaches zero, the trends are mostly linear and the slopes are comparable or greater than the trend observed across all experiments. Second, the parameterization shows that the signaling time delay in the detailed model varies in a roughly hyperbolic manner with wound size. These predicted trends are also similar to experiments (Chapter 4, Figure 6F’).

Within the detailed model, the wound-size-dependence for the time delay and spread rate of the distal response can be traced to a generalized mechanism with two key structural features. First, the signal (i.e., active Gbp) builds up gradually over time. Second, the signal diffuses rapidly enough during this build up to spread well beyond the spatial extent of its

source. The first feature by itself provides both a time delay associated with reaching threshold and a diffusion-like spread associated with the threshold boundary moving further from the wound as signal builds; however, it does not yield a wound-size dependence. Even though smaller wounds produce smaller amounts of protease activity and thus smaller integrated signals, they do so over smaller areas to yield the same signal density as larger wounds. The second key structural feature, relatively rapid diffusional spread, ensures that signals from small or large wounds are spread over comparable areas, decreasing the signal density for smaller wounds, increasing it for larger wounds. This signal density difference yields the observed wound-size dependence for α and $t_{0,\min}$.

Using the computational model, we are able to recapitulate key features of the calcium response. For example, we modeled the same parameters in a control vs a 70% reduction in Mthl10 levels (Chapter 4, Figure 7A) and found this matches the observed response in our internally-controlled system where Mthl10 is knocked down on one side of the wound while an internal control is maintained (Chapter 4, Figure 7B). We also modelled variations of extracellular pro-Gbp levels and found that, for the best-fit parameter sets, decreasing pro-Gbp levels are predicted to decrease the spatial extent and duration of the calcium response (four model output examples shown in Fig. 7C). In experiments, we observed similarly modified responses in the double null Δ*Gbp1,2*, but not in the individual null mutants of *Gbp1* or *Gbp2* (Chapter 4, Figure 3). Since the Gbp reduction in individual nulls was perhaps insufficient to measurably alter the calcium response, we revisited this experiment using trans-heterozygotes of the Δ*Gbp1,2* deletion and one of the individual null mutant alleles (*Gbp1*$^{\Delta}$ or *Gbp2*$^{3\Delta FS}$). The resultant pupae expressed only one allele of *Gbp1* and were null for Gbp2 *(*Δ*Gbp1,2/ Gbp2*$^{3\Delta FS}$) or expressed one allele of *Gbp2* and were null for *Gbp1* (Δ*Gbp1,2/ Gbp1*$^{\Delta}$*).* We wounded each of these pupae and compared their distal calcium responses to controls and found that the spatial extent was significantly decreased in both conditions compared to controls (Chapter 4, Figure 7D). Furthermore, the response duration was decreased significantly in the pupae null for

Gbp1 and heterozygous for *Gbp2* (Chapter 4, Figure 7E). Interestingly, the start times (Chapter 4, Figure 7F) were not significantly different in either condition, which matches the very weak dependence of start time on Gbp levels in the model (Chapter 4, Figure 7C). These results experimentally validate the model prediction that sufficient reduction in pro-Gbp prior to wounding can decrease the spatial extent and duration of the calcium response.

Computational model identifies key role for cell lysis over time

In the detailed model construction used here (Chapter 4, Figure 6A), the rate of signal spread is controlled largely by the rate of signal accumulation plus the diffusion constant of active Gbp. Diffusive spread of the protease itself is minimal (Chapter 4, Figure 6B). The rate of signal accumulation itself is controlled by the rate constant for the release of protease activity via cell lysis, k_S, and the enzymatic rate constant for proteolytic cleavage of pro-Gbp, k_C. Among the set of best fits, these two model parameters can compensate for one another, as shown by their inverse correlation (Chapter 4, Figure 7G). One can be fast so long as the other serves as the sufficiently slow rate-limiting step in generating active Gbp. In most best-fit parameter sets, the rate-limiting step had a corresponding time constant ($1/k$) of 50-500 s. Interestingly, only a few of the best fits had a quick release of protease activity after wounding ($1/k_S < 1$ s) and modifying the model to force an instantaneous release of this activity failed to fit the experimental data. In other words, the model predicts that extracellular protease release occurs progressively over time after wounding, rather than all at once. Given that laser-induced wounds are made very rapidly – cavitation bubble generation and collapse occur within microseconds – the best-fits' requirement for much slower protease release was an unexpected prediction. We hypothesized that the key step may not be an instantaneous release of proteases from all damaged cells, but rather slow and progressive cell lysis. This led us to reexamine live imaging of nuclear-mCherry-labeled cells around wounds. Although a small number of cells were destroyed immediately by the ablation process, a much larger group of surrounding cells were

observed to lyse progressively over ~90 seconds, validating the model's prediction that the wound-induced cell destruction is not instantaneous (Chapter 4, Figure 7H).

Quantitative modeling based on the protease/Gbp mechanism thus provides explanations for the distal calcium response's wound-size dependencies, makes verified predictions regarding required extracellular pro-Gbp concentrations, and makes an unanticipated prediction about slow protease release that matches a reexamination of experimental data. Further model predictions are provided by the sensitivity analysis shown in Fig. S5. Several parameters have a strong impact on the timing and reach of the distal calcium response, including all those related to the release of protease activity, plus the rate constant for pro-Gbp cleavage, and the initial amount of pro-Gbp present in the extracellular space. It is especially interesting that the amounts of pro-Gbps have a strong impact on the calcium response, as these are known to vary with environmental conditions [160]. The inclusion of an extracellular enzymatic step in the wound-detection pathway provides both signal amplification and multiple options for regulation. Quantitative modeling provides a set of potentially experimentally testable predictions for how this regulation could function *in vivo*.

DISCUSSION

This study traces the induction of the repair process back to the wound itself. We find that for epithelial wounds in the *Drosophila* notum, the cell-surface receptor Mthl10 responds to Gbp ligands in the extracellular environment, triggering a cell-autonomous increase in cytoplasmic calcium. It was already known that Gbps are synthesized in an inactive pro-form, requiring proteolytic cleavage for activation, and that they are secreted by the fat body. We find that although Gbps are present in unwounded tissues, they activate Mthl10 only in the presence of a wound. Interestingly, Gbps have cleavage consensus sequences for multiple protease families. Further, the addition of cell lysate or the addition of the unrelated proteases trypsin or

clostripain to unwounded tissue is sufficient to generate a calcium signal in wing discs through Mthl10/Gbp signaling. These results lead us to a model in which the lysis of cells inherent in wounding releases non-specific cellular proteases into the extracellular environment. These proteases cleave and activate extracellular Gbps, which in turn activate the Mthl10 GPCR on cells around the wound, initiating wound-induced calcium signaling. Such cell lysis and protease release should be a general feature of cell destruction, whether caused by trauma, pathogen-induced lysis, or a lytic form of cell death such as pyroptosis or necroptosis (immunologically silent apoptosis may well be an exception [164]). A variety of epithelial damage mechanisms may thus converge through the Gbps to signal via the GPCR Mthl10 and alert surrounding cells to the presence of a nearby wound. This molecular mechanism is supported by a computational model which accurately describes the pattern and timing of wound-induced calcium, predicted its dependence on wound size and initial levels of Gbps, and directed us to observe that cell lysis is not immediate but rather takes place over 10s of seconds. Thus, we offer a model for how surrounding cells detect the damage of cell lysis, utilizing a Gbp-based protease detector system.

Two superimposed mechanisms increase cytoplasmic calcium around wounds

Laser-wounds generate complex yet reproducible patterns of increased cytoplasmic calcium, and the complexity of this pattern has undoubtedly made it difficult to unravel its underlying mechanisms. Within the first ~90 seconds after wounding, two mechanisms drive the increase of calcium, and the complexity is generated by the temporal and spatial superimposition of these two mechanisms. Previously, we reported that a different type of cellular damage initiates a different mechanism for increasing cytoplasmic calcium [14]. In that report, we identified wound-induced microtears in the plasma membranes of surviving cells, and these microtears provided an entry for extracellular calcium to flood into the cytoplasm and then flow out to neighboring undamaged cells via gap junctions. This direct entry of calcium through

damaged plasma membranes is evident within milliseconds after wounding. In this report we describe a second mechanism that extends to more distal cells, initiated by cell lysis at wounding. The dynamics of protease release from lysed cells, along with the gradual accumulation of active Gbp and its rapid diffusion, all contribute to the appearance of this distal calcium response 45-75 s after wounding. The earliest and closest cells to be activated by MthI10/Gbp signaling cannot be identified visually because the initial flood of calcium through microtears takes time to subside.

Three tools allowed us to decipher these superimposed mechanisms. The first tool was the laser itself, which generates a highly stereotyped pattern of damage within a circular wound bed. Although cell lysis and plasma membrane damage are features of nearly every wound, their reproducible pattern in a laser wound allowed us to distinguish the signaling mechanisms each type of damage potentiated. The second tool was a spatiotemporal analytical framework to measure radius over time, which clearly identified two peaks, the first induced by microtears and the second induced by cell lysis. The third tool was experimental, using RNAi-knock down of genes in a limited region and comparing it with an internal control. The ability to identify asymmetry between the control and experimental sides of wounds allowed us to bypass concerns about variable wound sizes, which otherwise would have made it difficult to recognize patterns and interpret data. Complex overlapping patterns may have obscured the mechanisms upstream of wound-induced calcium in other systems as well as ours.

Other upstream regulators of wound-induced calcium

Previous studies identified other molecules and phenomena upstream of wound-induced calcium. Studies in cell culture found that wound-generated cell lysis releases ATP, which diffuses extracellularly to bind to purinergic receptors and activate calcium release from intracellular stores [43,120,121,165–167]. Although reproducible in many types of cultured cells, there has been little evidence to support ATP signaling from lytic cells *in vivo*, likely because

extracellular ATP is rapidly hydrolyzed by nucleotidases *in vivo* [168]. Interestingly, ATP does appear to signal damage and promote motility in response to injuries associated with cell swelling in zebrafish, animals that inhabit a hypotonic aqueous environment; however, even in this wounding paradigm, ATP does not signal from lytic cells at an appreciable level [120]. We did not find evidence for ATP signaling upstream of calcium in our wounding experiments, as knockdown of the only fly adenosine receptor did not alter the calcium pattern around wounds.

Some *in vivo* studies have implicated a TrpM ion channel upstream of calcium release. This role of TrpM was first identified in laser-wounding studies of the *C. elegans* hypodermis [9], a giant syncytial cell where we would expect great overlap in the spatial extent of microtear-initiated calcium, which would diffuse quickly throughout a syncytium, and receptor-mediated calcium released from the ER. In the hypodermis, loss of TrpM reduced by half the intensity of wound-induced calcium signaling, but without spatial and temporal analysis, the exact contribution of TrpM is not known. In the *Drosophila* notum, a previous study identified TrpM as a regulator of wound-induced actin remodeling, and a slight reduction in wound-induced calcium intensity over time was noted in *TrpM* knockdowns [6]. In contrast, we did not observe any change in the spatial or temporal aspects of the calcium response in *TrpM* knockdown cells compared to the internal control, and given wound-to-wound variability it would have been hard to identify a small effect without an internal control. A study in the fly embryo determined that wound-induced calcium originates from both the external environment and internal stores [7], suggesting to us that two superimposed calcium response mechanisms may have been at play in these experiments. They found when *TrpM* was knocked down, calcium intensity was reduced by half, but again without spatial and temporal analysis or an internal control, it is difficult to know what pathway TrpM regulates.

Tissue mechanics are upstream of increases in cytoplasmic calcium in a non-wounding context. Several labs have reported calcium flashes and waves in unwounded wing discs, dissected from larvae and cultured *ex vivo* [41,42,150]. Cell and organ culture requires serum to

support metabolism outside the organism, and in fly culture, this “serum” is generated by grinding whole adult flies and collecting the supernatant. Because such serum would undoubtedly contain secreted signals from wounded cells, calcium signaling in wing discs *ex vivo* is probably a wound response; indeed, we found it to be transduced by the same mechanism as wound signals, requiring protease, Gbps, and Mthl10. One aspect of calcium signaling in wing discs that we have not tested in our wounding model, however, is the role of mechanical tension. In carefully controlled mechanical experiments, fly serum was found to induce calcium flashes in wing discs specifically on the release of mechanical compression, indicating that tension is a requirement for calcium signaling in these wing discs [149]. It is interesting to consider the TrpM results in light of these mechanical studies, as some TrpM channels can be mechanosensitive. Together, these data suggest that there may be a role for mechanical tension in wound-induced calcium responses.

Functions of the Gbp/Mthl10 induced calcium increase around wounds

We have found two independent mechanisms that increase cytoplasmic calcium, and in the cells at the wound margin these mechanisms would appear to act redundantly. Such redundancy indicates that the role of calcium in these cells is very important for wound healing. One biological pathway that may be downstream of calcium in these cells is recruitment of actin and myosin to the wound margin [6,72,169] to form an actomyosin purse-string that cinches the wound closed [6,68,169]. What about calcium in the distal cells, regulated by Gbp/Mthl10? There are many possible functions, but at the moment, all of them are speculative. One possibility is that the cytosolic calcium response initiates distal epithelial cells to modify their cellular behavior from a stationary/non-proliferative state to a migratory and/or proliferative state necessary to repair the wound. Alternatively, an increase in cytosolic calcium may act to modulate an inflammatory response through DUOX leading to the formation of hydrogen peroxide to recruit inflammatory cells to the wound [7] or through the calcium-dependent activation of cytoplasmic

Phospholipase A_2 leading to the rapid recruitment of immune cells to tissue damage [8]. This possibility is intriguing because Gbp is known to activate an immune response leading to the upregulation of antimicrobial peptides [155] and to increased activity of phagocytic plasmatocytes in a calcium-dependent manner [170]. Interestingly, loss of Methuselah-like (Mthl) GPCRs results in increased lifespans [154,171,172], and Gbps are nutrition-sensitive peptides whose expression is reduced under starvation conditions [160]. Increased lifespan, caloric restriction and decreased inflammation have all been linked [173–176], and Gbp/Mthl10 activation at wounds may be part of this link.

Although the cytokine and GPCR families are widely conserved, Gbp and Mthl10 do not have direct orthologs in chordates. Nonetheless, similarities exist between the Gbp/Mthl10 mechanism and wound responses in other organisms. Damage- or pathogen-induced activation of proteins by proteolytic cleavage has been well documented in the cases of spätzle in the Toll pathway [99–101], thrombin and fibrin in the blood coagulation pathway [106–108], and IL-1β and IL-18 in the pyroptosis pathway [177–179]. Additionally, wound-defense signaling in plants relies on an immunomodulatory plant elicitor peptide that is cleaved into its active form by cysteine proteases upon damage-induced cytosolic calcium [144], and the plant defense hormone systemin is cleaved into its active form by phytaspases in response to damage or predation [180]. Because the basic circuitry is similar across kingdoms, our study suggests an ancient strategy for wound detection based on proprotein cleavage, activated by proteases released via cell lysis. As these examples make clear, proteases are already known to play critical roles in blood clotting and immune signaling, and this study finds that proteases are also instructive signals in epithelial wound detection.

Limitations of the Study

As noted above, the Gbp ligands and Mthl10 receptor are not present in mammals, so the extent of mechanistic conservation is unclear. Further, we have not experimentally tested

this wound-detection mechanism in other developmental stages of *Drosophila*. For the computational model, several simplifications were made: the use of one variable for all proteases and one variable for all Gbps, rather than having separate Gbp1 and Gbp2; the use of simplified receptor/ligand dynamics that do not include uptake or recycling; and the use of a ligand-receptor binding threshold rather than inclusion of the signal transduction cascade between receptor-binding and calcium release. Finally, this study does not describe or address the mechanism behind the calcium flares that continue for at least an hour after wounding.

Acknowledgements

We thank E. Baehrecke (University of Massachusetts Medical School, Worcester, MA) for providing the *UAS-IP$_3$* sponge fly stock; T. Koyama (IGC, Lisbon, Portugal) for providing the Δ*Gbp1,2* fly stock; the Bloomington *Drosophila* Stock Center (Bloomington, IN) and the National Institute of Genetics (Shizuoka, Japan) for *Drosophila* stocks; G. Struhl (Columbia University, New York, NY) for providing the plasmid containing the *Actin5c* promoter; G. Neuert, M. Tyska, J. Nordman, and I. Macara (Vanderbilt University, Nashville TN) for comments on the manuscript. Funding: This work was supported by the National Institute of General Medical Sciences (1R01GM130130 to A.P.M. and M.S.H.), the National Institute of Arthritis and Musculoskeletal and Skin Diseases (R21AR072510 to A.P.M.). E.K.S. was supported by the National Institute of Cancer (5T32CA119925) and J.O.C. was supported by the National Institute of Child Health and Human Development (T32HD007502) and the American Heart Association (19PRE34410069 to J.O.C.).

Author Contributions

J.O.C., E.K.S., A.C.S., M.S.H., and A.P.M designed this study and developed the methodology for experiments. K.S.L. and N.N. created the *Gbp1*$^{\Delta}$ and *Gbp2*$^{3\Delta FS}$ mutant fly lines. J.O.C., E.K.S., and C.D.G. performed pupal wounding experiments and analyzed that data. J.O.C. and F.B.A. performed larval wing disc experiments and analyzed that data. A.C.S. and

M.S.H. designed and created the computational model. J.O.C. and A.C.S. created the figures. J.O.C., A.C.S., M.S.H., and A.P.M. wrote and edited the manuscript.

CHAPTER 4 MAIN FIGURES

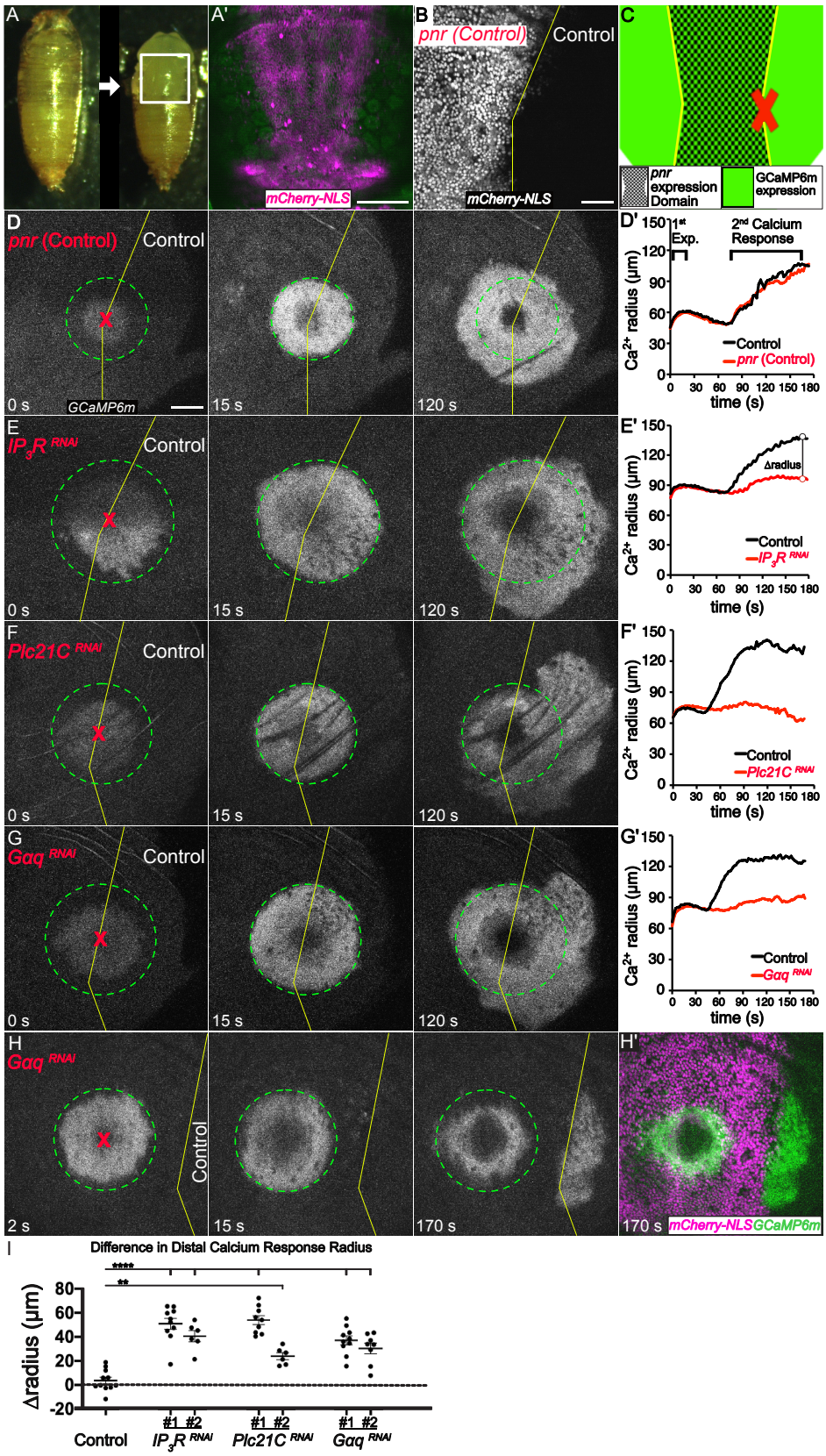

Chapter 4, Figure 1. Wounds trigger calcium release via the G_q pathway.
(A) Experimental model, *Drosophila* pupa (left) with pupal case removed (right). Gene expression is controlled in the *pnr* domain, as delineated by mCherry-NLS (magenta in **A'**, grayscale in **B**). **(B-C)** wounds (red X) are targeted at the *pnr* boundary (yellow line, **B, C**). (**D-H)** GCaMP6m calcium reporter. **(D, D')** Calcium response to wounds in the absence of gene knock-down. The max radius of the rapid first calcium expansion is marked by green circle; the distal calcium response begins ~45-75 s after wounding. Analysis of the calcium radius with respect to time **(D')** demonstrates that the response is symmetric on both sides of the *pnr* boundary. n = 11. (**E–G**) The distal calcium response requires G_q-pathway components knocked down on the left side (*pnr* domain) of each panel. *IP3R RNAi #1* n = 10, *IP3R RNAi #2* n = 6, *PLC21C RNAi #1* n = 9, *PLC21C RNAi #1* n = 6, *Gαq RNAi #1* n = 10, *Gαq RNAi #2* n = 8. (**D'–G'**) Quantification of calcium dynamics for control (black) and *pnr* (red) sides of wounds. (**H**) Wound targeted within the Gα*q* knock-down domain (left of yellow line) yields no distal calcium response until the initiating signal reaches the nearby control domain. (**H'**) Green shows calcium (*GCaMP6m*), magenta shows *pnr* domain where Gα*q* is knocked down. (**I**) Δradius, difference in calcium signal radii at maximum extent of the distal calcium response for control minus *pnr* side of each wound (as shown in E'), with *pnr*-knockdown genotypes indicated; bars = mean $\pm$ SEM. Statistical analysis by one-way ANOVA, which included all genotypes from Fig. 1, Fig. 2, and Fig. S1, multiple comparisons WRT control group, **p<0.01, ****p<0.0001. Scale bars = 200 µm (A'), or 50 µm (B–H'). See also: Figure S1, Movies 1–4.

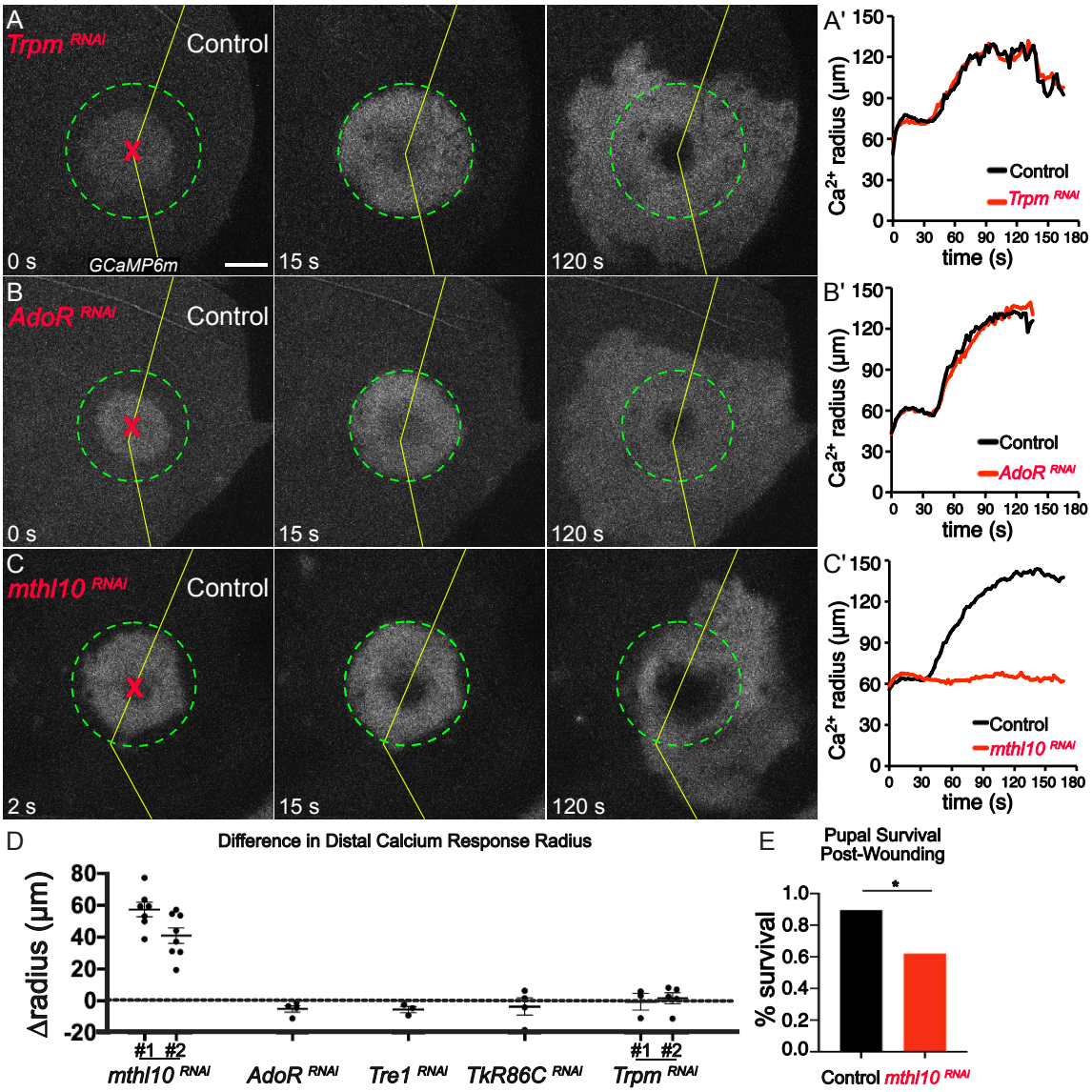

Chapter 4, Figure 2: The distal calcium response requires the GPCR Methuselah-like 10 (Mthl10).

(**A–C**) GCaMP6m reporter showing cytosolic calcium in representative samples. RNAi of the indicated gene is limited to the *pnr* domain (left side), and wounds (red X) are administered at the *pnr* domain boundary (yellow line). Maximum extent of first expansion is marked by dashed green circle. (**A**) Knockdown of the calcium ion channel *TRPM* has no effect on either calcium response. *TRPM RNAi #1* n = 3, *TRPM RNAi #2* n = 5 (**B**) Knockdown of the GPCR Adenosine Receptor (*AdoR*) has no effect on either calcium response. *AdoR RNAi* n = 4. (**C**) Knockdown of the GPCR *Methuselah-like 10* (*Mthl10*) phenocopies the G_q-pathway knockdowns, with a dramatic decrease in the distal calcium response. *mthl10 RNAi #1* n = 7, *mthl10 RNAi #2* n = 8. (**A'–C'**) Quantification of calcium signal radius versus time in control (black) and *pnr*-expression (red) sides of each wound. (**D**) Δradius between control and *pnr* sides, with *pnr*-knockdown genotypes indicated; bars = mean ± SEM. *Tre1 RNAi* n = 3, *TkR86C RNAi* n = 4. Both mthl10 RNAi lines were statistically significant (****p<0.0001) by one-way ANOVA, which included all genotypes from Fig. 1, Fig. 2, and Fig. S1, multiple comparisons WRT control group from Fig. 1. (**E**) Pupal survival to adulthood after large wounds. Quantification by Chi-Square, n=29 each, p=0.0141. Scale bar = 50 µm. See also: Movie 5.

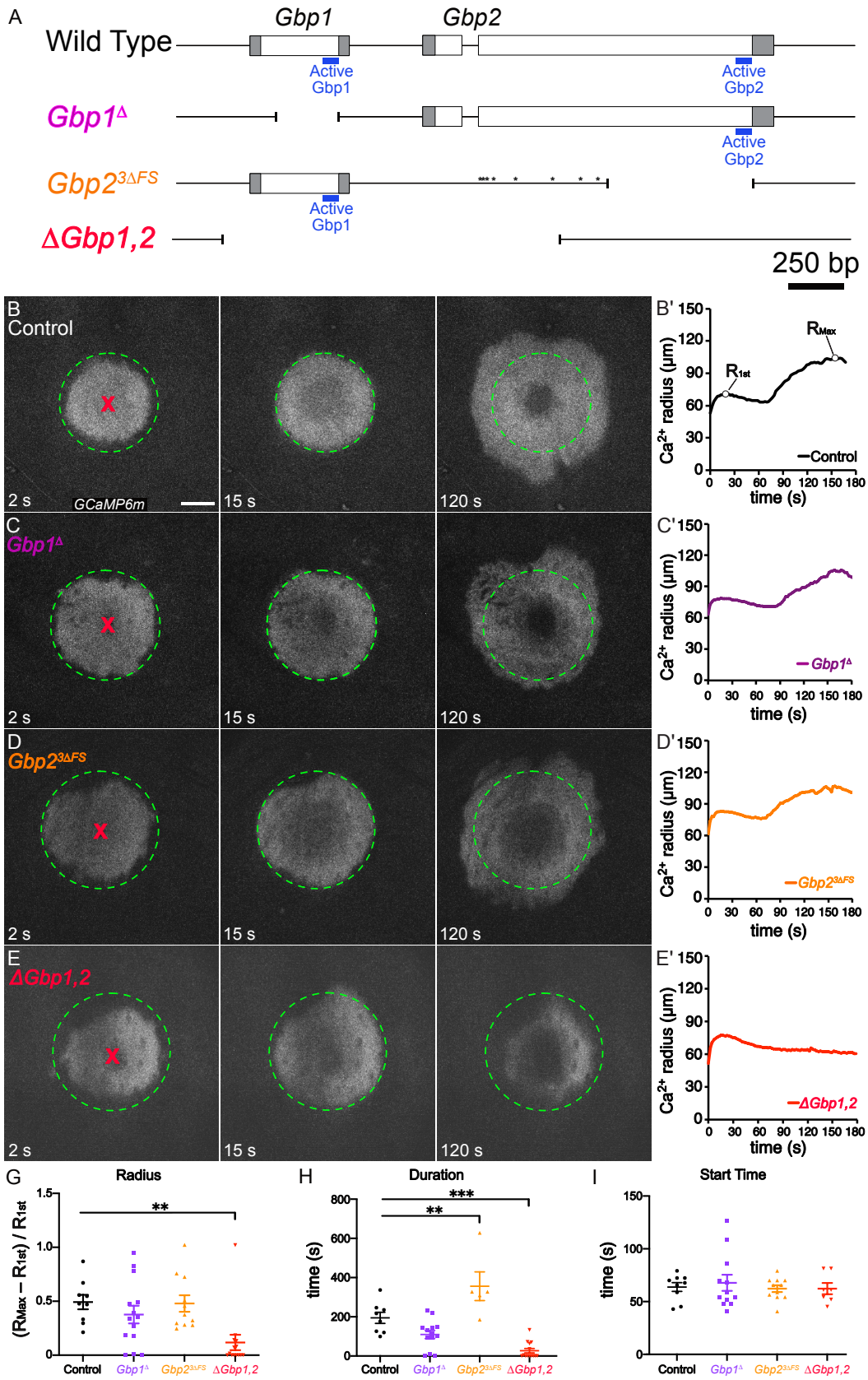

Chapter 4, Figure 3: The distal calcium response requires either Gbp1 or Gbp2.

(**A**) Schematic showing the genomic region for *Gbp1* and *Gbp2*, the deletion Δ*Gbp1,2*, and the *Gbp1* or *Gbp2* null mutants generated for this study (transcription proceeds from left to right). The $Gbp1^{\Delta}$ deletion allele is missing 282 bases within the coding region of *Gbp1*, removing most of the region encoding the Gbp1 active peptide (blue). The complex $Gbp2^{3\Delta FS}$ allele comprises 8 point mutations (asterisks) and 3 deletions, inducing frameshifts and premature terminations upstream of the Gbp2 active peptide (blue) (see Methods). (**B–E**) GCaMP6m reporter showing cytosolic calcium in representative samples of control or deletion mutants. Scale bar = 50 µm. (**B, B'**) The normal calcium response is present in controls (n = 9). (**C-D**) Homozygous $Gbp1^{\Delta}$ (**C**) or $Gbp2^{3\Delta FS}$ (**D**) each retain the distal calcium response (n = 14 and 11 respectively). (**E,E'**) A normal distal calcium response is absent after wounding homozygous Δ*Gbp1,2* in n=13/14. (**G**) Spatial quantification of each sample's maximum radius (R_{Max} in **B'**) normalized to its first expansion maximum radius (R_{1st} in **B'**). Δ*Gbp1,2* has a significantly decreased response compared to control, while the $Gbp1^{\Delta}$ and $Gbp2^{3\Delta FS}$ do not. **(H)** Duration that distal calcium response radius exceeded R_{1st}. Δ*Gbp1,2* has a significantly decreased duration compared to control, while surprisingly, $Gbp2^{3\Delta FS}$ was significantly increased. Movies cut off before the distal calcium response dipped below R_{1st} were excluded from **H**. (**I**) The start time, defined as the time when the calcium radius began consistently increasing for the distal calcium response, shows no significant differences. Samples where $R_{Max} = R_{1st}$ were excluded from **I**. Statistical analysis by one-way ANOVA, multiple comparisons WRT control group, **p<0.01, ***p<0.001.

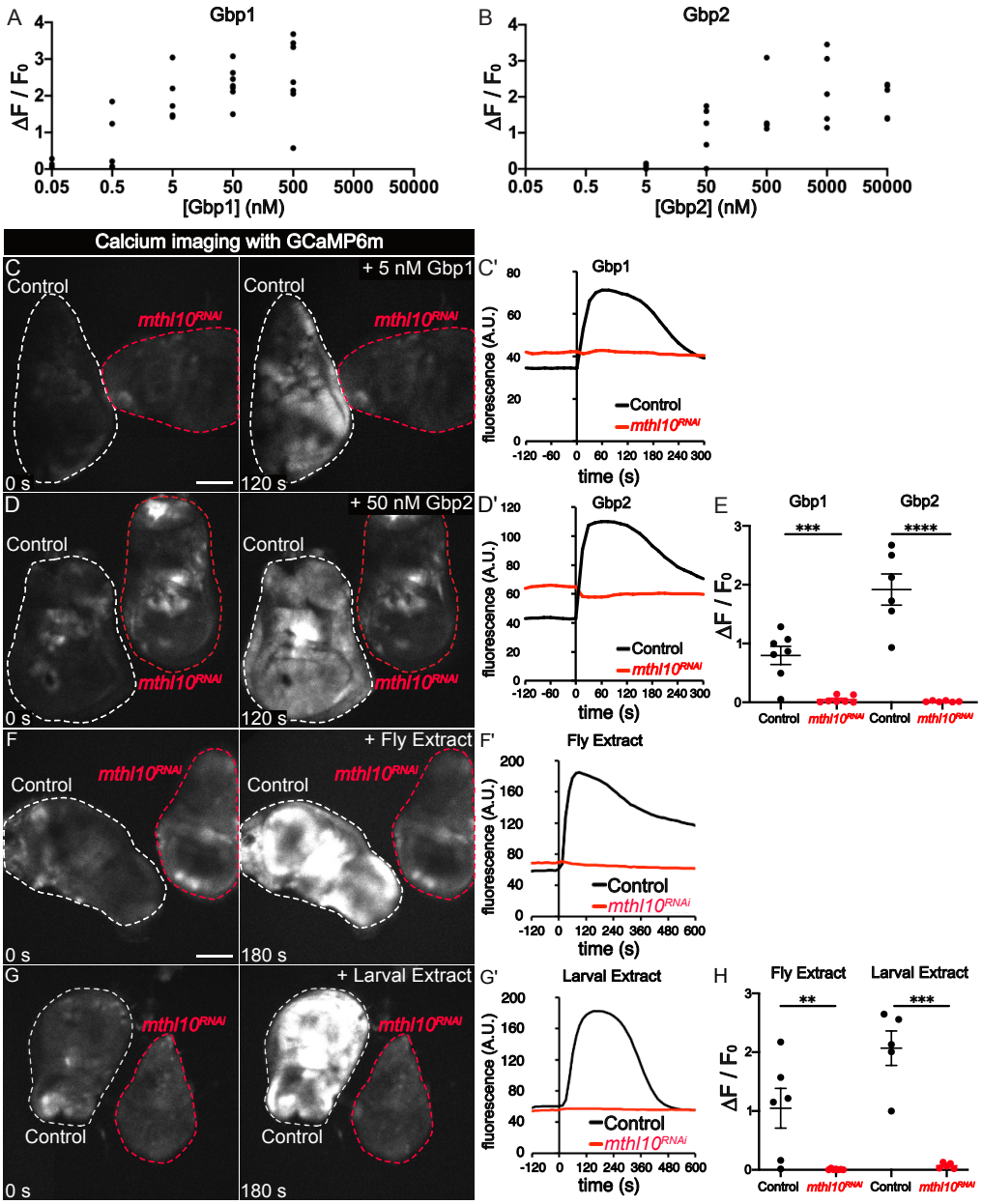

Chapter 4, Figure 4: Gbp peptides and *Drosophila* extracts elicit calcium responses in wing discs through Mthl10.

(**A-B**) Gbp1 or Gbp2 peptides elicit a concentration-dependent calcium response in wing discs. Gbp1 additions n = 29, Gbp2 additions n = 21. 5 nM Gbp1 or 50 nM Gbp2 consistently elicits a calcium response. (**C-D, F-G**) Assays were performed with two wing discs (one control and one *mthl10* knockdown) mounted adjacently and activated simultaneously. *Mthl10* is required in wing discs for Gbp1 (**C**, n = 7) or Gbp2 (**D**, n = 6) to activate a calcium response. Change in GCaMP6m fluorescence over time for samples **C** and **D** is quantified in **C'** and **D'**, respectively. (**E**) Normalized change in fluorescence is quantified for all samples. (**F-G**) *Mthl10* is required in wing discs for 5% fly extract (**F**, n = 6) or 5% larval extract (**G**, n = 5) to activate a calcium response. Change in GCaMP6m fluorescence over time for samples **F** and **G** is quantified in **F'** and **G'**, respectively. (**H**) Normalized change in fluorescence is quantified for all samples in **F'** and **G'**. Scale bar = 100 µm. Graph bars represent mean and SEM. **p<0.01, ***p<0.001, ****p<0.0001 by Student's t-test. See also: Figure S2, Movie 6–7.

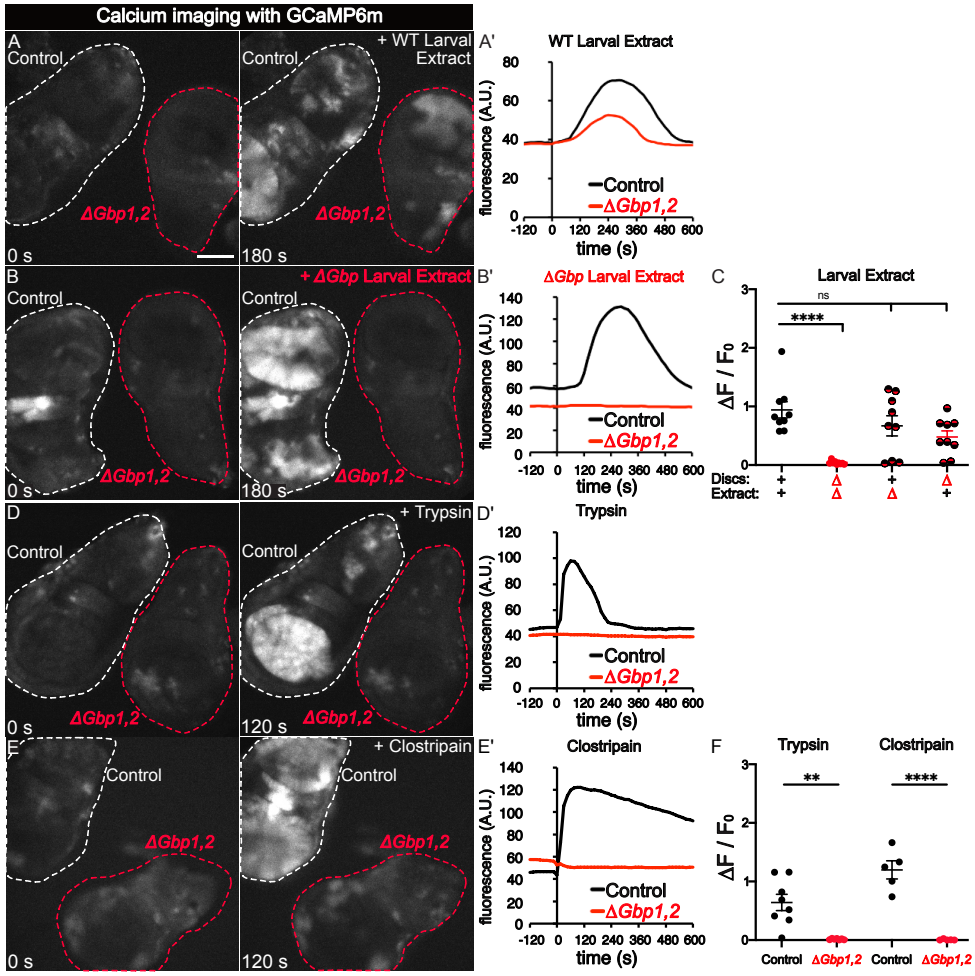

Chapter 4, Figure 5: *Drosophila* extract and proteases require Gbps to elicit calcium responses.

(**A-F**) All assays were performed with two wing discs (one control and one Δ*Gbp1,2*) mounted adjacently and activated simultaneously. Scale bar = 100 µm. (**A-C**) Gbp is required for the larval extract-mediated calcium response, as no response occurs if Gbp is absent from both extract and wing disc (**A, A'**, n = 9). The signal can be supplied by either the wing disc (**A, A'**) or by the larval extract (**B, B'**, n = 9). Normalized change in fluorescence is quantified in **C**. **(D-F)** Serine protease trypsin (**D**, n = 8) or cysteine protease clostripain (**E**, n = 5) activate calcium in a Gbp-dependent manner. Normalized change in fluorescence is quantified in **F**. Graph bars represent mean and SEM. **p<0.01, ****p<0.0001 by two-way ANOVA in **C** and Student's t-test in **F**. See also: Movie 8.

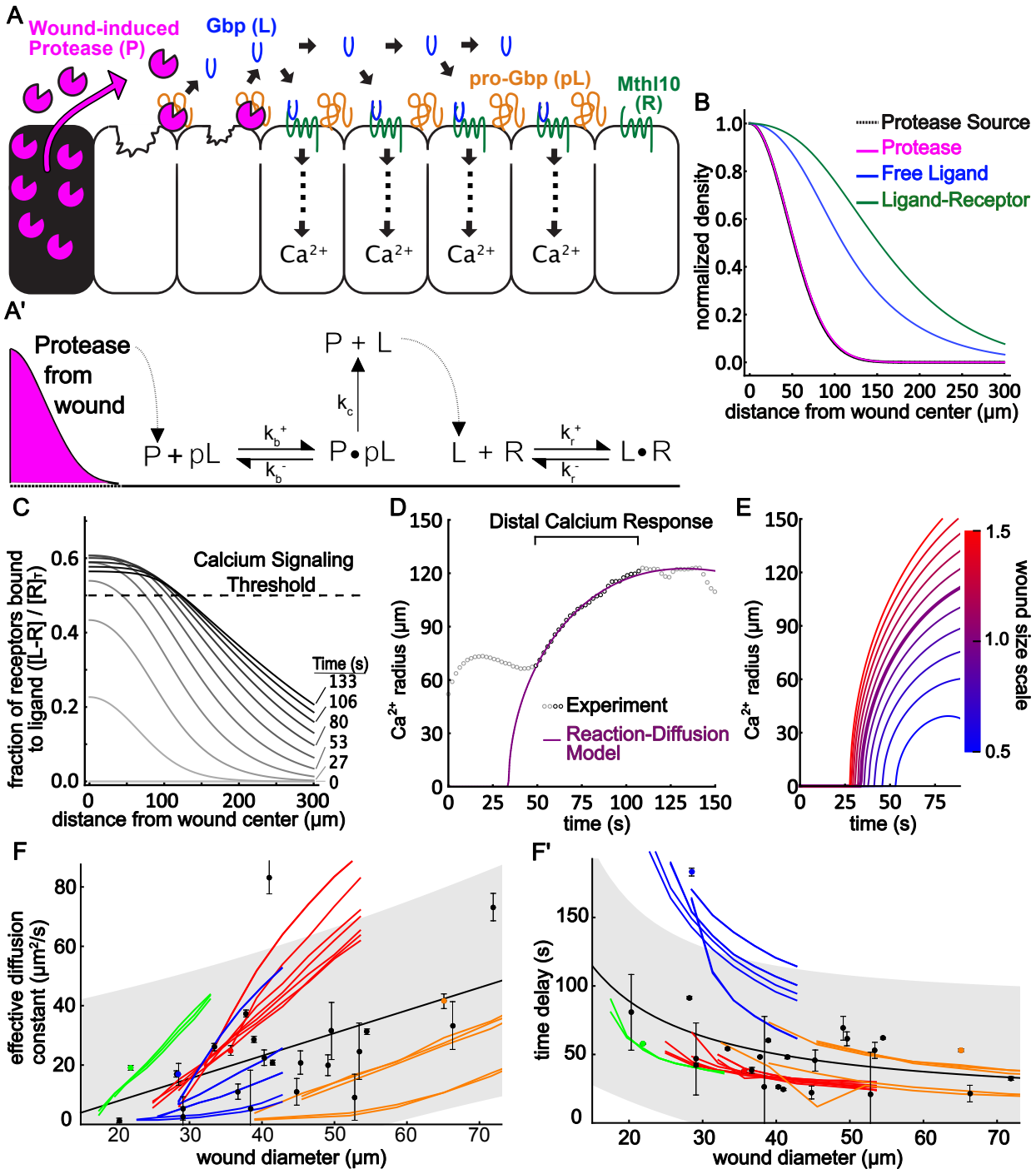

Chapter 4, Figure 6: Reaction-diffusion (RD) model for epithelial wound detection. (**A, A'**) Model schematic and reactions. Diffusible proteases (P) released from lysed and damaged cells cleave immobile pro-ligand (pL), releasing diffusible, activated ligand (L) that binds to its cognate cell-surface receptor (R). **(B)** RD model output of concentration of protease (pink line), free ligand (blue line), and ligand-receptor complex (green line) as a function of distance from the wound center 1 minute after wounding. Each line is normalized by the component's maximum concentration over all space 1 minute after wounding. The spatial extent of the protease source (black dashed line) is normalized so that its maximum is 1. (**C**) Representative model output for the fraction of receptors bound to ligand as a function of

distance from the wound at various times. Threshold for triggering calcium response is taken as 0.5 (dashed line). (**D**) Calcium signal radius versus time after wounding: experimental data (open circles), and RD model fit (purple line). (**E**) Calcium signal radius from the RD model for different simulated wound sizes; each line represents the impact of scaling the wound size for an otherwise fixed set of RD parameters determined from the best fit to an individual wound response. The bold line corresponds to a scale of 1.0 and matches the best fit line in panel D. **(F-F')** Experimental and modeled wound size dependence of the effective diffusion (F) and start time (F') of the distal calcium response. Experimental data (black dots) are taken from n = 26 wounds larger than 15 μm in diameter. Black line and shaded region indicate the best fit curve and single prediction 95% confidence interval respectively for a linear fit (F) and hyperbolic fit (F') to the data. Model results (colored lines) are determined by scaling the wound size from a best fit parameter set and then parameterizing the model outputs according to a delayed-diffusion model. Each color represents a fit to the same dataset (as in Fig. S3, S4), and each line corresponds to a different best fit parameter set. See also: Figures S3–5, Movie 9.

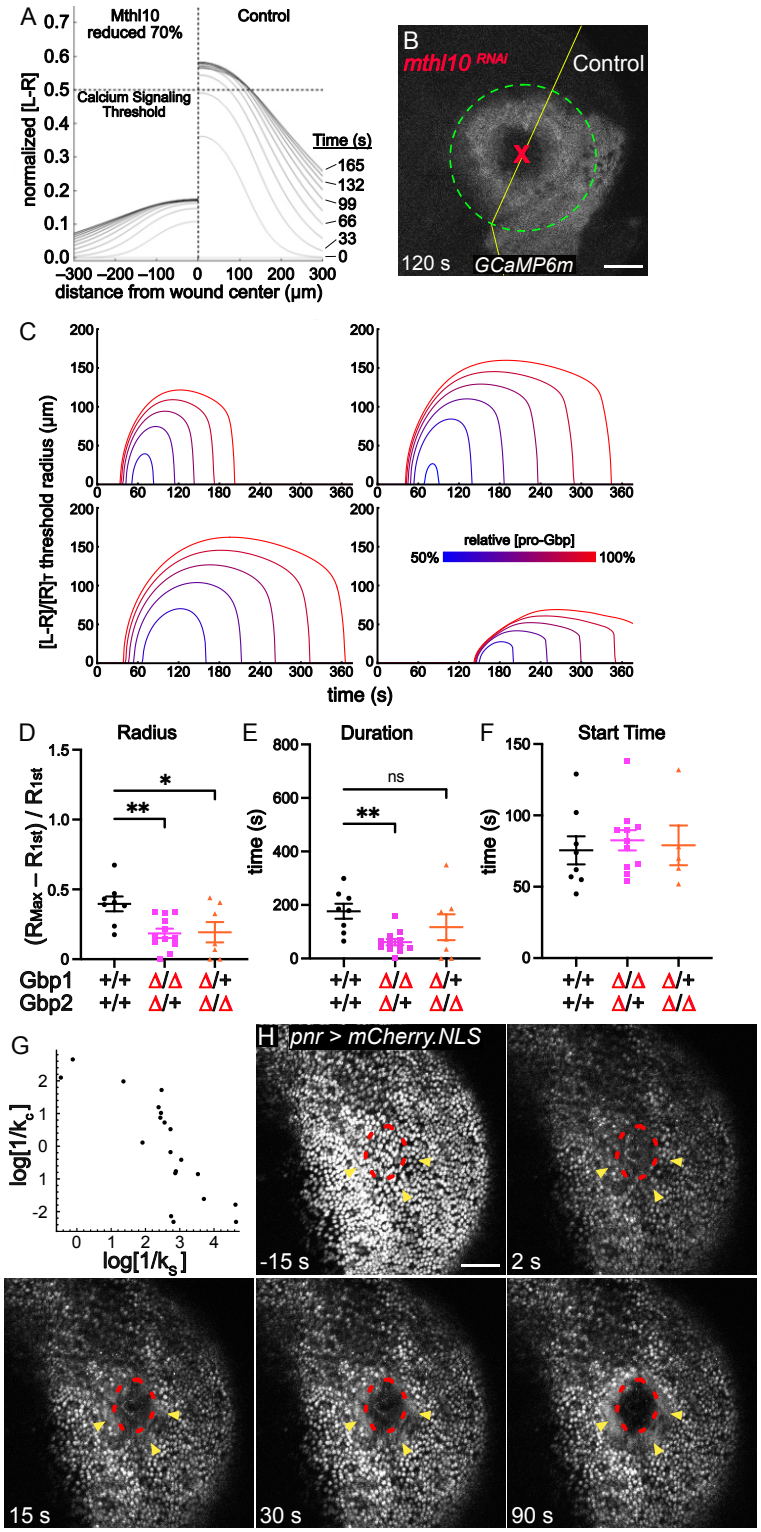

Chapter 4, Figure 7: Reaction-diffusion (RD) model predictions and experimental validations.

(**A**) Representative RD model output for the normalized fraction of receptors bound to ligand as a function of distance from the wound at various times, with Mthl10 reduced on one side of the wound. The threshold for triggering calcium response is taken as 0.5 (dashed line). Negative

distances (left side) correspond to the side with a reduced receptor level, and positive distances (right side) show the response on the control side with an unaltered receptor level. The signal does not reach the threshold on the side where Mlth10 is reduced, matching *in vivo* experimental data where *mthl10* is knocked down on one side (**B**). Scale bar = 50 μm. (**C**) Model output for four parameter sets with varying initial concentration of extracellular pro-Gbp, showing sufficiently decreased levels of pro-Gbp are predicted to decrease the radius and duration of the calcium response, a result not observed in Fig. 3. (**D–F**) Post-hoc experiments performed on trans-heterozygous pupae expressing one allele of either *Gbp1* or *Gbp2* while null for the other. The distal calcium response radius is significantly decreased in both conditions (**D**), while the signal duration is decreased in the condition lacking both copies of *Gbp1* (**E**). Interestingly, the start times (**F**) were unchanged, as predicted in **C**. Statistical analysis by one-way ANOVA, multiple comparisons WRT control group, *$p<0.05$, **$p<0.01$. (**G**) Time constant of pro-ligand cleavage ($1/k_c$) is inversely correlated with the time constant of protease release and activation ($1/k_S$). The model predicts that a rapid pro-ligand cleavage will only occur if the protease is released and activated slowly over time, or in rare cases a rapid protease release can occur but only if the pro-ligand cleavage occurs slowly. In both cases, the triggering signal must build up slowly, indicating that cells lyse and protease accumulates progressively over time after wounding, rather than all at once. **(H)** The black region devoid of mCherry.NLS signal corresponds to the region of fully lysed cells. Cells lyse progressively over time during the first 90 s following wounding, expanding to a region indicated by the red dotted circle. Yellow arrowheads indicate cells with damaged nuclear membranes, which release nuclear-localized mCherry from nuclei into the cytosol, a process which also appears to occur progressively. Scale bar = 50 μm.

Supplemental Movies can be found in the supplemental material to O'Connor, et al. *Dev Cell* 2021.[113]

Chapter 4, Movie S1: Calcium signaling is observed in response to wounds in *Drosophila* pupae.

Chapter 4, Movie S2: The distal calcium response requires components of the Gq-signaling pathway.

Chapter 4, Movie S3: Puncture wounds recapitulate laser wounds in *Drosophila* pupae.

Chapter 4, Movie S4: The distal calcium response can jump from the Gq knockdown domain to the control domain.

Chapter 4, Movie S5: The distal calcium response requires the GPCR Methuselah-like 10.

Chapter 4, Movie S6: Gbp1 and Gbp2 elicit a calcium response in wing discs in an Mthl10-dependent manner.

Chapter 4, Movie S7: *Drosophila* extract elicits a calcium response in wing discs in an Mthl10-dependent manner.

Chapter 4, Movie S8: Larval extract elicits a calcium response in wing discs in a Gbp-dependent manner.

Chapter 4, Movie S9: Model output of scaled molecular component concentrations and calcium signal radius vs. time

SUPPORTING TEXT

Reaction-Diffusion Model of the Distal Calcium Response

The extracellular space

While the extracellular space in the pupal laser wound experiments is a three-dimensional space, arguments can be made to reduce it to a one-dimensional space. First, a cuticle that exists just above the tissue essentially limits the extracellular space to a two-dimensional plane. Second, due to the radial symmetry of the distal calcium response around the wound, we can assume that the system is radially symmetric about the wound center. Therefore, the relevant molecular components in the model can be assumed to only depend on two dependent variables: one spatial variable r that is the distance from the center of the wound, and one temporal variable t that is the time since wounding.

Protease Source

Since the extent of the damage decreases farther from the wound center, it is reasonable to assume that the source of active protease follows this same trend. Therefore, the active protease source initiated by the wound is taken to be a Gaussian in space whose maximum is at the wound center. The source is also taken to decay exponentially in time to represent the depletion of protease from the total amount released from the wound. The protease source term then takes the form

$$S(r,t) = \frac{P_0 k_S}{2\pi\sigma_w^2} \exp\left(-\frac{r^2}{2\sigma_w^2} - k_S t\right) \tag{1}$$

where P_0 is the total number of protease molecules released from the source, k_S is the rate constant for the source, and σ_w determines the spatial extent of the source.

It is worth noting that, while active protease could arise from various mechanisms, the model remains agnostic as to how we get to a final, activated form of the protease. Therefore, the Gaussian form of the protease source just represents where we would expect to find active protease after various activation mechanisms have occurred.

Protease-proligand model

The protease-proligand interactions are modeled as a simple reaction, where one protease molecule reversibly binds to one proligand molecule to form a complex. This complex is then irreversibly converted into a protease molecule and a ligand molecule upon cleavage of the proligand. These processes can be modeled with the scheme shown in Fig 6A' with rate constants k_b^+ , k_b^-, and k_c.

Ligand-Receptor model

The ligand-receptor interactions are modeled as a simple reaction, where one ligand molecule reversibly binds to one receptor molecule to form a complex. This process can be modeled with the scheme shown in Fig 6A' with rate constants k_r^+ and k_r^-. While the ligand-receptor dynamics upstream of calcium signaling can be modeled in a more detailed way, as in [181], these processes most likely do not influence the calcium signals on the timescale of the distal calcium response, so they are not considered here.

Reaction-Diffusion Model Set of Equations

Using the law of mass action, the model reactions above can be turned into a set of coupled partial differential equations. The model assumes that all molecular components exist in a radially symmetric, two-dimensional plane where protease and ligand can diffuse with

diffusion constants D_P and D_L respectively. All other molecular components are assumed to be immobile. This leads to the following set of six differential equations

$$\frac{\partial[P]}{\partial t} = D_P \nabla^2[P] + S - k_b^+[P][pL] + k_b^-[P \cdot pL] + k_c[P \cdot pL] \tag{2}$$

$$\frac{\partial[pL]}{\partial t} = -k_b^+[P][pL] + k_b^-[P \cdot pL] \tag{3}$$

$$\frac{\partial[P \cdot pL]}{\partial t} = k_b^+[P][pL] - k_b^-[P \cdot pL] - k_c[P \cdot pL] \tag{4}$$

$$\frac{\partial[L]}{\partial t} = D_L \nabla^2[L] + k_c[P \cdot pL] - k_r^+[L][R] + k_r^-[L \cdot R] \tag{5}$$

$$\frac{\partial[R]}{\partial t} = -k_r^+[L][R] + k_r^-[L \cdot R] \tag{6}$$

$$\frac{\partial[L \cdot R]}{\partial t} = k_r^+[L][R] - k_r^-[L \cdot R] \tag{7}$$

where brackets denote the concentration of a molecular component in terms of number of molecules per unit area, and the Laplacian operator ∇^2 is expressed in terms of the polar coordinate r as $\nabla^2 = \frac{\partial^2}{\partial r^2} + \frac{1}{r} \cdot \frac{\partial}{\partial r}$.

In order to simplify this set of equations, it is assumed that ligand production is described by Michaelis-Menten kinetics and that ligand-receptor binding is at equilibrium on fast timescales. Therefore, we have

$$[P][pL] = K_b[P \cdot pL] \tag{8}$$

$$[L][R] = K_r[L \cdot R] \tag{9}$$

where $K_b = \frac{k_b^- + k_c}{k_b^+}$ and $K_r = \frac{k_r^-}{k_r^+}$. Additionally, by defining the total proligand concentration as $[pL]_T = [pL] + [P \cdot pL]$ and the constant total receptor concentration as $[R]_T = [R] + [L \cdot R]$, we obtain the following equations:

$$[P \cdot pL] = \frac{[P][pL]_T}{K_b + [P]} \tag{10}$$

$$[L \cdot R] = \frac{[L][R]_T}{K_r + [L]} \tag{11}$$

By adding together specific pairs of equations from (2) – (7) we obtain

$$\frac{\partial}{\partial t}([pL] + [P \cdot pL]) = \frac{\partial [pL]_T}{\partial t} = -k_c[P \cdot pL] \tag{12}$$

$$\frac{\partial}{\partial t}([R] + [L \cdot R]) = \frac{\partial [R]_T}{\partial t} = 0 \tag{13}$$

$$\frac{\partial}{\partial t}([P] + [P \cdot pL]) = D_P \nabla^2 [P] + S \tag{14}$$

$$\frac{\partial}{\partial t}([L] + [L \cdot R]) = D_L \nabla^2 [L] + k_c [P \cdot pL] \tag{15}$$

Then, by combining equations (10) – (15) we end up with a set of three differential equations and four algebraic equations

$$\frac{\partial [P]}{\partial t} = \left(1 + \frac{K_b [pL]_T}{(K_b + [P])^2}\right)^{-1} \cdot \left[D_P \nabla^2 [P] + S + k_c \left(\frac{[P]}{K_b + [P]}\right)^2 [pL]_T\right] \tag{16}$$

$$\frac{\partial [pL]_T}{\partial t} = -k_c \cdot \frac{[P] \cdot [pL]_T}{K_b + [P]} \tag{17}$$

$$\frac{\partial [L]}{\partial t} = \left(1 + \frac{K_r [R]_T}{(K_r + [L])^2}\right)^{-1} \cdot \left[D_L \nabla^2 [L] + k_c \cdot \frac{[P] \cdot [pL]_T}{K_b + [P]}\right] \tag{18}$$

$$[P \cdot pL] = \frac{[P] \cdot [pL]_T}{K_b + [P]} \tag{19}$$

$$[pL] = [pL]_T - [P \cdot pL] \tag{20}$$

$$[L \cdot R] = \frac{[R]_T [L]}{K_r + [L]} \tag{21}$$

$$[R] = [R]_T - [L \cdot R] \tag{22}$$

Initial and Boundary Conditions

Due to diffusive terms in the equations, the mobile molecular components require both boundary conditions and initial conditions, whereas the immobile molecular components only

require initial conditions. We assume that there is initially no protease or ligand in the extracellular space, and that a uniform proligand concentration $[pL]_0$ is present in the extracellular space. This gives the following initial conditions

$$[P](r,0) = 0 \tag{23}$$

$$[pL]_T(r,0) = [pL]_0 \tag{24}$$

$$[L](r,0) = 0 \tag{25}$$

The initial conditions of the other molecular components can be obtained from the algebraic equations above, although these are not important in solving the differential equations.

For each mobile molecular component, the same boundary conditions are applied: far from the wound the concentrations should go to 0, and in order to impose radial symmetry there needs to be no flux at the origin. This leads to the following boundary conditions

$$\lim_{r\to\infty}[P] = \lim_{r\to\infty}[L] = 0 \tag{26}$$

$$-D_P \frac{\partial[P]}{\partial r}\Big|_{r=0} = -D_L \frac{\partial[L]}{\partial r}\Big|_{r=0} = 0 \tag{27}$$

Non-dimensionalization

To reduce the number of parameters in the model, as well as simplify the model further, the independent variables are scaled in the following way:

$$r = r_d \rho \tag{28}$$

$$t = t_0 \tau \tag{29}$$

where $r_d = 10\ \mu m$ is the average ablation radius following wounding, $t_0 = 47\ s$ is the median time after wounding before the distal calcium response occurs, and ρ and τ are dimensionless variables for space and time, respectively. Additionally, the dependent variables are scaled in the following way:

$$[P] = [P]_0 x \tag{30}$$

$$[pL] = [pL]_0 y \tag{31}$$

$$[P \cdot pL] = [pL]_0 y_x \tag{32}$$

$$[pL]_T = [pL]_0 y_T \tag{33}$$

$$[L] = [pL]_0 \ell \tag{34}$$

$$[R] = [R]_T w \tag{35}$$

$$[L \cdot R] = [R]_T w_\ell \tag{36}$$

where $[P]_0 = \frac{P_0}{2\pi r_d^2}$, and $x, y, y_x, y_T, \ell, w,$ and w_ℓ are dimensionless variables.

By applying these scales (28) – (36)to the model equations (16) – (22) one arrives at the following non-dimensionalized equations

$$\frac{\partial x}{\partial \tau} = \left(1 + \frac{\gamma_{pL} y_T}{(1+\gamma_P x)^2}\right)^{-1} \cdot \left[\gamma_{D_P} \nabla_\rho^2 x + \frac{\gamma_S}{\gamma_w^2} \exp\left(-\frac{\rho^2}{2\gamma_w^2} - \gamma_d \tau\right) + \gamma_c \cdot \frac{\gamma_{pL}}{\gamma_P} \cdot \left(\frac{\gamma_P x}{1+\gamma_P x}\right)^2 \cdot y_T\right] \tag{37}$$

$$\frac{\partial y_T}{\partial \tau} = -\frac{\gamma_c \gamma_P x}{1+\gamma_P x} \cdot y_T \tag{38}$$

$$\frac{\partial \ell}{\partial \tau} = \left(1 + \frac{\gamma_R}{(1+\gamma_L \ell)^2}\right)^{-1} \cdot \left[\gamma_{D_L} \nabla_\rho^2 \ell + \frac{\gamma_c \gamma_P x}{1+\gamma_P x} \cdot y_T\right] \tag{39}$$

$$y_x = \frac{\gamma_P x y_T}{1+\gamma_P x} \tag{40}$$

$$y = y_T - y_x \tag{41}$$

$$w_\ell = \frac{\gamma_L \ell}{1+\gamma_L \ell} \tag{42}$$

$$w = 1 - w_\ell \tag{43}$$

where we now have nine dimensionless parameters (see also Fig. S5, which highlights the influence of each of these parameters on model output)

$$\gamma_w = \frac{\sigma_w}{r_d} \tag{44}$$

$$\gamma_{D_P} = \frac{t_0}{r_d^2} D_P \tag{45}$$

$$\gamma_{D_L} = \frac{t_0}{r_d^2} D_L \tag{46}$$

$$\gamma_S = t_0 k_S \tag{47}$$

$$\gamma_c = t_0 k_c \tag{48}$$

$$\gamma_P = \frac{[P]_0}{K_b} \tag{49}$$

$$\gamma_{pL} = \frac{[pL]_0}{K_b} \tag{50}$$

$$\gamma_L = \frac{[pL]_0}{K_r} \tag{51}$$

$$\gamma_R = \frac{[R]_T}{K_r} \tag{52}$$

Additionally, the scaled initial and boundary conditions are

$$x(\rho, 0) = 0 \tag{53}$$

$$y_T(\rho, 0) = 1 \tag{54}$$

$$\ell(r, 0) = 0 \tag{55}$$

$$\lim_{\rho \to \infty} x = \lim_{\rho \to \infty} \ell = 0 \tag{56}$$

$$-\gamma_{D_P} \frac{\partial x}{\partial \rho}|_{\rho=0} = -\gamma_{D_L} \frac{\partial \ell}{\partial \rho}|_{\rho=0} = 0 \tag{57}$$

where, once again, initial conditions for the other scaled molecular components can be determined from the algebraic relations, although these are not important for solving the differential equations.

Method of Solution

Due to the $1/\rho$ dependence of the Laplacian operator in polar coordinates, the boundary condition at $\rho = 0$ cannot be handled numerically in a simple fashion. Therefore, the boundary conditions were imposed at a small radial distance of $\Delta\rho = .001$, and the protease source was shifted this distance as well so that the scaled source term becomes $s(\rho, \tau) = \frac{\gamma_S}{\gamma_w^2} \exp\left(-\frac{(\rho-\Delta\rho)^2}{2\gamma_w^2} - \gamma_d \tau\right)$. Additionally, the boundary condition at infinity must be imposed at a finite value ρ_{far}. A value of $\rho_{far} = 100$ ($r_{far} = 1000\ \mu m$) was chosen for simulations since values of ρ_{far} larger than this do not cause large changes in the model output on the timescale of interest.

The software Mathematica was used to solve the above set of model equations. Since the system of equations is nonlinear and the equation for y_T does not contain derivatives with respect to ρ, the method of lines was chosen to solve the set of differential equations. Because the spatial region is one-dimensional, the "Tensor Product Grid" method was used to discretize the spatial variable. The number of grid points for this discretization was chosen to be the smallest value so that use of a larger number of points did not yield a significantly different solution. To aid in any reproduction, the numerical differential equation solver function 'NDSolveValue' was used with settings specified by

```
Method->{"IndexReduction"->Automatic,
        "EquationSimplification"->"Residual",
        "PDEDiscretization"->{"MethodOfLines",
                              "SpatialDiscretization"->{"TensorProductGrid",
                                                        "MinPoints"->200,
                                                        "MaxPoints"->500,
                                                        "DifferenceOrder"->2
                                                        }
                              }
         }
```

A more detailed description of the numeric solution algorithms and settings can be found in the Mathematica documentation.

Model Output and Signal Radius

Solving the set of non-dimensionalized model equations along with a set of parameter values yields scaled molecular component concentrations as functions of $\rho = r/r_d$ and $\tau = t/t_0$.

The model assumes that for a given spatial coordinate ρ, calcium will first be released into the cytosol when at least half of the receptors are bound to a ligand molecule. This sets a threshold for the scaled variable w_ℓ as $w_{thresh} = 0.5$. By solving for the radial distance ρ_{thresh} such that $w_\ell(\rho_{thresh}, \tau) = w_{thresh}$, we can then determine the signal radius as a function of time $\rho_{thresh}(\tau)$. Therefore, it is assumed that $\rho_{thresh}(\tau)$ is equal to the calcium radius during the distal calcium response.

After the distal calcium response, the calcium dynamics are determined by processes not covered in the current model. Therefore, it should be noted that the proposed model is not valid past the distal calcium response, as the ligand is not the sole factor in determining the calcium dynamics past this point.

Estimate of Gbp diffusion constant

To estimate the free diffusion constant of the ligand Gbp, we assume that the ligand of molecular weight as 2.79 kDa ≈ 4.63 x 10^{-21} g (based on the peptide sequence described above) is spherical with a typical protein density of 1.37 g/cm^3. This results in an estimated effective radius of 0.93 nm. Using the Stokes-Einstein relation at a temperature of 293 K in water results in an estimated diffusion constant of about 260 μm^2/s, which is 122.2 in scaled units. This estimate is only used to approximate the free Gbp diffusion constant; this parameter was still allowed to vary during the fitting process.

Initial Guess Selection

Initial guesses for each selected distal calcium response was obtained by randomly searching parameter space for parameter sets that produced model outputs that met two criteria. First, the parameter set had to produce a distal calcium response that did not extend past the maximum of the distal calcium response to be fit to. Second, the parameter set had to produce a distal calcium response that had a sum of squares error that was 10% or less than

the sum of squares error of a no-response model output (where the fraction of receptors bound to ligand never crosses the 50% threshold). Sum of square errors are determined according to step 2 of "Fitting the model to the data" below. For each of the four selected data sets to fit to, 32 initial guesses were obtained.

Fitting the model to the data

The first goal of the model is to reproduce the distal calcium response data. This is done by fitting the model output of $\rho_{thresh}(\tau)$ to the data by varying the nine dimensionless parameters mentioned earlier. Due to a possibly large space of feasible parameter values, a fitting method is desired that searches a sufficient amount of the parameter space without taking too much time or biasing one region of parameter space over another. Therefore, the fitting method is based on orthogonal array sampling. The fitting steps are outlined below:

1. A distal calcium response dataset is chosen that the model will be fit to. In order to prevent $\rho_{thresh}(\tau)$ from increasing to ρ values past the distal calcium response at later times, additional "constraint points" are appended to the dataset that are equal to the maximum extent of the distal calcium response. The number of constraint points is equal to the number of experimental data points in order to equally weigh fitting the distal calcium response with not extending past its maximum extent.

2. A fitting function to be minimized is defined in two parts. For the original data points, the fitting function is just a sum of squares difference between the data and the model. For the constraint points, the fitting function is also a sum of squares difference between the model and the data, but it is 0 if $\rho_{thresh}(\tau)$ is less than the corresponding constraint point. This way there is only a penalty when the model output extends past the maximum extent of the distal calcium response. The goal of the fitting procedure is then

to find a parameter set that minimizes the fitting function. More explicitly, we want to minimize the following piecewise function for data points (original and constraint) $d(\tau_i)$ and model output points $\rho_{thresh}(\tau_i) = m(\tau_i)$

$$f(d,m) = \sum_i \begin{cases} (m(\tau_i) - d(\tau_i))^2 & \text{for original data points} \\ Max\,[m(\tau_i) - d(\tau_i), 0]^2 & \text{for constraint points} \end{cases}$$

3. In order to vary the dimensionless parameters across desired ranges, some of which span orders of magnitude, the dimensionless parameters are replaced in the following way

$\gamma_{D_P} \rightarrow 12.22 \times 10^{\Gamma_{D_P}}$

$\gamma_{D_L} \rightarrow 122.2 \times \Gamma_{D_L}$

$\gamma_S \rightarrow 10^{\Gamma_S}$

$\gamma_c \rightarrow 10^{\Gamma_c}$

$\gamma_P \rightarrow 10^{\Gamma_P}$

$\gamma_{pL} \rightarrow 10^{\Gamma_{pL}}$

$\gamma_L \rightarrow 10^{\Gamma_L}$

$\gamma_R \rightarrow 10^{\Gamma_R}$

$\gamma_w \rightarrow \Gamma_w$

Therefore, we have created a new dimensionless parameter set $\mathbf{\Gamma} = \{\Gamma_{D_P}, \Gamma_{D_L}, \Gamma_S, \Gamma_c, \Gamma_P, \Gamma_{pL}, \Gamma_L, \Gamma_R, \Gamma_w\}$ to use for the fitting method.

4. An initial set of parameter values $\mathbf{\Gamma}_0$ is determined as explained in the section "Initial Guess Selection" above.

5. An orthogonal array A is created with 729 runs, 9 factors, 3 levels, a strength of 5, and an index of 3. The levels are set to be {-1, 0, 1}. i.e. A is a 729 x 9 matrix with the three entries -1, 0, or 1 such that every 729 x 5 subarray of A contains every 5-tuple based on {-1,0,1} exactly 3 times.

6. For each row A_i of the orthogonal array A, a new parameter set $\mathbf{\Gamma}_i$ is obtained by adding A_i to the initial parameter set $\mathbf{\Gamma}_0$. Each of these parameter sets are then applied to the model, thus resulting in a set $\{\rho_i(\tau)\}$ of 729 different $\rho_{thresh}(\tau)$ functions.

7. For each $\rho_i(\tau)$, the fitting function from step 2 is evaluated. The parameter set $\mathbf{\Gamma}_i$ that results in the best fit $\rho_i(\tau)$ now becomes $\mathbf{\Gamma}_0$.

8. Steps 6 and 7 are repeated until the best fitting parameter set is $\mathbf{\Gamma}_0$

9. Steps 6 – 8 are repeated with entries $\{-1,0,1\}$ in the orthogonal array replaced with entries $\{-1/2^n, 0, 1/2^n\}$ for n values 1, 2, 3, and 4. The final set $\mathbf{\Gamma}_0$ is then determined to be the parameter set that best fits the data for the given initial parameter set.

Wound-size scaling of the model

The distal calcium response has two characteristics of interest: its time delay $t_{0,\min}$ and its effective diffusion constant α_{eff}. We previously showed that the distal calcium response can be fit to an empirical "delayed diffusion equation" where $t_{0,\min}$ and α_{eff} are independent

parameters that are chosen to fit the data [14]. As shown in Fig. 6F-F', these measures appear to have a wound size dependency.

The parameters in the model that are affected by the wound size are the total amount of protease that is released and the spatial extent of the protease source. However, it is assumed that the protease per cell (area) should remain constant with respect to wound size. More specifically, in order to keep the protease density constant as the wound size changes, it must be that if σ_w is scaled by some factor λ, then P_0 must be scaled by λ^2. These parameters appear in the dimensionless parameters $\gamma_P = \frac{[P]_0}{K_b} = \frac{1}{K_b} \cdot \frac{P_0}{2\pi r_d^2}$ and $\gamma_w = \frac{\sigma_w}{r_d^2}$. Therefore, scaling the wound size by a factor λ in the model corresponds to scaling γ_w by λ and scaling γ_P by λ^2.

Starting with a best fit parameter set, the wound size was then varied using scaling factors of λ from 0.5 to 1.5 in step sizes of 0.1. An example of the calcium signal radius for each scaling factor is shown in Fig. 6E. Values of $t_{0,\min}$ and α_{eff} were then determined for each new parameter set by fitting the delayed diffusion model to the RD model output. The delayed diffusion model, discussed in more detail in [8], describes the calcium signal radius by the equations

$$R_S^2 = 2\sigma^2 \ln\left[\frac{1}{2\pi\sigma^2(C_{th}/M)}\right] \tag{58}$$

$$\sigma^2 = \sigma_0^2 + 2\alpha(t - t_0) \tag{59}$$

The effective diffusion constant α was obtained by directly fitting the RD model output to equations (58) and (59), while the time delay $t_{0,\min}$ was obtained from fits to (58) and (59) by

$$t_{0,\min} = t_0 - \frac{\sigma_0^2}{2\alpha} \tag{60}$$

In other words, the time delay is the time when σ from equation (59) is equal to 0 given the best fit parameters to equations (58) and (59).

Mthl10-reduction internally-controlled expression model

In order to simulate an internally-controlled system where Mthl10 is reduced on half of the tissue, the model must be modified in the following ways:

1. Unlike the original model, which assumes a uniform initial tissue, the internally-controlled system no longer has rotational symmetry. Therefore, the species in the model need to be expressed as functions of both distance from the wound center r as well as the polar angle θ, and periodic boundary conditions are implemented so that for each diffusible species x_i, $x_i(r, 0, t) = x_i(r, 2\pi, t)$. The periodic behavior of the non-diffusible species is not explicitly implemented, as it follows automatically from the diffusible species' periodic boundary conditions.

2. The total amount of receptor is reduced on half of the tissue by reducing the parameter $\gamma_R = [R]_T/K_r$ for $\pi/2 < \theta < 3\pi/2$. Therefore, the parameter γ_R now becomes a piecewise function in space

$$\gamma_R = \begin{cases} \lambda \cdot [R]_T/K_r & \text{for } \pi/2 < \theta < 3\pi/2 \\ [R]_T/K_r & \text{otherwise} \end{cases} \tag{61}$$

   Where $0 \leq \lambda \leq 1$

3. In order to compare the $[L \cdot R]/[R]_T$ output between each side of the tissue, $[L \cdot R]/[R]_T$ on the Mthl-10 reduction side needs to be multiplied by λ so that the fraction is relative to $[R]_T$ on the control side.

An example of the $[L \cdot R]/[R]_T$ output of the above model is shown in Fig. 7A

Initial pro-Gbp concentration scaling of the model

In addition to wound size, the reaction-diffusion model can be scaled in terms of other system parameters as well. More specifically, the model can be used to investigate how the system behaves due to a reduction in pro-Gbp levels . The initial pro-ligand concentration appears in the dimensionless parameters $\gamma_{pL} = \frac{[pL]_0}{K_b}$ and $\gamma_L = \frac{[pL]_0}{K_r}$. Therefore, scaling the initial pro-ligand concentration by a factor λ in the model corresponds to scaling both γ_{pL} and γ_L by λ. Results of this scaling are shown in Fig. 7C.

CHAPTER 4 SUPPLEMENTAL FIGURES

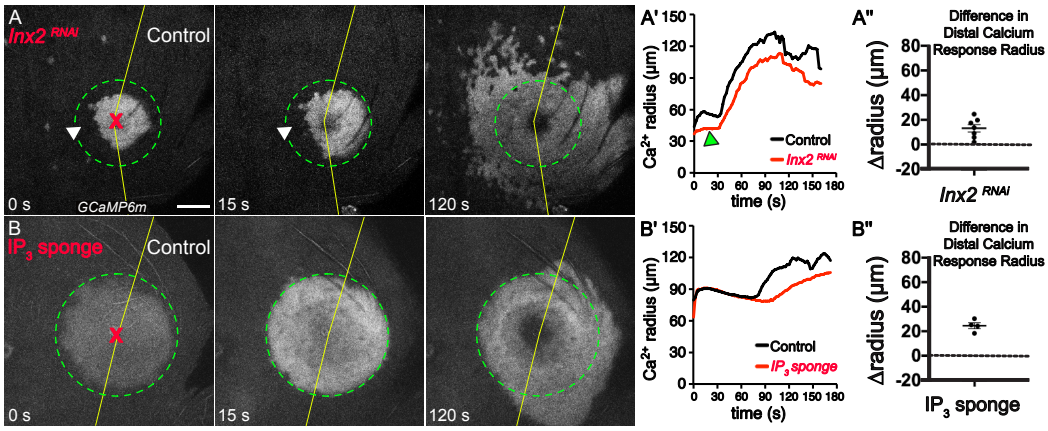

Chapter 4, Figure S1: Wounds signal calcium to proximal cells through gap junctions and to distal cells through IP_3.
(**A-B**) GCaMP6m reporter showing cytosolic calcium in representative samples of various knockdowns in the *Drosophila* notum. Gene manipulations are performed in the *pnr* expression domain (left side) and wounds (red X) are administered at the *pnr* domain boundary (yellow line). Maximum extent of first expansion is marked by dashed green circle. Scale bar = 50 µm. (**A**) Knockdown of gap junctions (*Inx2*^{RNAi}) attenuates first calcium expansion (arrowheads) (n = 7); the distal calcium response still occurs in the knockdown domain, but with a "speckled" pattern, as reported previously [14,42,150]. Although the *Inx2* knockdown appears to cause a slight reduction in calcium radius (**A'–A''**), the speckled nature of the signal would cause the automated algorithm that identifies the radius to underestimate it. (**B**) Expression of an IP_3 sponge has no effect on the first calcium expansion, but the distal calcium response is delayed (n = 4). (**A''–B''**) Difference in calcium signal radii (Δradius) at maximum extent of the distal calcium response for control minus pnr sides of each wound; pnr-side genotypes indicated. IP_3 sponge was statistically significant (*$p<0.05$) by one-way ANOVA, which included all genotypes from Fig. 1, Fig. 2, and Fig. S1, multiple comparisons WRT control group from Fig. 1.

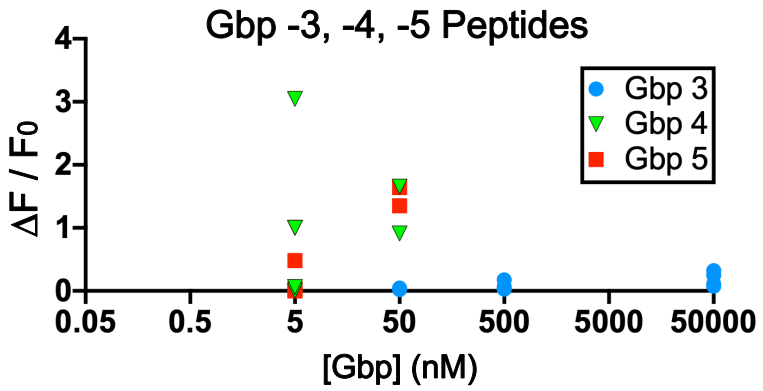

Chapter 4, Figure S2: Gbps 4 and 5 are also sufficient to elicit calcium responses in wing discs.
Change in GCaMP6m calcium fluorescence when a given concentration of Gbp -3 (n = 15), -4 (n = 7), or -5 (n = 7) peptides is added to *Drosophila* wing imaginal discs. Even at 50 μM, Gbp3 (blue circle) does not elicit a calcium response. Gbp4 (green triangle) elicits an inconsistent response at 5 nM, and consistently when added at 50 nM. Gbp5 peptide elicits a calcium response at 50 nM.

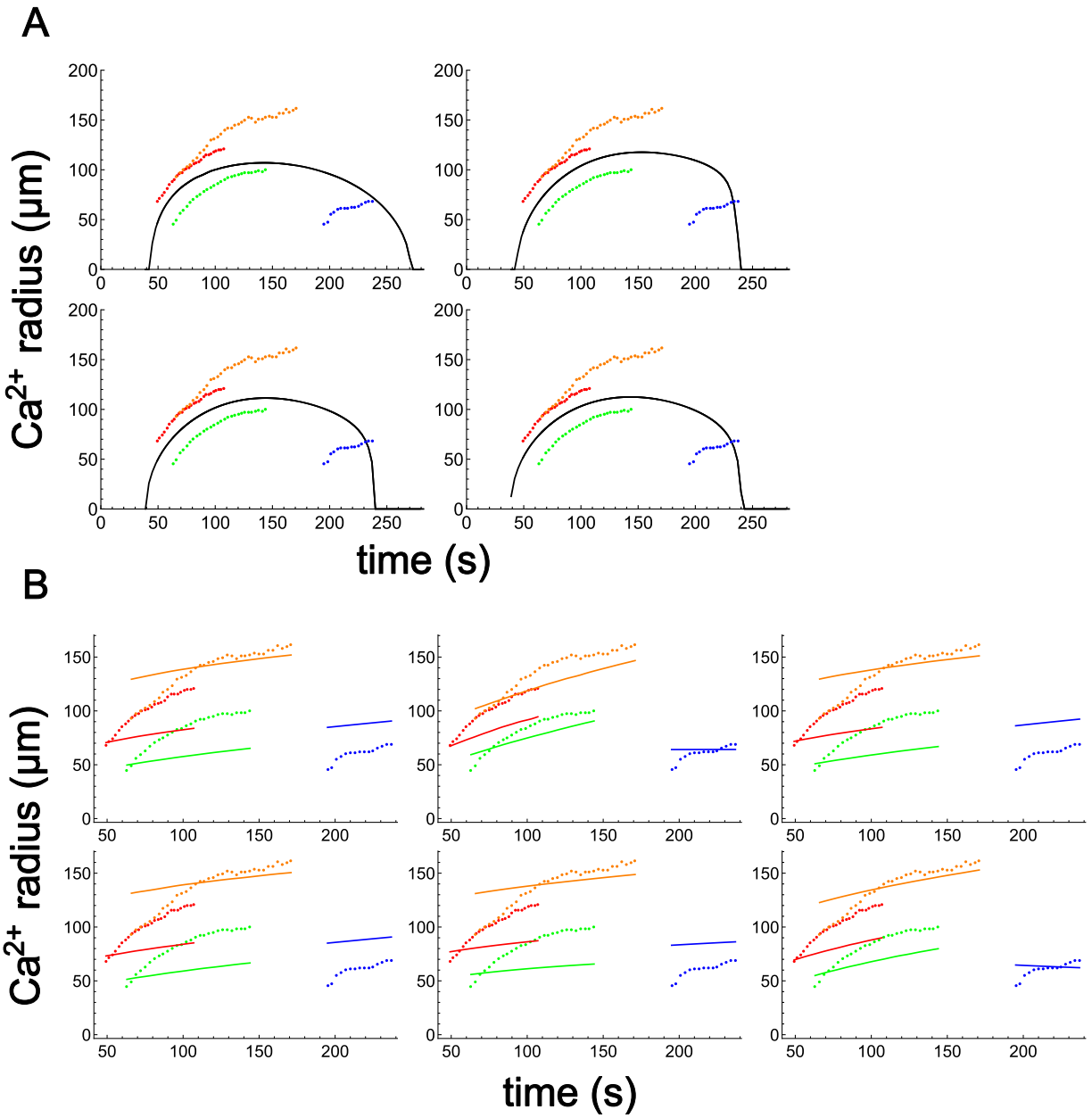

Chapter 4, Figure S3: Results of simultaneously fitting the reaction-diffusion model to four selected experimental samples.
(**A**) Four results of running the fitting process trying to minimize the cost function for all data sets simultaneously with a single parameter set. Model output is given by the black line, and distal calcium response data (colored points) are color coded based on the colors in Fig. S4.
(**B**) Six results of running the fitting process trying to minimize the cost function for all data sets simultaneously with a single base parameter set that is scaled according to the wound size of each distal calcium response (See "Distal calcium response properties from the model" supplement section for specifics on scaling parameters based on wound size). Model output (lines) and distal calcium response data (points) are color coded based on the colors in Chapter 4, Figure S4. Colored lines correspond to model output given the wound size of the same colored distal calcium response data points.

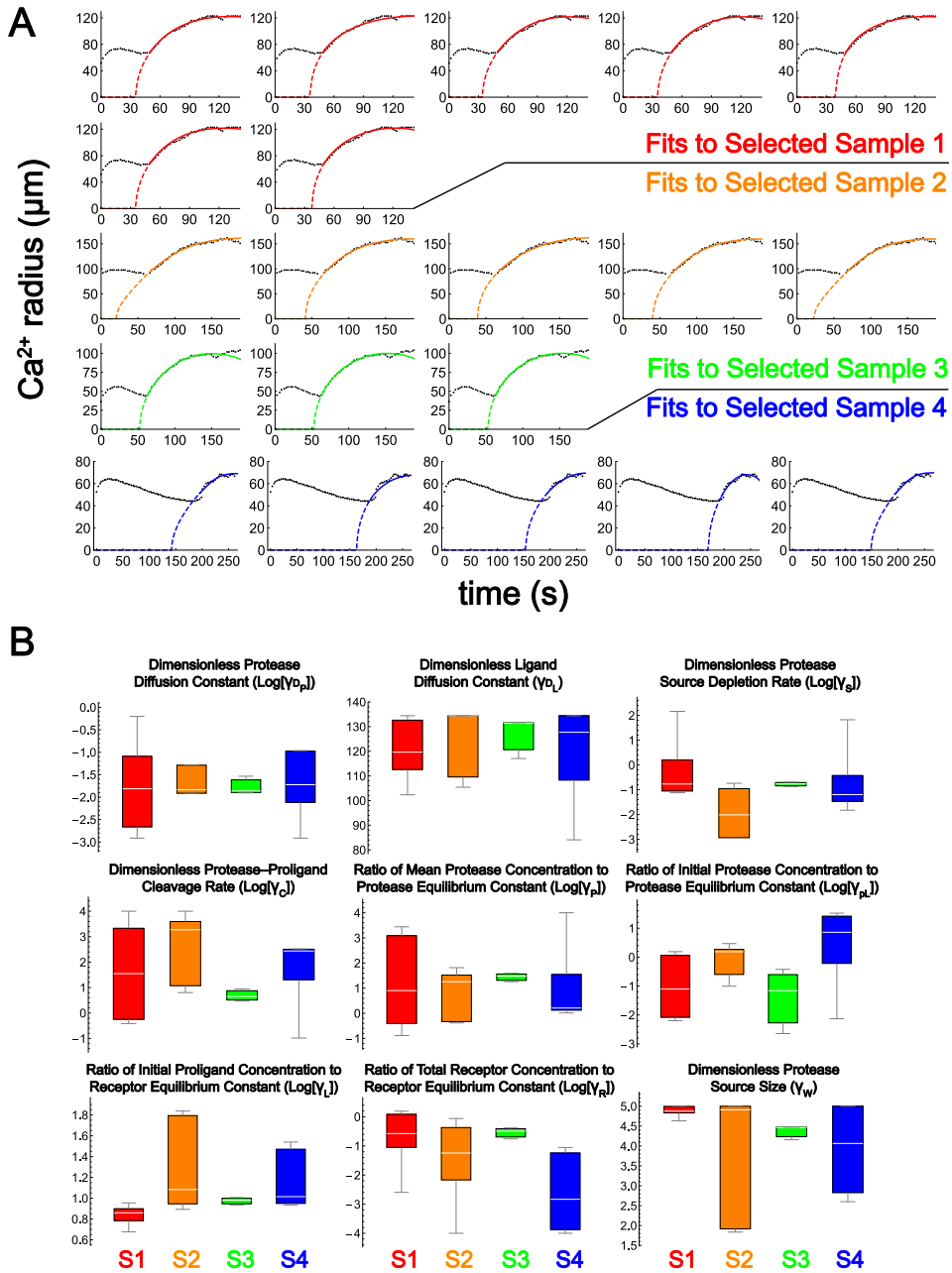

Chapter 4, Figure S4, related to Figure 6: Results of fitting the reaction-diffusion model to four selected experimental samples.
(**A**) Calcium signal radius versus time after wounding: experimental data (black circles), and RD model fits (colored lines). Each graph is a different best RD model fit to the distal calcium response data. (**B**) Box and whisker plots of best fit parameters to each selected distal calcium response. Parameters are defined further in the Supplemental Text. Colors correspond to the colors in A. Note that some of the plots correspond to the logarithm of the parameters to emphasize spreads across orders of magnitude.

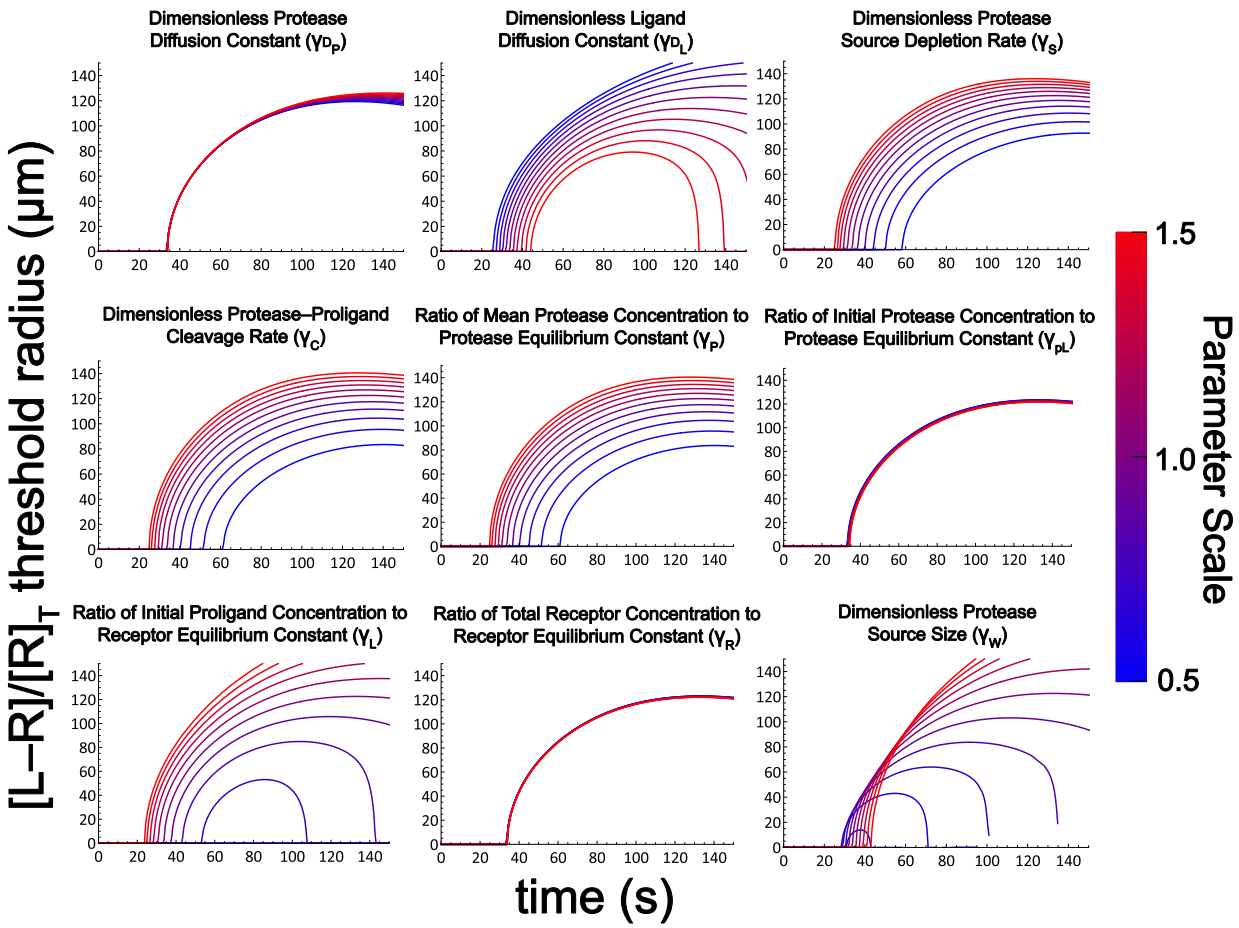

Chapter 4, Figure S5: Parameter variation effect on RD model output.
Calcium signal radius when varying a single parameter from a set of RD parameters determined from the best fit to an individual wound response (Purple line, Fig. 6D). Parameter scale indicates by how much the corresponding parameter was scaled to obtain lines of the corresponding color.

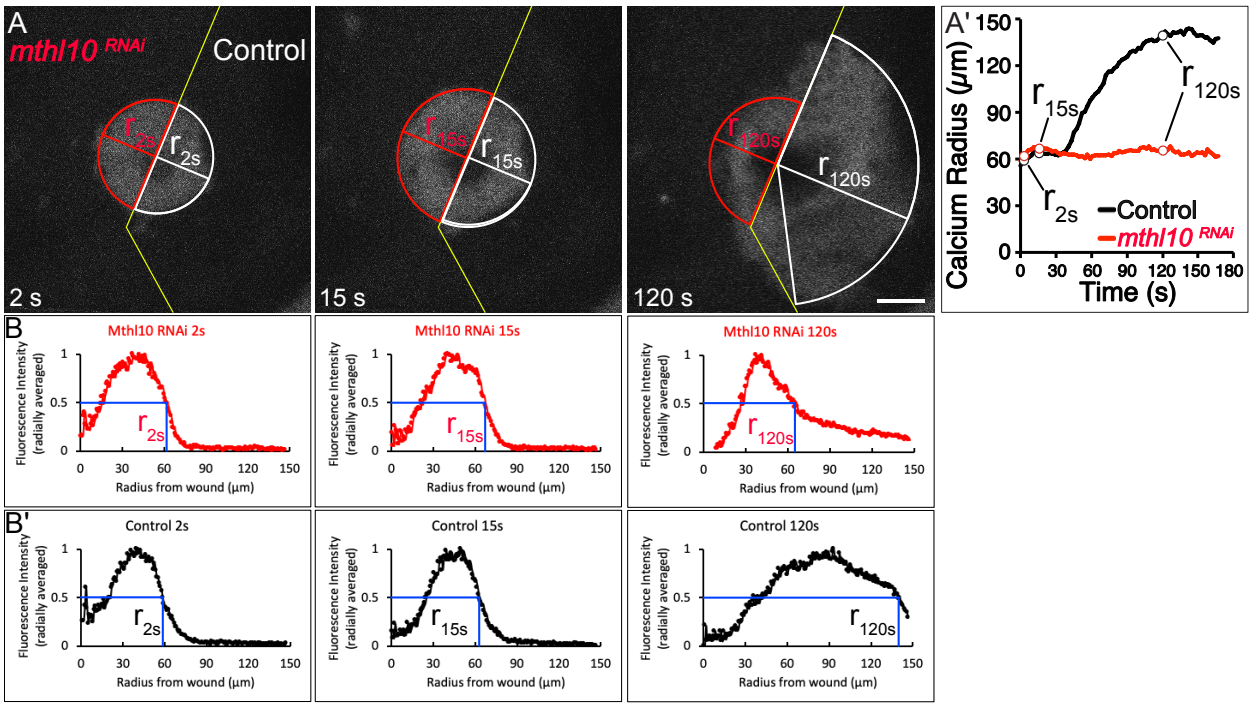

Chapter 4, Figure S6: Radial analysis of calcium signaling.
(**A**) Illustration of the radius analysis, applied to the sample shown in Fig. 2C. The averaged calcium radius is defined for the knockdown and control sides at each time point independently, which can then be graphed as a function of time (**A'**). (**B, B'**) At each time point, the MATLAB program analyzes the radially averaged fluorescence intensity, and determines the upper radius of half maximum to define the calcium radius. The experimental domain (**B**) and internal-control domain (**B'**) are analyzed independently, delineated by *pnr>mCherry.NLS* (as in Fig. 1B). Scale bar = 50 μm.

Supplemental Movies can be found in the supplementary material of O'Connor, et al. *Dev Cell.* 2021.[113]

Chapter 4, Movie S1: Calcium signaling is observed in response to wounds in *Drosophila* pupae.
Calcium response to wounds, monitored by GCaMP6m, is symmetric on both sides of the *pnr* boundary (yellow line) in the absence of gene knock-down (*pnr>mCherry-NLS*). The maximum radius of the rapid first expansion is marked by green circle. Scale bar = 50 μm.

Chapter 4, Movie S2: The distal calcium response requires components of the Gq-signaling pathway.
Calcium response to wounds is monitored by GCaMP6m. The maximum radius of the rapid first expansion is marked by green circle. The distal calcium response only occurs in the control side of each movie, and not on the side where *IP_3R*, *Plc21C*, or *$G\alpha q$* is knocked down. Scale bar = 50 μm.

Chapter 4, Movie S3: Puncture wounds recapitulate laser wounds in *Drosophila* pupae.
Calcium response to wounds is monitored by GCaMP6m in response to puncture by an electrolytically sharpened needle. Pupal nota were imaged with a 5X objective to give working distance for manual puncture. Scale bar = 100 μm.

Chapter 4, Movie S4: The distal calcium response can jump from the Gq knockdown domain to the control domain.
Wound targeted within the $G_{\alpha q}$ knock-down domain (magenta, left of yellow line). Calcium response to wounds is monitored by GCaMP6m (green). The maximum radius of the rapid first expansion is marked by green circle. The distal calcium response is absent from the $G_{\alpha q}$ knock-down domain until the signal diffuses into the nearby control domain (right of the yellow line). Scale bar = 50 μm.

Chapter 4, Movie S5: The distal calcium response requires the GPCR Methuselah-like 10.
Calcium response to wounds is monitored by GCaMP6m. The maximum radius of the rapid first expansion is marked by green circle. The distal calcium response only occurs in the control side and not on the side where Mthl10 is knocked down. Scale bar = 50 μm.

Chapter 4, Movie S6: Gbp1 and Gbp2 elicit a calcium response in wing discs in an Mthl10-dependent manner.
Control (white outline) and *mthl10* knockdown (red outline) wing discs mounted together in the same media bubble. Gbp1 added at t = 0 seconds to 5 nM final concentration (left), or Gbp2 added at t = 0 seconds to 50 nM final concentration (right), elicits a calcium response in only the control disc, monitored by GCaMP6m. Scale bar = 100 μm.

Chapter 4, Movie S7: *Drosophila* extract elicits a calcium response in wing discs in an Mthl10-dependent manner.
Control (white outline) and *mthl10* knockdown (red outline) wing discs mounted together in the same media bubble. Adult fly extract (left) or larval extract (right), added at t=0 to 5% final concentration, elicits a calcium response in only the control discs, monitored by GCaMP6m. Scale bar = 100 μm.

Chapter 4, Movie S8: Larval extract elicits a calcium response in wing discs in a Gbp-dependent manner.
Control (white outline) and Δ*Gbp1,2* (red outline) wing discs mounted together in the same media bubble. Δ*Gbp1,2* larval extract, added at t=0 to 5% final concentration, elicits a calcium response in only the control disc, monitored by GCaMP6m. Scale bar = 100 μm.

Chapter 4, Movie S9: Model output of scaled molecular component concentrations and calcium signal radius vs. time
(A) Protease concentration scaled by the concentration of total protease within an area of ~638 μm^2 (see supplementary information). (B) Free pro-ligand and ligand concentrations scaled by the initial pro-ligand concentration. (C) Free receptor and bound receptor concentrations scaled by the total receptor concentration. The bound receptor threshold for triggering calcium release is taken as 0.5 (dashed line). Red point indicates where the bound receptor concentration crosses this threshold. (D) Calcium signal radius as a function of time as determined from the point in space where the bound receptor crosses the signaling threshold. Red point indicates the signal radius at the corresponding point in time.

CHAPTER 5

ADDITIONAL MODULATORS OF WOUND-INDUCED CALCIUM SIGNALING

Introduction

This project has sought to understand the initiators of the damage-induced increase in cytosolic calcium observed after wounding. Previous work characterized an initial influx of extracellular calcium rushing into damaged cells through plasma membrane microtears, which then diffuses outward to neighboring cells through gap junctions[14]. Chapter 4 characterized a second calcium expansion that occurs through ER calcium release. This second calcium expansion can travel outward to distal cells at least 150 μm away from the wound site, before devolving into asymmetric oscillatory flares. This chapter will better characterize additional modulators of the wound-induced calcium signaling events, including the proteins that play a major role in creating the unique spatiotemporal dynamics of the distal calcium response and subsequent flares.

Cytosolic and organelle calcium is tightly regulated by a series of proteins that maintain the cytosolic calcium concentration at approximately 100 nM and endoplasmic reticular calcium concentration nearly four orders of magnitude higher at approximately 500 μM[18,19]. To do this, ion channels shuttle calcium into or out of the cytosol from organelles or the extracellular space (where calcium is maintained at approximately 1 mM)[18], We have thoroughly explored the IP_3 Receptor in Chapter 4, which releases calcium from the ER in an IP_3 dependent manner. In response, SERCA (sarcoplasmic/endoplasmic reticulum Ca2+-ATPase) pumps calcium back into the ER from the cytosol[59,60]. Thus, IP_3R and SERCA maintain the balance of ER calcium by letting calcium out of or into the ER, respectively.

PLCβ Overexpression Alters Calcium Responses

Wound-induced production of active Gbp leads to the sequential activation of Mthl10, Gαq, and PLCβ, resulting in a dramatic increase in cytosolic IP_3 that leads to ER calcium release through the IP_3R. However, this process can be simulated by a simple overexpression of PLCβ in the *Drosophila* pupa. Overexpression of PLCβ through *pnr-Gal4 > UAS-PLC21C* leads to spontaneous calcium flashes in the *pnr* region, even without a wound (Chapter 5, Figure 1A). These calcium flashes often expand outward from a single point, and can repeatedly fluctuate in a similar manner to wound-induced calcium flares following the second calcium expansion. After wounding on the border of PLCβ overexpression, the second calcium expansion spreads farther than in control samples. The calcium expansion often breaks away from the first calcium expansion and acts as an isolated travelling calcium wave, similar to the calcium flares that generally occur after the second calcium expansion (Chapter 5, Figure 1B). Furthermore, these wound-induced calcium flares can undergo wave-annihilation[182,183] with spontaneous calcium flashes in PLCβ overexpression pupae (Chapter 5, Figure 1C); if a spontaneous calcium flash travelling medial to lateral approaches a wound-induced calcium flare travelling in the opposite direction, neither will continue to propagate passed the other. This is because each travelling wave approaches a set of cells that has just released calcium from its respective ER. This means that the oscillatory calcium increases caused by both spontaneous calcium flashes and wound-induced calcium flares are determined by the ER refractory period, the time in which the IP_3R is unable to re-release calcium (even in the presence of cytosolic IP_3) because the ER has been depleted of calcium[38].

SERCA, STIM, and PMCA Modulate the Calcium Response

As mentioned above, IP_3-mediated calcium release from the ER is balanced by SERCA pumping cytosolic calcium back into the ER[59,60]. In the *Drosophila* pupa, prolonged knockdown of SERCA through *pnr-Gal4 > UAS-SERCA RNAi* is lethal. However, a more temporary

knockdown of SERCA will cause the excess cytosolic calcium in the affected cells, as determined by increased fluorescence of GCaMP6m in *pnr* cells compared to control cells, even before wounding has occurred (Chapter 5, Figure 2A). Further, upon laser ablation on the border of *SERCA RNAi* expression, the knockdown cells appear to have a normal first and second calcium expansion, but dramatically reduced flaring thereafter with GCaMP6m fluorescence remaining consistently elevated for longer compared to the control domain (Chapter 5, Figure 2A). This fits with the model that SERCA pumps calcium back into the ER after IP_3-mediated calcium release in the distal calcium response.

Another set of proteins that maintain ER calcium homeostasis are STIM and Orai. STIM works by sensing when calcium levels in the ER are depleted and activating Orai on the plasma membrane, which in turn allows calcium to enter the cytosol from the extracellular space[18,31]. We predicted that, if flares were caused by calcium being re-released by the ER repeatedly after the initial IP_3-mediated release, then a STIM knockdown should decrease the number of times a single cell can “flare” because a small amount of ER calcium is lost into the extracellular space through the plasma membrane calcium ATPase (PMCA) each release, without getting any replenishment from Orai. Indeed, knockdown of STIM through *pnr-Gal4 > UAS-STIM RNAi* causes the knockdown region cells to flare for approximately four minutes while the flares continue in control domain for approximately six minutes (Chapter 5, Figure 2B).

As mentioned above, the PMCA channel removes excess calcium from the cytosol into the extracellular space, helping to maintain a low calcium concentration in the cytosol compared to the high extracellular concentration. Upon knockdown of PMCA in the pupa through *pnr-Gal4 > UAS-PMCA RNAi*, the amount of time that calcium is retained in the cytosol after injury is dramatically increased, especially in the region of the initial influx and first calcium expansion where extracellular calcium has rushed into cells (Chapter 5, Figure 2C). This demonstrates that PMCA plays a role in clearing wound-induced calcium from the cytosol in the cells around an injury. However, the *PMCA RNAi* phenotype does appear to be mostly affect the cells in the

region within the first calcium expansion radius, rather than the region of the distal calcium response. This makes sense considering the first expansion calcium originated in the extracellular space, and will likely be pumped back out of the cell, while the distal calcium response originated from the ER, meaning this calcium will likely be pumped back into the ER. This also explains the difference in phenotype between *PMCA RNAi* and *SERCA RNAi*.

These four experiments help to explain some of the cellular calcium dynamics that remained unexplored in Chapter 4, including the wound-induced flares. When cytosolic calcium is high, whether through extracellular calcium rushing in, gap-junctional transfer, or through ER calcium release, the PMCA channel will work to pump calcium out of the cytosol and into the extracellular space. When ER calcium release occurs specifically after increased cytosolic IP_3, SERCA pumps calcium back into the ER. After a refractory period during which the ER is refilled with calcium, the excess cytosolic IP_3 may trigger another ER calcium release. This process which may occur repeatedly until the IP_3 in the cytosol is depleted or the ER calcium is no longer properly refilled. The latter may occur because each flare will cause some ER calcium to be released into the cytosol, some of which will inevitably be pumped into the extracellular space by PMCA. Therefore, if even a small amount of ER calcium gets lost to the extracellular space per cycle, then repeated cycles may see the ER eventually depleted of sufficient calcium. To prevent this from occurring, STIM activates Orai after ER calcium depletion to bring extracellular calcium into the cytosol. Thus, these five proteins of IP_3R, SERCA, PMCA, STIM, and Orai all modulate the wound-induced increase in cytosolic calcium, and each play a role in the dynamics of the calcium flares and eventual return to homeostasis of calcium in the minutes following a wound.

Mechanosensitive Ion Channels Are Not Required for the Calcium Response

An additional potential mechanism of calcium signaling following a wound is through mechanosensation. Mechanosensitive ion channels such as piezo detect changes in cortical tension in cells, resulting in extracellular calcium entry into the cytosol[27–29]. Indeed, release of

cellular tension was shown to modulate calcium signaling in imaginal wing discs[149] in the presence of fly extract, which we showed in chapter 4 activates calcium signaling through Growth-blocking peptides and Methuselah-like 10. Because changes in cellular tension modulate the calcium response in wing discs, we hypothesized that changes in cellular tension may also modulate the distal calcium response in pupae after wounding.

Previous work from other labs has implicated transient-receptor potential (TRP) channels, some of which can be activated through mechanosensation[32,33], in extracellular calcium entry after wounding[6,7]. Furthermore, the act of wounding causes a dramatic disruption to the tissue's structure by destroying cells (and thereby their adhesions to neighbors), creating an imbalance in the cellular forces and restructuring the cortical tension on the tissue[184–186]. This change in cortical tension might be sufficient to activate a mechanosensitive ion channel in the cells proximal to a wound.

To test the role of potentially mechanosensitive ion channels in the wound-induced calcium response, we used the internally-controlled system to wound on the border of expression in pupae expressing a knockdown of either piezo or the previously implicated calcium channel TRPm. However, in both cases the calcium response after wounding was unchanged, showing that neither piezo nor TRPm are required for a normal calcium response after wounding (Chapter 5, Figure 2D, Chapter 4, Fig 2). It is worth noting that our system, and *ActinP-GCaMP6m* specifically used in our studies, is much better suited to study the spatiotemporal dynamics of the calcium response, rather than the concentration of cytosolic calcium. Therefore, TRPm and/or Piezo could theoretically play a minor role in the amount of cytosolic calcium induced after wounding.

Mechanosensation May Play a Sensitizing Role in the Calcium Response

Although we did not observe a difference in the calcium response after knockdown of TRPm or Piezo, changes in cellular tension may still modulate the distal calcium response after wounding by somehow sensitizing the cell (or any of the proteins involved in the signal cascade

specifically) to the wound signals through an unknown mechanism. To test this possibility, we used the internally-controlled system to manipulate cortical tension in the pupal notum by expression of a knockdown of the Rho-kinase (Rok) that phosphorylates myosin II (a manipulation that should decrease cortical tension), or by expression of a phosphomimetic form of myosin II light chain (sqhEE) (a manipulation that should increase cortical tension). Neither of these changes produced a significant difference in the radius of the wound induced calcium response in the expression domain compared to the control domain. However, the distal calcium response occurred an average of 6 seconds earlier in the expression domain of the SqhEE pupae compared to its control domain, which was significantly different from the response in the Rok RNAi pupae which occurred an about 1 second later in the expression domain compared to its control (Chapter 5, Figure 3). While this difference in calcium response in response to manipulated tension is very subtle, it shows that the ability of the cells to properly transduce the wound-induced calcium signals may be sensitized by cortical tension. Another reason for the relatively subtle response may be that the epithelial cells in the expression domain are continuous with the epithelial cells in the adjacent control domain, potentially causing any tension manipulation in the expression domain to propagate to the control domain, reducing its comparative effect. Regardless, the effect size would still be vastly smaller than the effect of the Mthl10/Gq-pathway manipulations shown in Chapter 4, so we conclude that the major driving factor in the distal calcium response is biochemical in nature, with mechanosensation only playing a relatively small sensitizing role at most.

Conclusions

By overexpression of PLCβ and knockdown of SERCA, we found the oscillatory calcium flares are a byproduct of the IP_3-mediated ER calcium release. After PLCβ activation leads to increase production of IP_3, calcium is released into the cytosol through IP_3R, after which it is pumped back into the ER by SERCA. Because some cytosolic calcium is lost to the extracellular

space through PMCA, the ER protein STIM activates Orai to allow extracellular calcium entry to help replenish the lost calcium and maintain ER calcium stores[18,31]. We find that knockdown of STIM reduces the duration of the flares after wounding. PMCA knockdown also increased the amount of time calcium remains in the cytosol following the initial influx and first expansion. Finally, we found that manipulating cortical tension in the tissue can change the distal calcium response start time, demonstrating a role for cortical tension in sensitizing the tissue to the calcium response.

CHAPTER 5 FIGURES

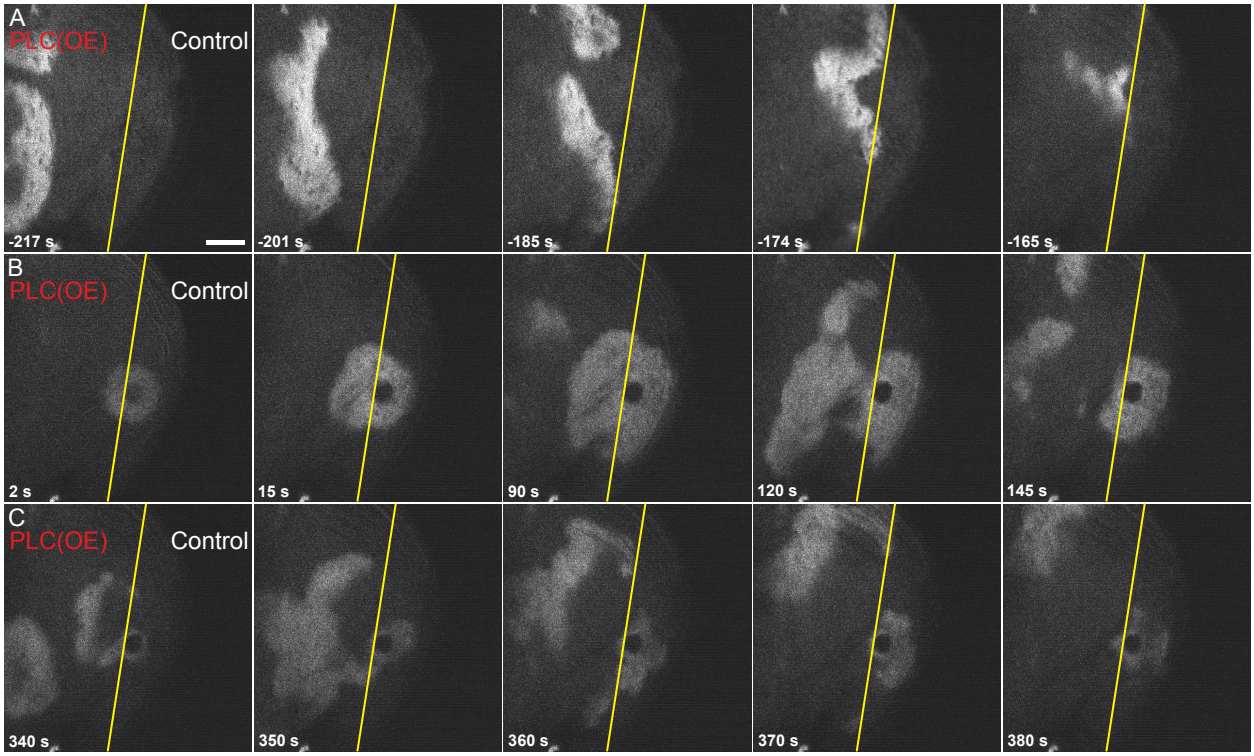

Chapter 5, Figure 1. PLC Overexpression increases the cellular calcium response
(A–C) PLC is overexpressed in the *pnr* domain (left) adjacent to the internal control domain (right), as delineated by yellow line. GCaMP6m calcium reporter is ubiquitously expressed. Scale bar = 50 µm. (A) Even prior to wounding, spontaneous calcium flashes occur in the *pnr* domain. The calcium flashes spread in a wavelike manner, similar to wound induced calcium expansions. (B) Calcium response after wounding (at t = 0 s) appears modified in the *pnr* domain, with the calcium response often breaking away from the initial influx/1st expansion calcium, and often travelling farther than the distal calcium response in the control domain. (C) Spontaneous calcium waves from the *pnr* domain will undergo wave annihilation with the distal calcium response/flares, demonstrating the calcium flares are dependent upon the refractory period of the endoplasmic reticulum's calcium release; as the wound-induced flares travel from right-to-left they encounter cells that have just experienced a spontaneous calcium flash travelling from left-to-right so they cannot release calcium again (and vice versa), causing the two waves to annihilate each other.

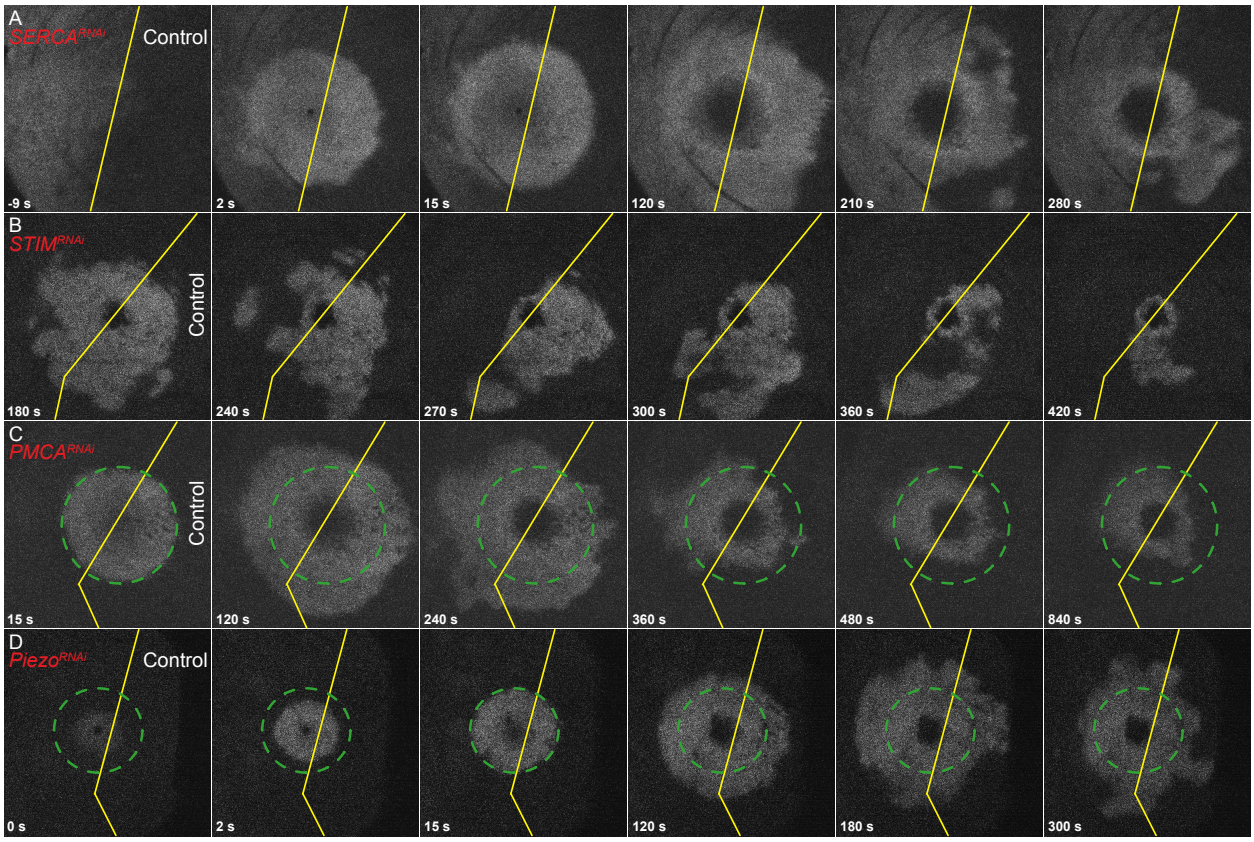

Chapter 5, Figure 2. Various calcium modulators change the wound-induced calcium response.

(A–D) UAS-RNAis are expressed in the *pnr* domain (left) adjacent to the internal control domain (right), as delineated by yellow line. GCaMP6m calcium reporter is ubiquitously expressed. Scale bar = 50 μm. (A) *SERCA*^{RNAi} expression causes increased GCaMP6m fluorescence in the *pnr* domain, even before wounding. After wounding, the distal calcium response appears to travel slightly farther than in the control domain, and remain in the cytosol while the control domain calcium response devolves into flares, showing SERCA is required for calcium reuptake into the ER after the distal calcium response and before the flares. (B) *STIM*^{RNAi} expression retains a normal distal calcium response and flares initially, but the flares subside after about 4 minutes in the expression domain whereas flares persist in the control domain for about 7 minutes, showing that STIM plays a role in replenishing cellular/ER calcium following repeated reuptake/flare events. (C) *PMCA*^{RNAi} expression has a normal distal calcium response and flares, but the calcium in the expression domain–especially near the first expansion region (green circle)–persists in the cytosol for much longer than the control domain. While the cytosolic calcium in cells outside the first expansion region usually dies down around 7 minutes, it often persists for at least 15 minutes in the *PMCA*^{RNAi} region. (D) *Piezo*^{RNAi} expression has a normal initial influx, first calcium expansion, distal calcium response, and flares, showing the mechanosensitive ion channel Piezo is not required for any aspect of the wound-induced calcium response.

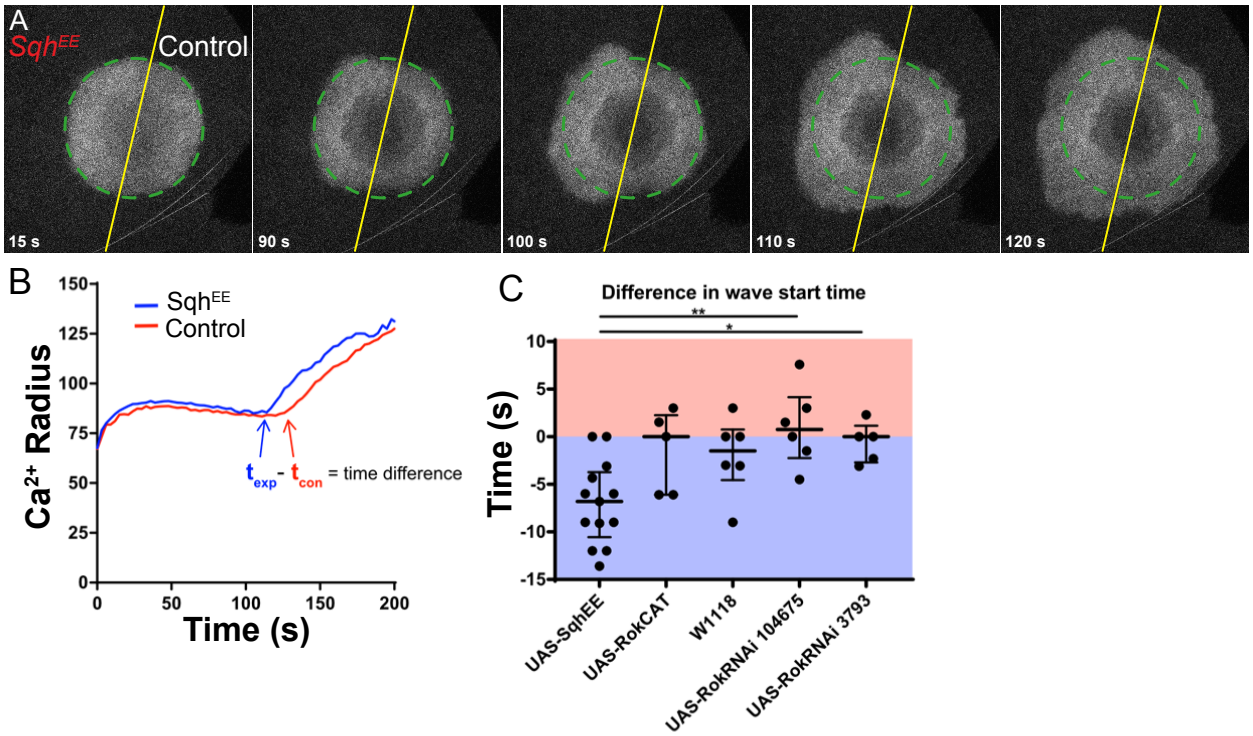

Chapter 5, Figure 3. Cortical tension modulator SqhEE sensitizes cells to the distal calcium response

(A) Phosphomimetic form of myosin-II light chain, *SqhEE* is expressed in the *pnr* domain (left) adjacent to the internal control domain (right), as delineated by yellow line. GCaMP6m calcium reporter is ubiquitously expressed. Scale bar = 50 µm. (A) *SqhEE* expression causes the distal calcium response to begin slightly earlier in the *pnr* domain compared to the internal control domain. (B) Representative quantification of calcium radius vs time, showing the distal calcium response begins slightly earlier in the *SqhEE* expression domain. The time difference in distal calcium response start time can be easily calculated as the difference between the expression domain and control domain. (C) Quantification showing that *SqhEE* expression (which increases cortical tension) causes the distal calcium response start time to be significantly decreased compared to Rok^{RNAi} expression (which decreases cortical tension), showing cortical tension may sensitize the distal calcium response. Analysis by one-way ANOVA, *$p < 0.05$, **$p < 0.01$. Data gathered in collaboration with former Page-McCaw lab graduate student Erica Shannon.

CHAPTER 6

WOUND-INDUCED CHANGES IN CYTOSKELETON AND EPITHELIAL TENSION

Introduction

Chapters 2–5 focused on understanding the immediate aftermath of a wound and the initiation of calcium signaling within the first ~five minutes after a wound. However, there are numerous other factors and cellular behaviors that occur downstream of (or independent of) calcium signaling that play a crucial role in the repair process. In order to understand the variety of cellular behaviors that aid in the wound response, we used live imaging of genetically encoded fluorescent proteins to monitor repair beyond the time frame of calcium signaling. Because of the stationary nature of *Drosophila* pupae, we were able to live image the notum throughout the entire repair process, generally on the order of six hours for typical laser wounds. In doing so, we sought to understand each of the pathways that are required for repair, and the role that calcium signaling might play in sparking the repair response.

Chapter 5 introduced the concept that cortical tension changes upon wounding–the epithelial sheet is junctionally connected, and therefore any wound created in that sheet will cause all of the proximal cells to spring back as the wounded cells' junctions are severed[114,186]. We also showed that tension changes may play a small role in sensitizing the cells around a wound to calcium signaling. However, after the initial springing back after wounding, the cells will re-equilibrate their forces and the tension will be reset[24,186,187]. As this happens, the cells will dynamically shift their cytoskeletal proteins, namely actin and myosin, accordingly. What does this wound-induced cytoskeletal change look like, and does this process require calcium signaling?

Previous studies over the past two decades have used model organisms to characterize the changes in actin and myosin after single-cell wounds[20,169,188] and in multi-cellular, tissue

level wounds[6,68,188]. Briefly, the most prominent feature in both types of wounds is a contractile purse-string of actin and myosin that forms around the wound margin and progressively cinches the wound closed. As the purse-string tightens, it aids in cell migration by pulling the surrounding cells inwards to fill in the void in the center of the wound. When the purse-string has cinched the wound nearly closed, cells extend filopodia that reach across to grab cells on the opposite side and finally pull the wound shut[67,189,190]. By using a genetically expressed myosin-II-GFP (*Zip-GFP*), we visualized the heavy chain of non-muscle myosin II to watch this process occur in the *Drosophila* pupal notum during wound repair.

Myosin localization rapidly changes after wounding

Wounding myosin-II-GFP pupae recapitulated the results from previous studies, showing a supracellular actomyosin purse-string forming around the wound margin within the first 45 minutes after wounding (Chapter 6, Figure 1A). To test whether the distal calcium expansion is required for pursestring formation, we wounded pupae expressing myosin-II-GFP in a Δ*Gbp1,2* background that completely blocks the distal calcium expansion after wounding. We found that pursestring formation was not noticeably altered in the Δ*Gbp1,2* pupae, showing the distal calcium expansion is not required for the actomyosin pursestring (Chapter 6, Figure 1B). This does not preclude the possibility that calcium signaling as a whole is not involved, given that both the initial influx and first expansion still occur in Δ*Gbp1,2* pupae. Future experiments by James White in the Page-McCaw lab will probe whether making numerous small wounds (which aggregate to the same area as a normal single-shot pulsed-laser ablation but without the cavitation bubble and ensuing initial influx) causes a noticeable decrease in pursestring intensity and/or an increase in repair time.

Myosin relocalization is correlated with increases in cytosolic calcium

Although the distal calcium response does not seem required for pursestring formation, it may still play a different role in altering cytoskeletal dynamics. After wounding myosin-II-GFP pupae, we noticed two interesting behaviors in cells distal from the wound that indicate the distal

calcium response may affect the cytoskeleton. First, there is a distinct reorganization of myosin during the first 45 minutes after wounding, whereby the myosin-II-GFP becomes slightly less localized at the cell borders and appears to be more localized in the center of the cell (either in the apical cortex or in the cytosol). This behavior is first seen about 10 cells back from the wound margin a few minutes after wounding and progressively moves inwards towards the cells more proximal to the wound margin (Chapter 6, Figure 2A). Second, the cells that undergo this myosin reorganization behavior appear to contract as the reorganization begins and relax as it ends, causing cell area to transiently decrease (Chapter 6, Figure 2B, C). This behavior also occurs initially in the cells distal from the wound and progressively moves inwards towards the cells more proximal to the wound margin, as seen in Antunes, et al.[6]. To determine whether this cell contraction phenotype was related the calcium response, I worked with Page-McCaw lab rotation student Lilia Merbouche to wound pupae co-expressing the calcium indicator GCaMP6m with the cell border marker p120ctn-TagRFP, and analyze the cell area as a function of calcium intensity on a cell-by-cell basis. She found this cell contractility event was correlated with high levels of intracellular calcium, with analysis of contracting cells finding that cell area was inversely proportional to GCaMP6m fluorescence such that minimum cell area occurred at the same time as maximum GCaMP6m intensity. (Chapter 6, Figure 3). Further studies are needed to show whether the inverse proportionality between cell area and GCaMP6m fluorescence intensity over time holds for all cells around the wound, and to determine whether the increase in cytosolic calcium is causative of the cell contraction rather than simply correlated. Regardless, this data points to a role for the increase in intracellular calcium in the cell contractility events observed after wounding, as well as in the dynamic changes in myosin localization.

Discussion

Perhaps, even though the distal calcium expansion is not necessarily required for the eventual pursestring formation, it plays a role in the alteration of cytoskeletal dynamics and in

the re-equilibration of cortical tension following a wound. Page-McCaw lab undergraduate Ivy Han is currently in the process of severing single borders on either the radial or tangential axis relative to the wound and measuring the recoil velocity to determine the relative tension on that border. The concept is relatively simple–just as cutting a tug-of-war rope would send each of the participants flying backwards, severing a tension-bearing border will cause the nearest vertices to spring back with a velocity based on the tension of the severed border[185–187]. Thus, severing a border and measuring the recoil velocity of the nearest vertices can be used to map tension within an epithelial sheet[187].

To test the hypothesis that the distal calcium expansion plays a role in the re-equilibration of cortical tension after wounding, Ivy plans to measure the recoil velocity after junctional severing in cells around notal wounds in the presence or absence of Mthl10, before or after a wound has been made in the tissue. We hypothesize that creation of a wound in the tissue will cause a dramatic change in the cortical tension on the tissue. Further, if the distal calcium response plays a role in reorganizing the cytoskeleton after wounding, then knockdown of Mthl10 should impair the tissue's cytoskeletal dynamics leading to dysregulation of tissue tension after wounding. By doing these experiments in the internally-controlled system, Ivy will be able to directly compare the tension in the *mthl10 RNAi* expression domain as compared to the neighboring internal control domain in the same sample.

These experiments show that a rapid change in myosin localization within minutes of the wound, that is correlated with the cellular increase in cytosolic calcium. Because the reorganization of actin and myosin in the early response to wounds has previous been shown to be vital for proper wound repair[6,66,68,190], characterizing the interplay between calcium and cytoskeletal dynamics may be key to fully understanding how cells convert calcium signaling into a tissue-scale repair response. Perhaps the Mthl10-mediated calcium signal causes a calcium-mediated actin reset[72] allowing cells to restructure their cytoskeleton to convert from a stationary and quiescent state into a migratory and reparative state.

CHAPTER 6 FIGURES

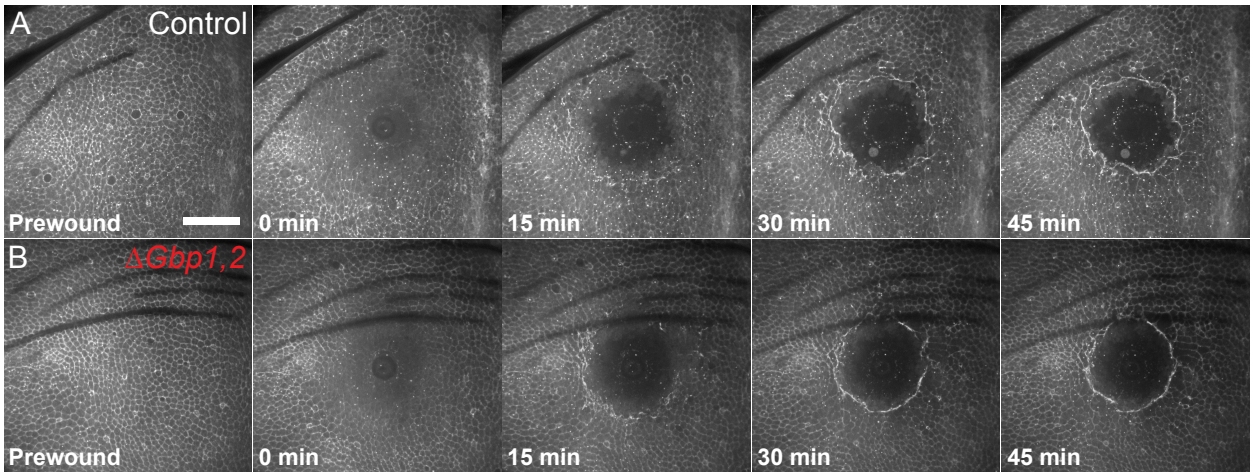

Chapter 6, Figure 1. The wound-induced actomyosin pursestring forms independently of Gbp1 and Gbp2.
(A–B) Myosin-II-GFP is ubiquitously expressed. Scale bar = 50 µm. (A) Myosin-II relocalizes rapidly within 45 minutes after wounding *Drosophila* pupae, resulting in a supracellular actomyosin pursestring that acts to cinch the wound closed. (B) In a Δ*Gbp1,2*, pursestring formation is unchanged, and wound closure rates do not appear to be altered.

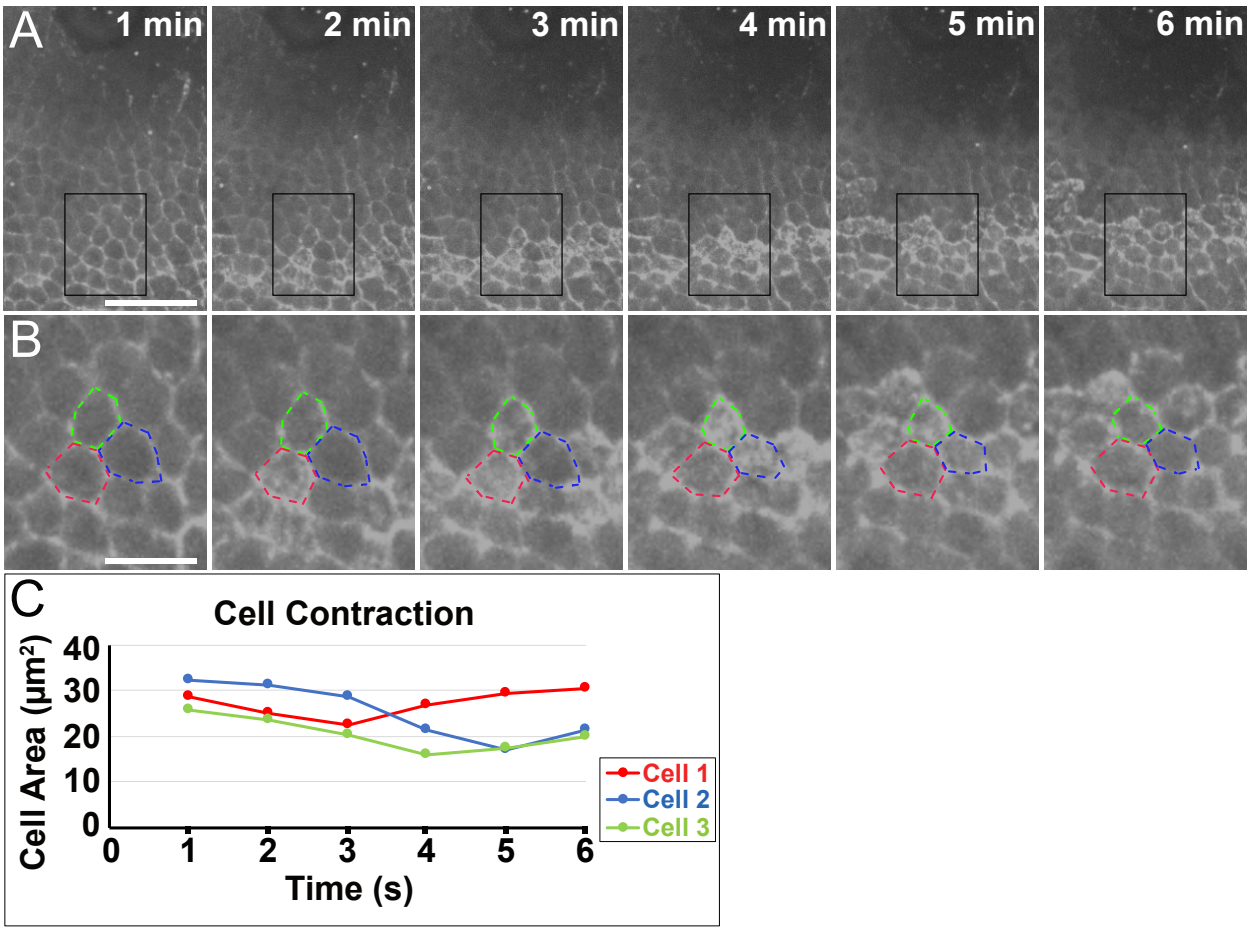

Chapter 6, Figure 2. Wounds cause relocalization of myosin
(A–B) Myosin-II-GFP is ubiquitously expressed. (A) Myosin-II cellular localization rapidly changes over the first few minutes after wounding, moving from cell borders to cytosolic/apical, beginning in cells approximately 75 μm from the wound. This phenotype progressively moves from distal cells to proximal cells over the first ~30 minutes after wounding. Black box shows panels depicted in B. Scale bar = 25 μm. (B) Myosin-II cellular relocalization is associated with a transient cell contraction. 3 example cells are outlined to show their cell contraction events over the first six minutes after wounding. Scale bar = 10 μm. (C) Quantification of cell area of the 3 cells in panel B, showing a transient cell contraction that is associated with the myosin relocalization visible in panels B.

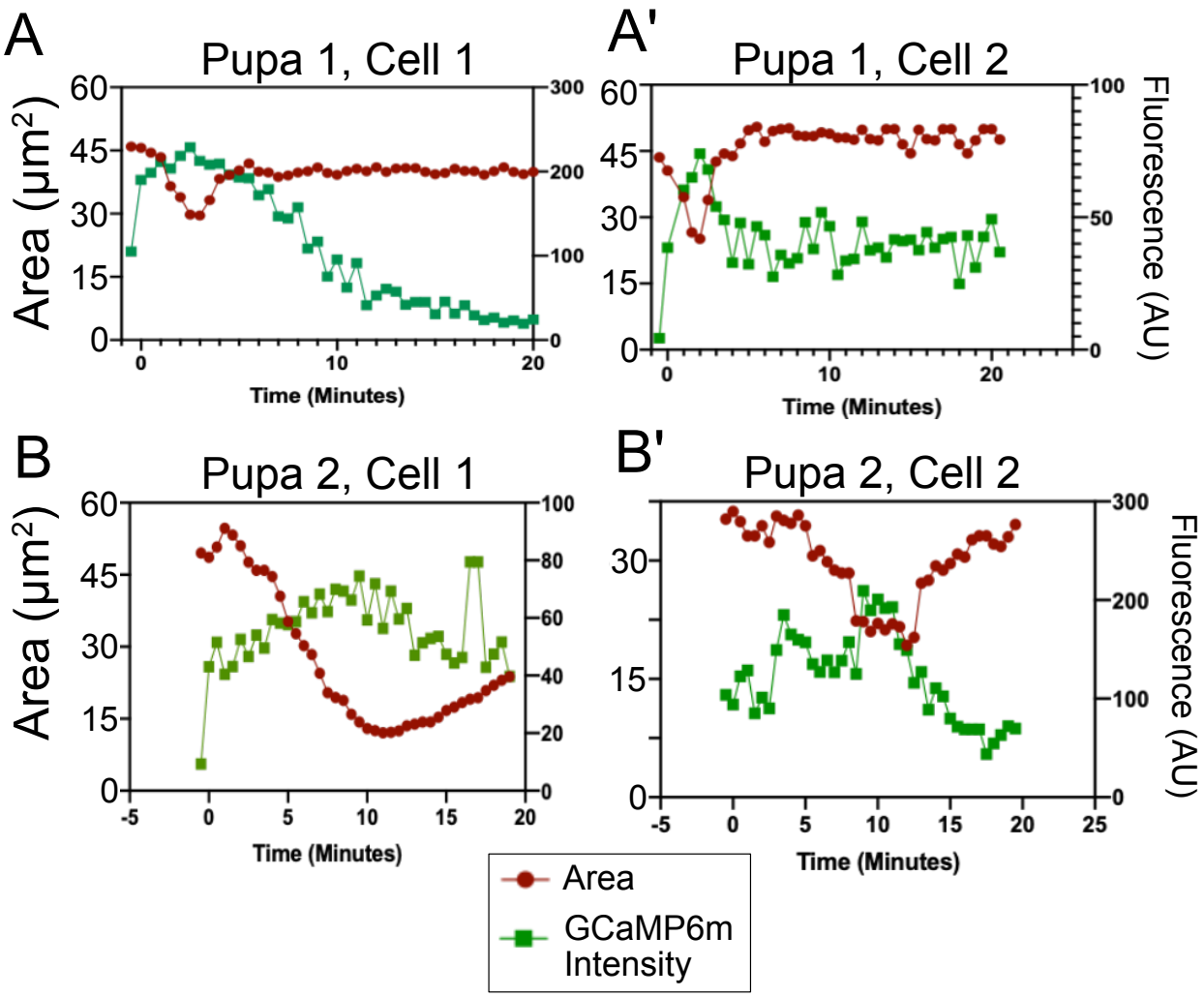

Chapter 6, Figure 3. Cell contraction occurs in tandem with increased calcium fluorescence.
(A–B) Cell contraction is depicted by the red lines following cell area, while calcium fluorescence is depicted by the green lines following GCaMP6m intensity of four cells following wounding in two pupae. In each case, cell area appears to conversely follow GCaMP6m intensity, showing the cell contraction events may be correlated with the calcium response after wounding. Figure courtesy of Page-McCaw Lab rotation student Lilia Merbouche.

CHAPTER 7

ADDITIONAL DOWNSTREAM WOUND RESPONSES

Introduction

This project also sought to explore other downstream cellular behaviors that aid in wound repair, beyond just changes in tension and cytoskeleton, and whether wound-induced calcium signaling is required for these behaviors to occur. To do this, we took a broader approach by observing animals throughout the entire repair process, and monitoring the distinctive cellular behaviors that occur during the wound closure process. The *Drosophila* pupa is especially useful for this task because it remains stationary for the entirety of its pupation, meaning the repair process can be captured on a microscope continuously for many hours (or even days) at a time.

Because wounding a tissue causes the destruction and death of dozens to hundreds of cells, the repair process requires the dead cells be replaced by new cells that are the product of increased proliferation and/or old cells migrating in to fill the void at the center of the wound. Previous studies have shown that epithelial cell migration occurs proximal to a wound, while proliferation is increased in cells distal from the wound[110]. Moreover, the wound response is not restricted to the epithelial sheet, but also requires other cells types such as immune cells (hemocytes and fat body cells in *Drosophila*) to fight potential infection, and macrophages (hemocytes in *Drosophila*) to clear debris from dead/dying cells[7,191]. Therefore, we studied the epithelial response to filling in the void of cell death, as well as the response of hemocytes and fat body cells.

Wounding induces cell cycle changes in cells proximal to the wound

To monitor epithelial nuclear migration and proliferation, we employed Fluorescent Ubiquitination-based Cell Cycle Indicators (FUCCI), comprised of E2F1-GFP and CycB-mRFP,

which are genetically expressed cell cycle indicators that allow for determination of whether a nucleus is in G1, S, G2, or M, based on the fluorescence (Chapter 7, Figure 1A, Zielke, et al. 2014[192]). Because both fluorophores are nuclear localized, we sought to use this system to track migration and proliferation after wounding. After wounding FUCCI pupae, we found nuclei proximal to the wound migrate inward to fill in the void, as expected. Interestingly, we found most of the nuclei around the wound margin began to simultaneously express both E2F1 and Cyclin B for the duration of repair (Chapter 7, Figure 1B). One potential reason is these cells are stalled in G2/M, either due to damage causing them to be unable to complete mitosis or through some signaling cascade leading them to deliberately delay cytokinesis. Another potential explanation is these nuclei undergo an altered cell cycle, such as endoreplication, whereby the nuclei replicate their cell cycle without going through cell division. This phenomenon has been seen by Vicki Losick[94,193], and while it appears to aid in wound repair[194], the exact role of wound-induced polyploidization is still being uncovered.

Multinucleate syncytial cells form after wounding

In order to better understand the cellular behaviors occurring around wounds, we used pupae expressing a green fluorescent cell border marker E-cadherin-GFP in tandem with the red fluorescent nuclear marker mCherry-NLS, in order to track both nuclei and cell borders. Rather than a simple increase in migration and proliferation, we observed a much more striking behavior that is less studied in the literature: multinucleate syncytia formation. Within two hours of wounding, many of the cells most proximal to the wound have become much larger and contain more than one nucleus (Chapter 7, Figure 2). Throughout the course of wound repair, some of the syncytial cells appear to progressively increase in size, eventually becoming as much as 50 times large by area than an average cell, with as many as 20 nuclei contained within a single cell, by six hours after wounding (Chapter 7, Figure 2). Furthermore, the number and size of syncytia per pupa was positively correlated with the size of the wound (Chapter 7, Figure 3).

In order to better understand syncytial cells after wounding, Page-McCaw Lab graduate student James White and Page-McCaw Lab undergraduate Jasmine Su have begun annotating movies of pupae during the repair process to accurately determine whether syncytia form through endomitosis, whereby the cell replicates and divides its nucleus but does not undergo cytokinesis, or cell-cell fusion whereby two cells fuse together to become a single larger cell[193,195,196]. If the syncytia form as a result of cell-cell fusions, they plan to assess the number of cell-cell fusions as a function of wound size, and whether the border breakdowns occur preferentially on the tangential borders or radial borders with respect to the wound. Radial borders separate cells in the same row with respect to distance from the wound while tangential borders separate cells in different rows back from the wound. If the tangential border between two cells breaks down (thus fusing a cell with a neighbor one row distal from the wound), then the syncytium would automatically form in a manner where it is elongated towards the direction of the wound. Forming syncytial cells in this manner could give two easily discernable benefits for wound repair. First, syncytial cells elongated towards the wound would immediately be polarized in the direction most conducive to migrating inwards to fill in the wound. Second, fusions between cells multiple rows back from the wound can allow for cellular resources, such as actin, to become aggregated at the wound margin, potentially facilitating pursestring and filopodia formation.

Immune cells infiltrate the wound site in a Gbp-independent manner

As previously mentioned, epithelia are not the only cells that respond to an injury. In *Drosophila*, hemocytes and fat body cells act like macrophages and immune cells to clear debris from the wound site and secrete antimicrobial peptides in response to a potential infection[197–200], and fat body cells specifically can act to plug the wound[138]. To better study this response, we wounded pupae expressing *srp-GMA*, which labels the actin of both hemocytes and fat body cells with GFP[201,202]. Interestingly, the immune response appears to be relatively sporadic, with some samples only having a very small number of srp-expressing cells

aggregating around the wound site at six hours after wounding, while other samples had significant immune cell infiltration after six hours. Another interesting finding was that some epithelial cells, labelled with p120ctn-TagRFP, also began to fluoresce with GFP (Chapter 7, Figure 4A). This shows that, not only do hemocytes and fat body cells express *srp* (Chapter 7, Figure 4B, C) some epithelia may also begin expressing *srp*, generally considered a transcription factor in mesodermal derived cells, possibly indicating the kind of transcriptional changes that begin to occur in certain epithelial cells around wounds. This possibility has not yet been fully explored.

Chapter 4 showed that the distal calcium expansion is sparked by proteases from the center of the wound activating the cytokines Growth-blocking peptides in the extracellular space. While Gbps were shown to trigger a calcium response on epithelial cells through Mthl10, these cytokines may also trigger an immune response, such as drawing the fat body cells or hemocytes to the wound. To determine whether Gbps play a role in this immune response, we wounded Δ*Gbp1,2* pupae expressing *srp-GMA* to determine whether these pupae had a reduced response. However, we found that Δ*Gbp1,2* pupae wounded under the same conditions had the same sporadic immune response as control pupae, with the exact same number of samples in both the control and Δ*Gbp1,2* group classified as having a “mild”, “moderate”, or “severe” infiltration of srp-expressing cells aggregating around the wound site at six hours (Chapter 7, Figure 5). Therefore, it does not appear that Gbp1 or Gbp2 have a clear role in recruiting immune cells to the site of pupal wounds.

CHAPTER 7 FIGURES

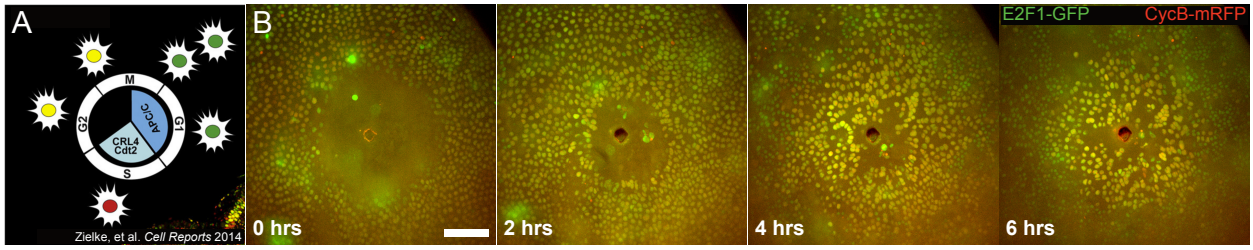

Chapter 7, Figure 1. Cells proximal to the wound preferentially enter G2/M phase of cell cycle during wound repair

(A) Schematic of the Fluorescence Ubiquitination-based Cell Cycle Indicator (FUCCI) system, from Zielke et al.[192] whereby E2F1-GFP and CycB-mRFP combine to indicate the cell cycle stage: green corresponds to G1, red corresponds to S, and yellow (green + red) corresponds to G2/M. (B) FUCCI is ubiquitously expressed in *Drosophila* pupae. Immediately after wounding, most epithelial cells in the notum are in G1. As repair occurs, the proximal cells progressively transition from green to yellow by 6 hours after wounding, where these cells remain generally without dividing, demonstrating either a pause in G2/M of cells proximal to the wound or a breakdown in the functionality of the FUCCI system as the proximal nuclei go through an altered cell cycle, such as endocycling. Scale bar = 50 μm. Figure made in collaboration with Page-McCaw lab graduate student James White.

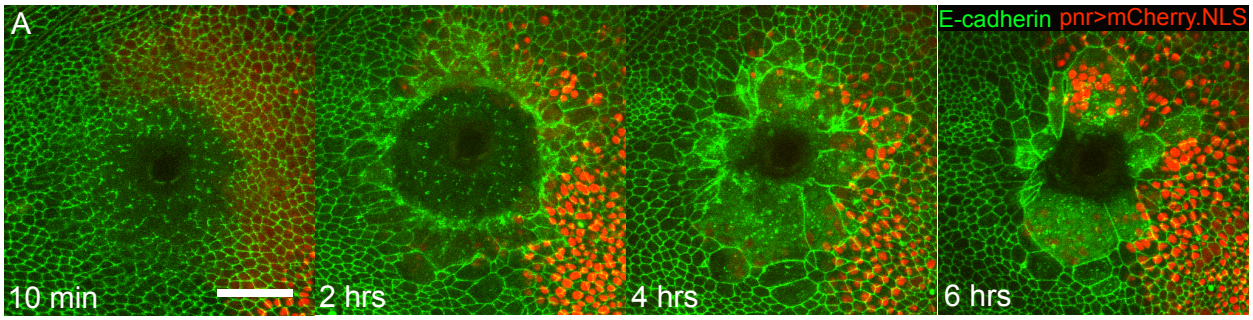

Chapter 7, Figure 2. Cells proximal to the wound undergo cell-cell fusions to become giant multinucleate syncytia.
(A) Ubiquitously expressed E-cadherin-GFP and *pnr* domain expressed mCherry.NLS. After wounding, cell-cell fusions occur in the cells most proximal to the wound margin, resulting in giant multinucleate syncytial cells. Scale bar = 50 μm.

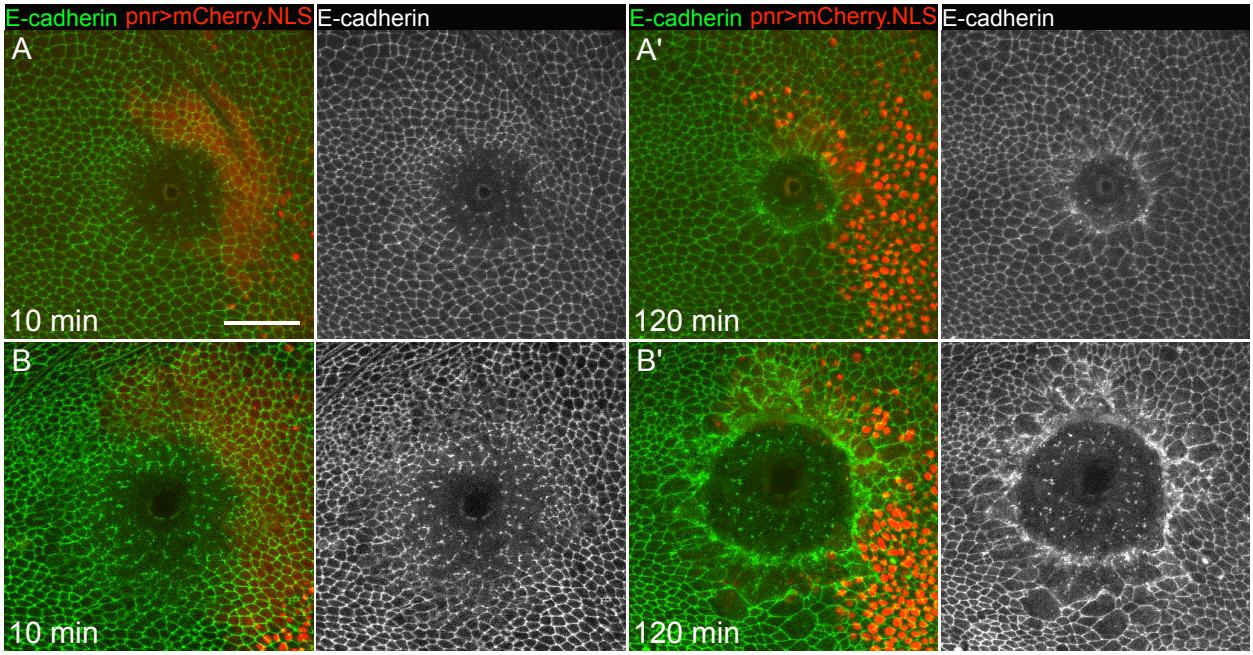

Chapter 7, Figure 3. Syncytia formation is increased in larger wounds.
(A–B) Ubiquitously expressed E-cadherin-GFP and *pnr* domain expressed mCherry.NLS. (A) After creating small wound, very few cell-cell fusions occur in the cells most proximal to the wound margin, resulting in only a small number of syncytial cells. (B) Larger wounds create larger and more numerous syncytia, already clearly visible 120 minutes after wounding. Scale bar = 50 µm.

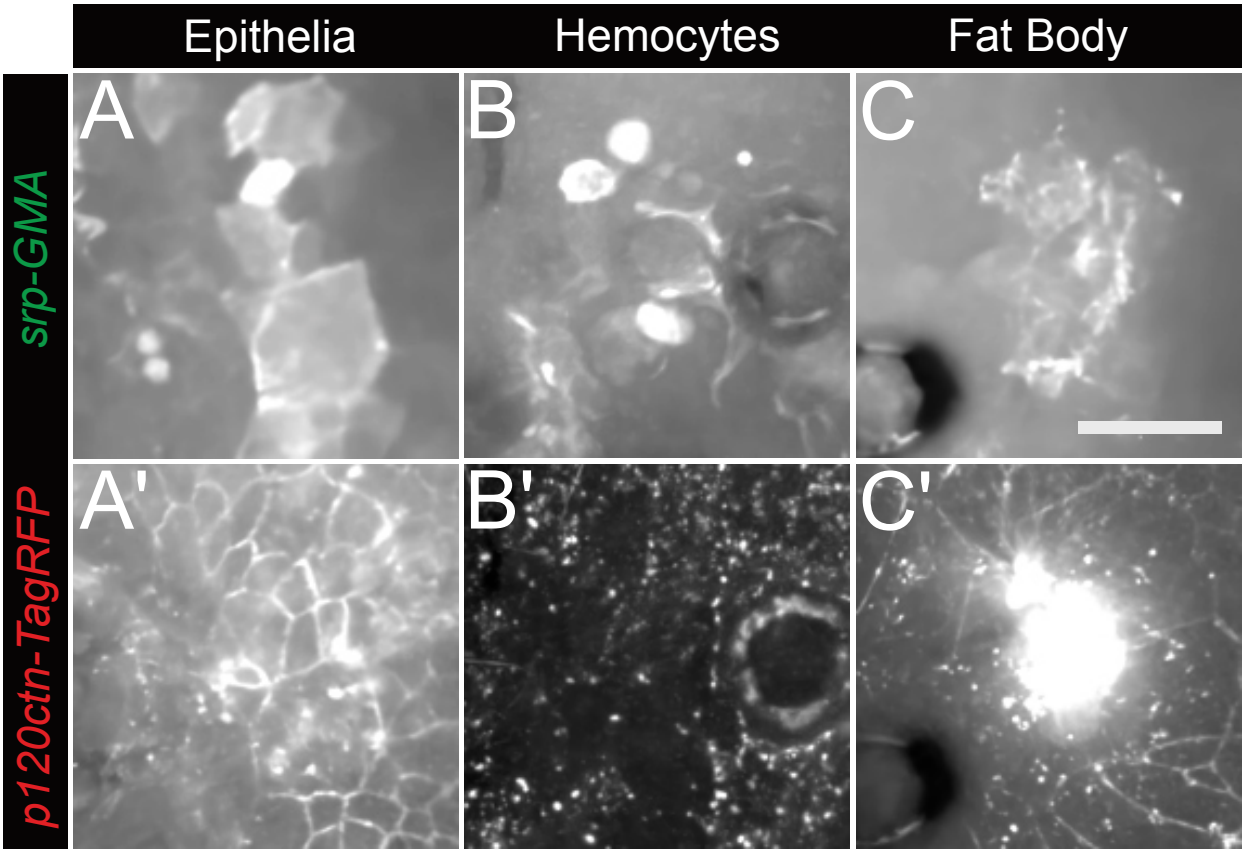

Chapter 7, Figure 4. Types of *srp*- expressing cells visible 6 hours after wounding. (A–C) Ubiquitously expressed *p120ctn-TagRFP* and *srp-GMA*, 6 hours after wounding. Three different *srp*- expressing cells are visible. Scale bar = 25 µm. (A) Some epithelial cells proximal to the wound (some of which are clearly syncytial cells) begin to express *srp-GMA.* (B) Round *srp*- expressing hemocytes, which do not express *p120ctn-TagRFP* (B'), cluster around the wound to clear debris and potentially respond to infection. (C) Large *srp*- expressing fat body cell, many of which highly express *p120ctn-TagRFP* (C'), cluster around the wound to potentially respond to infection.

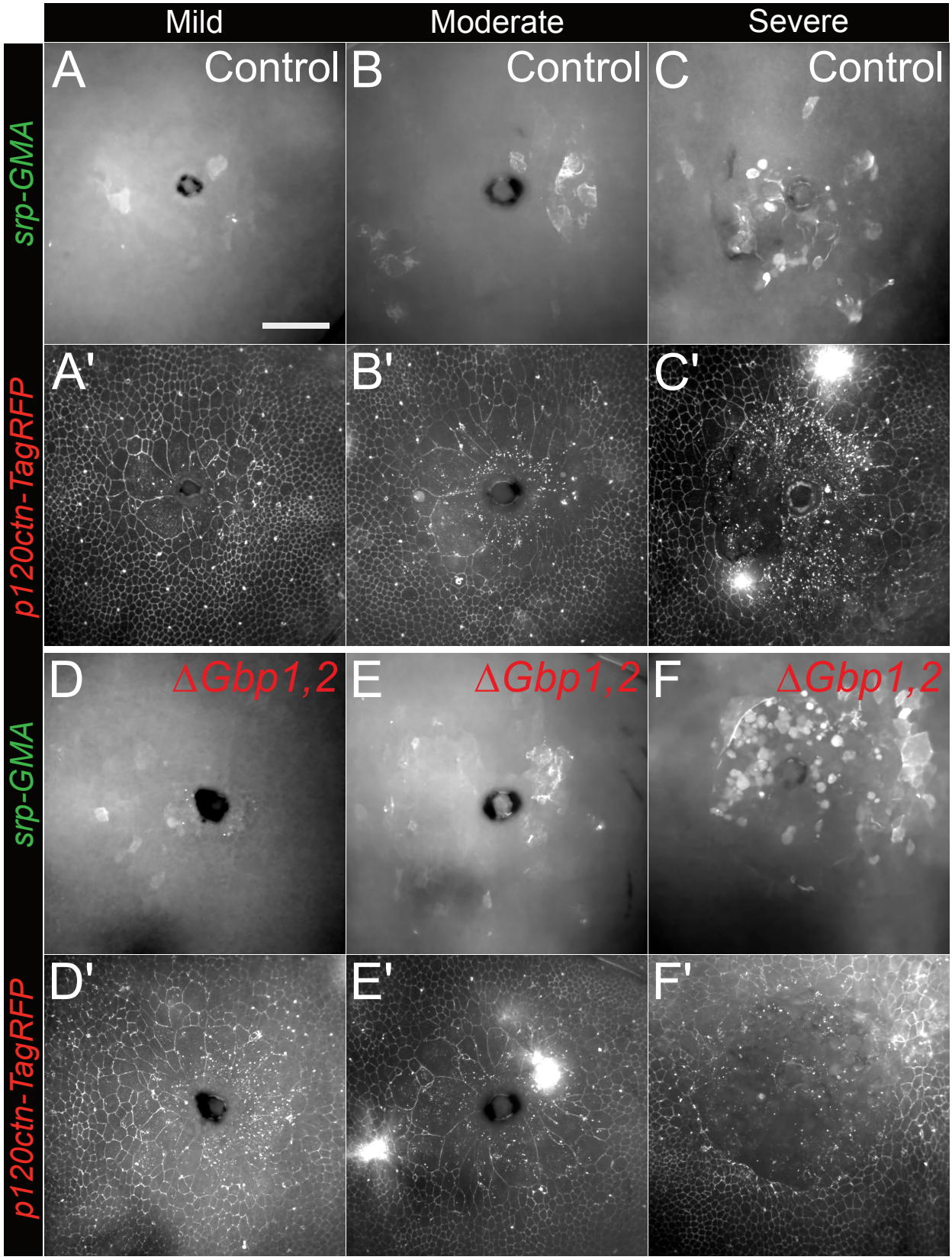

Chapter 7, Figure 5. Δ*Gbp1,2* does not noticeably affect the wound-induced immune response. (A–F) Ubiquitously expressed *srp-GMA* (A–F) and *p120ctn-TagRFP* (A'–F'), 6 hours

after wounding. Samples were monitored for immune response severity in control (A–C) or Δ*Gbp1,2* (D–F) pupae. Scale bar = 50 μm. (A, D) A representative control sample and a representative Δ*Gbp1,2* sample with relatively mild immune response. n = 2 of 7 for both control and Δ*Gbp1,2*. (B, E) A representative control sample and a representative Δ*Gbp1,2* sample with a relatively moderate immune response. n = 3 of 7 for both control and Δ*Gbp1,2.* (C, F) A representative control sample and a representative Δ*Gbp1,2* sample with relatively severe immune response. n = 2 of 7 for both control and Δ*Gbp1,2*. In both genotypes, the pupae with a severe immune response failed to close their wounds (C', F').

CHAPTER 8

DISCUSSION

Timeline of *Drosophila* Pupal Wound Responses

When the *Drosophila* pupal notum is wounded by pulsed-laser ablation, the laser superheats the focal point and ablates the tissue on the order of nanoseconds, converting the matter into a plasma and causing a cavitation bubble, which expands and contracts within microseconds, causing mechanical damage to the surrounding tissue[23,24,125,203]. The damage caused by the cavitation bubble is greatest at the focal point and lower farther from the center. As such, the damage is not uniform but variable within the cavitation footprint, leading to multiple distinct regions of cellular damage around a single pulsed-laser wound[118,136].

At the focal point, the laser pulses drive multiphoton ionization, plasma formation, molecular recombination that destroys biomolecules[134]. Just slightly further out, stresses from the rapidly expanding cavitation bubble and shock wave destroy macromolecular assemblies, which likely constitute the region of laser-induced rupture observed in Chapter 3[136]. Next is a distinct region of cell lysis, identified by the area that completely loses mCherry.NLS fluorescence in the minutes after wounding[113,136]. This is followed by a region of nuclear membrane damage identified by the cloud of mCherry.NLS that leaves the nuclear compartment and floods the cytoplasm when laser-induced stresses compromise nuclear membrane integrity (and likely other organelles at the same time)[136]. The final region of cellular damage is the zone of plasma membrane damage, where the mechanical shear force of the cavitation bubble rips the plasma membrane, identified through the immediate GCaMP fluorescence from extracellular calcium flooding into the cytoplasm[14,113,136].

The severity of damage is distinct in each of these regions, likely causing many of the regions to produce unique wound-induced signaling molecules and cellular responses. Although

the cells in the regions of laser-induced rupture and cell lysis have died, in their wake remains the initiating proteins that spark the wound-induced calcium response in distal cells: proteases[204]. These proteases will cleave pro-Gbp into its active form, which can then diffuse outward and bind to the cell surface GPCR Mthl10 to initiate the distal calcium response through the Gq-signaling cascade[113]. While this is occurring, most of the cells in the regions of nuclear membrane damage and plasma membrane damage will survive and participate in the wound response[136]. However, unlike the more distal cells, these proximal cells experience a unique wound environment, both due to these cells having to deal with their own cellular injury but also due to the initial influx of extracellular calcium that rushes into these cells[14,113,136]. Over the next ~15 seconds, this influx of extracellular calcium diffuses to ostensibly uninjured neighboring cells through gap junctions. Then, beginning ~45 seconds after wound, the Gbp/Mthl10-induced calcium response will begin releasing ER calcium in cells around the wound[113]. This distal calcium response continues outward, moving progressively more distally over the next minute or so before devolving into asymmetric stochastic flares for the next ~5-10 minutes. These calcium flares are junctionally connected, given the flares of each cell become uncoordinated with its neighbors in the absence of gap junctions[113]. A single "flare" comprises a cell oscillating between a state of high cytosolic calcium, after an IP_3-mediated ER calcium release, and low cytosolic calcium, after the calcium is pumped out into the extracellular space through PMCA or back into the ER through SERCA to reset the ER for a new IP_3-mediated release[38]. The duration of the flares depends on the amount of IP_3 remaining in the cell by the time the ER refractory period is finished and by the function of STIM and Orai to ensure the ER can get replenished with calcium.

These calcium signaling events inform the cells around the wound that damage has occurred, and begin to dramatically change the cellular behavior in response. Within the first few minutes, cells multiple rows back from the wound site begin to have visible changes in their cytoskeletal dynamics, as viewed with GFP-labelled myosin. Myosin-II-GFP that is usually

localized near the cell borders becomes relocalized to the cytosol/apical cortex, leading to a visible cell contraction phenotype that is correlated with the GCaMP6m intensity of the cell and travels in a distal-to-proximal manner from cell to cell towards the leading edge of the wound. Over the next ~15–45 minutes, actin and myosin begin to accumulate at the leading edge of the wound, forming a supracellular actomyosin pursestring that acts to cinch the wound closed over the course of ~6 hours for normal sized wounds in these studies.

As the wound is closing, the proximal cells become giant, multinucleate syncytial cells. There are two methods whereby this might occur: endomitosis whereby the cell replicates and divides its nucleus but does not undergo cytokinesis, or cell-cell fusion whereby two cells fuse together to become a single larger cell[193,195,196]. Current research in the Page-McCaw lab and Losick lab at Boston College seeks to determine the mechanisms and roles of syncytial cell formation around wounds. Additionally, through to the FUCCI system, we see an upregulation in E2F1 and Cyclin B in cells proximal to the wound, indicating these cells are either stalled in G2/M or undergoing an altered cell cycle to become polyploid[94,193,194].

In addition to the epithelial response, we also see an immune response by hemocytes and fat body cells, infiltrating the wound site. This is not a new finding[7,138,205]. However, the characterization of this response as highly variable in the pupal notum, with some wounds eliciting a very little small response from motile immune cell while other wounds elicit a very strong response, is quite interesting. Additionally, while calcium flashes were previously shown to orchestrate immune cell dynamics in *Drosophila* embryos[7], we find that Δ*Gbp1,2* do not appear to have an altered response in pupae, leading to the conclusion that the activation of Gbps around wounds, and the distal calcium response in general, is not required for immune cell infiltration to wounds. This does not preclude the initial influx and first expansion of calcium from being required, nor does is exclude the distal calcium response from playing a role in this behavior if the two calcium responses are redundant and either is sufficient. If experiments can eliminate all types of calcium signaling from pupal wounds, then this may be tested in the future.

Calcium signaling dynamics and roles

Calcium is an essential signaling ion, regulating a wide variety of cellular processes in every living organism[19,206,207]. Like sodium, potassium, and chloride, calcium ion concentration is tightly regulated by the cell[18,208]. Cytosolic calcium concentrations remain low, while a majority of calcium ions are actively maintained extracellularly or within organelles such as the endoplasmic reticulum[18,19]. The massive difference in concentration between cytosolic calcium and its stores under resting conditions, around four orders of magnitude difference, means that calcium signaling in the cytosol represents a massive change in the intracellular environment. Multiple cytosolic proteins are responsive to an increased concentration of calcium, such as calcineurin, which activates nuclear factor of activated T-cells (NFAT) to initiate an immune response through transcription of cytokines[209,210]; calmodulin, which activates a variety of other proteins including Myosin light chain kinase (MLCK) and Calcium/calmodulin-dependent protein kinase II (CaMKII) to phosphorylate numerous downstream targets[211,212]. In the wound response specifically, calcium is known to directly influence cytoskeletal dynamics[6,20,72], ROS production[7,11,74], $cPLA_2$ activation[8], and JNK signaling[96,191].

Calcium's spatiotemporal behavior in the cell is striking because it is oscillatory by nature[38,213,214]. Once a calcium release has occurred from the ER, calcium oscillations can occur because, after the calcium is pumped back into the ER through SERCA, sufficient levels of IP_3 may be present to stimulate another calcium release through IP_3R[38]. Additionally, the depletion of ER calcium may trigger STIM to activate Orai and allow "store-operated calcium entry" (SOCE) from the extracellular space[18,31]. Finally, an increase in cytosolic calcium can trigger "calcium-induced calcium release" (CICR) through the ryanodine receptor on the ER[38,48,49]. This means that the dynamics and responses of calcium signaling are based not only around the concentration of calcium in the cytosol, but also the duration and frequency of the recurring oscillations[18,19,213].

In response to wounding, this oscillatory behavior is seen in the stochastic flaring that occurs in the aftermath of the distal calcium response. Chapter 5 showed that disruption of SERCA, PMCA, or STIM can cause a significant change in the duration or frequency of the flaring response, changing the amount of time that calcium is in the cytosol of the cells around the wound. If future experiments uncover the role(s) of distal calcium response in repair after wounding, it will be interesting to see the effects of these proteins on the outcomes of repair. This would determine whether the distal calcium response alone is sufficient to activate the downstream wound response, or whether it requires a specific calcium signaling duration and frequency.

In a multicellular tissue such as the notum, these repeated oscillations travel from cell-to-cell in a wave-like manner because IP_3, and to a lesser extent calcium, can move through gap junctions[52–54], leading to a more coordinated response. Chapter 4 demonstrated that gap junction knockdown causes the initial calcium influx to be unable to spread and the distal calcium response and flares to appear speckled[113]; other studies have shown that impairment of gap junctions impairs calcium signaling[42,57,150] and potentially leads to disruption of coordinated cellular growth and survival[57,215].

Damage-induced activation of proteases

This project has characterized the distal calcium response, tracing the signaling cascade to the act of cellular destruction that occurs as a function of wounding. Simply lysing the cells at the middle of the wound and creating proteases sets in motion the process that leads to calcium release from the ER in cells at least 150 μm away from the wound. The protease-initiated model of wound detection varies from other models, where the ligand for a distal cell-surface GPCR is expected to be released by the lysed cell. Instead, the activation of fat body secreted pro-Gbp into its active form represents a different paradigm where the initiating ligand remains in the extracellular space until cell lysis causes it to activate. This could be evolutionarily

advantageous because it can allow for a system where only a single cell type needs to be responsible for producing and secreting a ligand for the wound response, and (in *Drosophila*) bathing all other cell types in a pro-ligand waiting for cell lysis to release protease into the extracellular space. Additionally, this gives a method for global systemic up/downregulation of the wound-sensitive signals so that the entire body can be prepared to respond to damage, rather than each cell or small group of tissues doing this independently. The finding that both serine and cysteine proteases can activate pro-Gbp lends credence to the idea that any of a variety of non-specific proteases released from destroyed cells might be sufficient to trigger the distal calcium response.

Proteolytic activation of proteins in response to damage or pathogens has been well documented in multiple organisms and cellular pathways. In the *Drosophila* Toll pathway, pro-Spatzle is cleaved into its active form in response to pathogens[99–101]. In the pyroptosis pathway, damage leads to the activation of the cysteine protease caspase-1, which cleaves the cytokines IL-1β and IL-18 into their active form to initiate an inflammatory response[177–179]. In the vertebrate blood coagulation, a cascade of proteases activating other proteases, such as pro-thrombin activation into thrombin, which then cleaves fibrinogen into fibrin, is vital for proper response to vascular injury[106–108]. In the blood coagulation pathway specifically, damage to the epithelia is repaired in part thanks to the proteolytic system based around proteins and cells found in the circulatory system that actively migrate through the body and bathe other cell types. While *Drosophila* have an open circulatory system, the hemocytes and fat cells roving throughout the hemolymph may represent an evolutionary precursor to the roving cells in vertebrates that respond to damage and pathogens[197,199,200]. Furthermore, previous studies have yielded results that support the notion of proteolytic activation in the immediate response to wounds. Wounds accompanied by serine protease application enhanced expression of a variety of wound response[102,103]. In plants, the immunomodulatory plant elicitor peptide and defense hormone systemin are each cleaved from their pro- forms into their active forms by proteases in response

to damage or predation[144,180]. The use of proteases as a wound response strategy is therefore not specific to *Drosophila*, and suggests that wound detection based on pro-protein cleavage may in fact be an evolutionarily conserved mechanism.

Comparisons to human wound repair

Although there are no known vertebrate homologues for the identified GPCR Mthl10 or chemokine ligands Gbp1 and Gbp2, there is reason to hypothesize that a similar mechanism for wound detection through proteases could be conserved between insects and humans given the universality of proteases in damage responses, and the presence of numerous GPCRs and chemokines in vertebrates. Interestingly, there is some sequence similarity between Drosophila Gbp1 and human β-defensin 2, which acts as a cytokine-responsive antimicrobial peptide in humans[154,216], which may indicate some level of conservation of the Gbp proteins. Regardless, while there is enormous diversity in GPCR ectodomains and ligands, there is considerable conservation of the GPCR interactions with G-proteins and the G-protein signaling cascades themselves, leading to similarities in the downstream pathways that result from GPCR activation[154,217]. The wound response in human skin involves numerous different cell types from the integumentary, circulatory, and immune systems coordinating together[4,5,104,105], while the wound response in the *Drosophila* notum appears to mostly involve three major cell types (epithelia, hemocytes, and fat body cells)[6,7,138]. However, it is important to realize how many important behaviors observed in *Drosophila* wound repair are conserved in humans: epithelial increase in cytosolic calcium, ROS creation, reorganization of cytoskeleton, epithelial migration, cytokine signaling, immune cell infiltration, and phagocytosis of debris[6,7,11,12,113,191,218]. Thus, even without human homologs of Gbp or Mthl10, the roles observed in the *Drosophila* wound response downstream of the Gbp/Mthl10-induced distal calcium response will likely be similar to the roles of human wound induced GPCR-mediated calcium responses. Therefore, the results of these studies have a substantial impact on the characterization of wound signaling and

damage responses that are present not only in *Drosophila*, but that are shared across the animal kingdom.

Summary and future studies

This project allowed us to study the wound response in a powerful model organism that is easy to genetically manipulate, wound, and monitor *in vivo*. By using this system, we have uncovered the molecular mechanisms of calcium signaling in the early response to epithelial wounds in the *Drosophila* pupa. This project has characterized two distinct calcium responses: one occurring due to extracellular calcium entry through plasma membrane damage followed by gap junction-mediated calcium diffusion to neighboring cells, and another occurring due to proteolytic cleavage of Gbp cytokines binding to the GPCR Mthl10 on distal cells to initiate IP_3-mediated ER calcium release through the Gq-signaling pathway. The fact that *Drosophila* has only ~200 GPCRs while humans have ~800 (about half of each being gustatory or olfactory)[151] and that the Drosophila community has created an easily usable expression system with publicly available knockdown lines[111], was crucial for making these discoveries. Additionally, the ability to use the *Drosophila* pupa to live image multicellular wound responses for multiple hours means this system will continue to be useful in determining the mechanisms of wound repair and the downstream role(s) of the Gbp/Mthl10 pathway. Furthermore, because the Gbp/Mthl10 pathway has already been characterized to elicit the distal calcium response, future studies will be able to compare control pupae to knockdown/knockout pupae to probe whether specific cellular wound responses require the distal calcium response. This was already done for immune cell infiltration, and although there was no identifiable difference, it can easily be done for other wound responses of interest, such as syncytia formation or cytoskeletal remodeling; do these occur in a Gbp/Mthl10-dependent manner? Unanswered questions about the nature of wound repair continue to be asked by Page-McCaw lab students James White, Ivy Han, and Jasmine Su, who are working to discover the processes that drive wound-induced syncytia

formation and cytoskeletal remodeling (whether they are downstream of the distal calcium response or not), and to determine their role in the eventual repair of wounds. These projects will continue to work towards the goal of completely characterizing the mechanisms that are essential for damage-induced cell signaling and proper wound repair.

Materials and Methods

Drosophila melanogaster husbandry

The *Drosophila* lines used for these studies are detailed in Table S1. The complete genotype for each figure panel is provided in Table S2. *Drosophila* were maintained on standard cornmeal-molasses media supplemented with dry yeast. With the exception of flies containing *Gal80*^{TS}, flies were housed in plastic tubes in incubators between 18˚C–25˚C.

Fly crosses where the progeny will express Gal80^{TS} were maintained at 18°C for 2 days to inhibit Gal4 activation during embryogenesis. Progeny were then incubated at 29°C to activate Gal4, where they remained until experimentation. Thus, 3rd instar larvae were incubated at 29°C for 3-4 days before wing disc dissections and pupae were incubated at 29°C for 4-5 days before wounding.

Table 1: Source flies obtained for these studies.

Fly lines:	**Complete genotype of source flies:**
"ActinP-GCaMP6m"	*w[1118]; P{w[+mC]=ActinP-GCaMP6m}attp40* (O'Connor et. al Dev Cell 2021)[113]
"pnr-Gal4"	*P{w[+mC]=UAS-Dcr-2.D}1, w[1118]; P{w[+mW.hs]=GawB}pnr[MD237]/TM3, Ser[1]* (FlyBase ID: FBst0025758)
"UAS-mCherry.NLS"	*w[*]; P{w[+mC]=UAS-mCherry.NLS}3* (FlyBase ID: FBst0038424)
"tubP-Gal80^{TS}"	*w[*]; P{w[+mC]=tubP-GAL80[ts]}2/TM2* (FlyBase ID: FBst0007017)
"UAS-GCaMP6m"	*w[1118]; P{y[+t7.7] w[+mC]=20XUAS-IVS-GCaMP6m}attP40* (FlyBase ID: FBst0042748)
"tubP-Gal4"	*y[1] w[*]; P{w[+mC]=tubP-GAL4}LL7/TM3, Sb[1] Ser[1]* (FlyBase ID: FBst0005138)
"UAS-Inx2 RNAi"	*y[1] v[1]; P{y[+t7.7] v[+t1.8]=TRiP.JF02446}attP2* (FlyBase ID: FBst0029306)
"UAS-IP$_3$ sponge"	*UAS-IP3-m49 sponge* (on 3rd) [219] The *UAS-IP3-m49 sponge* line was obtained as a gift from Eric Baehrecke Lab, (University of Massachusetts Medical School, Worcester, MA)
"UAS-IP$_3$R RNAi#1"	*y[1] v[1]; P{y[+t7.7] v[+t1.8]=TRiP.JF01957}attP2* (FlyBase ID: FBst0025937)
"UAS-IP$_3$R RNAi#2"	*UAS-itpr RNAi (no. 1063R-1,* National Institute of Genetics, Japan)

"UAS-Plc21C RNAi#1"	*y[1] sc[*] v[1] sev[21]; P{y[+t7.7] v[+t1.8]=TRiP.HMS00600}attP2* (FlyBase ID: FBst0033719)
"UAS-Plc21C RNAi#2"	*y[1] v[1]; P{y[+t7.7] v[+t1.8]=TRiP.JF01211}attP2* (FlyBase ID: FBst0031270)
"UAS-Gαq RNAi#1"	*y[1] v[1]; P{y[+t7.7] v[+t1.8]=TRiP.JF01209}attP2/TM3, Ser[1]* (FlyBase ID: FBst0031268)
"UAS- Gαq RNAi#2"	*y[1] v[1]; P{y[+t7.7] v[+t1.8]=TRiP.JF02464}attP2* (FlyBase ID: FBst0033765)
"UAS-mthl10 RNAi#1"	*y[1] v[1]; P{y[+t7.7] v[+t1.8]=TRiP.HMJ23672}attP40/CyO* (FlyBase ID: FBst0062315)
"UAS-mthl10 RNAi#2"	*y[1] v[1]; P{y[+t7.7] v[+t1.8]=TRiP.HMC03304}attP2* (FlyBase ID: FBst0051753)
"UAS-AdoR RNAi"	*y[1] sc[*] v[1] sev[21]; P{y[+t7.7] v[+t1.8]=TRiP.HMC03684}attP2* (FlyBase ID: FBst0056866)
"UAS-Tre1 RNAi"	*y[1] v[1]; P{y[+t7.7] v[+t1.8]=TRiP.JF02751}attP2* (FlyBase ID: FBst0027672)
"UAS-TkR86C RNAi"	*y[1] v[1]; P{y[+t7.7] v[+t1.8]=TRiP.JF02160}attP2* (FlyBase ID: FBst0031884)
"UAS-Trpm RNAi#1"	*y[1] v[1]; P{y[+t7.7] v[+t1.8]=TRiP.JF01236}attP2* (FlyBase ID: FBst0031291)
"UAS-Trpm RNAi#2"	*y[1] v[1]; P{y[+t7.7] v[+t1.8]=TRiP.JF01465}attP2* (FlyBase ID: FBst0031672)
"ΔGbp1,2"	*Df(2R)Gbp-ex67* [160] *(obtained as a gift from Takashi Koyama, (IGC, Lisbon, Portugal))*
"Gbp1$^{\Delta}$"	*w[1118]; Gbp1$^{\Delta}$*
"Gbp2$^{3\Delta FS}$"	*w[1118]; Gbp2$^{3\Delta FS}$*
"*vas-Cas9"*	*w[1118]; PBac{y[+mDint2]=vas-Cas9}VK00027 (FlyBase ID: FBst0051324)*
"His2Av-EGFP"	*w[*]; P{w[+mC]=His2Av-EGFP.C}2/SM6a (FlyBase ID: FBst0024163)*
"His2Av-mRFP"	*w[*]; P{w[+mC]=His2Av-mRFP1}II.2 (FlyBase ID: FBst0023651)*
"Ecadherin-GFP"	*P{Ubi-p63E-shg.GFP} (FlyBase ID: FBti0151829)*
"p120ctn-TagRFP"	y; ubiP- p120ctn-TagRFP (obtained as a gift from Shigeo Hayashi)[220]
"Zip-GFP"	w[*]; P{w[+mC]=PTT-GC}zip[CC01626]/SM6a *(FlyBase ID: FBst0051564)*
"srp-GMA"	obtained as a gift from Brian Stramer, originally from [202]
"UAS-FUCCI"	w[1118]; P{w[+mC]=UAS-GFP.E2f1.1-230}32 P{w[+mC]=UAS-mRFP1.NLS.CycB.1-266}19/CyO, P{ry[+t7.2]=en1}wg[en11]; MKRS/TM6B, Tb[1] *(FlyBase ID: FBst0055121)*
"UAS-PLC21C"	P{XP}Plc21C^{d11193} *(FlyBase ID: FBti0057244)*
"UAS-sqh^{EE}"	*w[*]; P{w[+mC]=UASp-sqh.E20E21}3 (FlyBase ID: FBst0064411)*
"UAS-SERCA RNAi"	*y[1] v[1]; P{y[+t7.7] v[+t1.8]=TRiP.JF01948}attP2 (FlyBase ID: FBst0025928)*
"UAS-PMCA RNAi"	*y[1] v[1]; P{y[+t7.7] v[+t1.8]=TRiP.JF01145}attP2 (FlyBase ID: FBst0031572)*
"UAS-STIM RNAi"	*y[1] v[1]; P{y[+t7.7] v[+t1.8]=TRiP.JF02567}attP2 (FlyBase ID: FBst0027263)*
"UAS-Piezo RNAi"	*w[1118]; P{GD993}v2796 (FlyBase ID: FBst0457216)*

Table 2: Complete genotype for each figure panel.

Figure	Full Genotype of Sample
C2, F1	*ActinP-GCaMP6m / + ; pnr-Gal4, UAS-mCherry.NLS, tubP-Gal80^{TS} / +*
C3, F2, 5	*ActinP-GCaMP6m / + ; pnr-Gal4, UAS-mCherry.NLS, tubP-Gal80^{TS} / +*
C3, F3	*His2Av-EGFP / CyO ; pnr-Gal4, UAS-mCherry.NLS, tubP-Gal80^{ts} / TM3*
C3, F4, S1, S2	*Ecadherin-GFP / CyO; pnr-Gal4, UAS-mCherry.NLS, tubP-Gal80^{ts} / TM3*
C4, F1A'	*pnr-Gal4, UAS-mCherry.NLS, tubP-Gal80^{TS} / +*
C4, F1B-D, 7H, Movie S1	*ActinP-GCaMP6m / + ; pnr-Gal4, UAS-mCherry.NLS, tubP-Gal80^{TS} / +*
C4, F1E, Movie S2 (left)	*ActinP-GCaMP6m / + ; pnr-Gal4, UAS-mCherry.NLS, tubP-Gal80^{TS} / UAS-IP$_3$R RNAi #1*
C4, F1F, Movie S2 (middle)	*ActinP-GCaMP6m / + ; pnr-Gal4, UAS-mCherry.NLS, tubP-Gal80^{TS} / UAS-Plc21C RNAi #1*
C4, F1G-H, Movie S2 (right), Movie S4	*ActinP-GCaMP6m / + ; pnr-Gal4, UAS-mCherry.NLS, tubP-Gal80^{TS} / UAS-Gαq RNAi #1*
C4, F2A	*ActinP-GCaMP6m / + ; pnr-Gal4, UAS-mCherry.NLS, tubP-Gal80^{TS} / UAS-Trpm RNAi #2*
C4, F2B	*ActinP-GCaMP6m / + ; pnr-Gal4, UAS-mCherry.NLS, tubP-Gal80^{TS} / UAS-AdoR RNAi*
C4, F2C, 8B, Movie S5	*ActinP-GCaMP6m / UAS-Mthl10 RNAi #1 ; pnr-Gal4, UAS-mCherry.NLS, tubP-Gal80^{TS} / +*
C4, F3B, 8D-F (+/+)	*ActinP-GCaMP6m / ActinP-GCaMP6m*
C4, F3C	*ActinP-GCaMP6m, Gbp1$^{\Delta}$ / ActinP-GCaMP6m, Gbp1$^{\Delta}$*
C4, F3D	*ActinP-GCaMP6m, Gbp2$^{3\Delta FS}$ / ActinP-GCaMP6m, Gbp2$^{3\Delta FS}$*
C4, F3E	*ActinP-GCaMP6m, ΔGbp1,2 / ActinP-GCaMP6m, ΔGbp1,2*
C4, F4A-B, S2	*ActinP-GCaMP6m / CyO*
C4, F4C-D, F-G Movie S6, Movie S7	*UAS-GCaMP6m / + ; tubP-Gal4, tubP-Gal80^{TS} / UAS-mCherry.NLS* (White) *UAS-GCaMP6m / UAS-Mthl10 RNAi #1 ; tubP-Gal4, tubP-Gal80^{TS} / +* (Red)
C4, F5A-F, Movie S8	*UAS-GCaMP6m / + ; tubP-Gal4, tubP-Gal80^{TS} / UAS-mCherry.NLS* (White) *ActinP-GCaMP6m, ΔGbp1,2 / ActinP-GCaMP6m, ΔGbp1,2* (Red)
C4, F7D-F	*ActinP-GCaMP6m, ΔGbp1,2 / ActinP-GCaMP6m, Gbp1$^{\Delta}$*

C4, F7D-F	*ActinP-GCaMP6m, ΔGbp1,2 / ActinP-GCaMP6m, Gbp2$^{3\Delta FS}$*
C4, FS1A	*ActinP-GCaMP6m / + ; pnr-Gal4, UAS-mCherry.NLS, tubP-Gal80^{TS} / UAS-Inx2 RNAi #1*
C4, FS1B	*ActinP-GCaMP6m / + ; pnr-Gal4, UAS-mCherry.NLS, tubP-Gal80^{TS} / UAS-IP$_3$ sponge*
C4, Movie S3 (left)	*UAS-GCaMP6m / + ; pnr-Gal4, UAS-mCherry.NLS, tubP-Gal80^{TS} / +*
C4, Movie S3 (middle)	*UAS-GCaMP6m / + ; pnr-Gal4, UAS-mCherry.NLS, tubP-Gal80^{TS} / UAS-Inx2 RNAi #1*
C4, Movie S3 (right)	*UAS-GCaMP6m / + ; pnr-Gal4, UAS-mCherry.NLS, tubP-Gal80^{TS} / UAS-Gaq RNAi #1*
C5, F1	*ActinP-GCaMP6m / + ; pnr-Gal4, UAS-mCherry.NLS, tubP-Gal80^{TS} / UAS-SERCA RNAi*
C5, F2A	*ActinP-GCaMP6m / + ; pnr-Gal4, UAS-mCherry.NLS, tubP-Gal80^{TS} / UAS-PLC21C*
C5, F2B	*ActinP-GCaMP6m / + ; pnr-Gal4, UAS-mCherry.NLS, tubP-Gal80^{TS} / UAS-PMCA RNAi*
C5, F2C	*ActinP-GCaMP6m / + ; pnr-Gal4, UAS-mCherry.NLS, tubP-Gal80^{TS} / UAS-STIM RNAi*
C5, F2D	*ActinP-GCaMP6m / + ; pnr-Gal4, UAS-mCherry.NLS, tubP-Gal80^{TS} / UAS-Piezo RNAi*
C5, F3A	*ActinP-GCaMP6m / + ; pnr-Gal4, UAS-mCherry.NLS, tubP-Gal80^{TS} / UAS-SqhEE*
C6, F1A, 2	*Myosin-II-GFP / HisRFP*
C6, F1B	*Myosin-II-GFP, ΔGbp1,2 / HisRFP, ΔGbp1,2*
C6, F3	*ActinP-GCaMP6m / p120ctn-TagRFP*
C7, F1	*UAS-FUCCI / + ; pnr-Gal4, UAS-mCherry.NLS, tubP-Gal80^{TS} / +*
C7, F2, 3	*Ecadherin-GFP / CyO; pnr-Gal4, UAS-mCherry.NLS, tubP-Gal80^{ts} / TM3*
C7, F4, 5A-C	*srp-GMA / p120ctn-TagRFP*
C7, F5D-E	*srp-GMA, ΔGbo1,2 / p120ctn-TagRFP, ΔGbp1,2*

Drosophila **extract preparation**

Fly and larval extract was made following a protocol adapted from [221] and [222]. Briefly, 100 healthy adult flies with a female:male ratio of 3:1 or 100 healthy 3rd instar larvae, from non-overcrowded bottles, were homogenized in 750 µl of Schneider's *Drosophila* media (Thermo Fisher, #21720024). The resulting homogenates were centrifuged at 4°C for 20 minutes at 2600*g*. The supernatant was heat treated at 60°C for 5 minutes, before a second centrifugation at 4°C for 90 minutes at 2600*g*. The resulting supernatant – considered 100% extract – was aliquoted and stored at -20°C.

METHOD DETAILS

Pupal mounting

The protocol for pupal mount is detailed in Chapter 2. Briefly, white prepupae were identified and aged for 12-18 hours After Puparium Formation (APF) at 29°C. Each pupa was placed ventral side down on a piece of double-sided tape (Scotch brand, catalog #665) adhered to a microscope slide, and the anterior pupal case was removed with fine tipped forceps to reveal the head and thorax (as in Chapter 4, Figure 1A). The entire piece of double-sided tape (with dissected pupa) was gently lifted off the microscope slide and adhered to a 35 mm x 50 mm coverslip (Fisherbrand, cat#125485R) so the pupa is laid against the coverslip notum-side down, with the pupa sandwiched between the coverslip and the tape layer. Then, an oxygen permeable membrane (YSI, standard membrane kit, cat#1329882) was applied over the pupa and secured to the coverslip with additional double-sided tape so the pupa would not become dehydrated or deprived of oxygen.

Pupal survival

When mounted as described above, pupae developed normally for the next 3-4 days until eclosion, whereupon the adult flies crawled out of their cases and became stuck on the double-sided tape a few inches away. Pupal survival was measured as whether a pupa had developed into an adult fly and emerged from its case in this manner within 7 days after wounding (to ensure a pupa delayed in development was not accidentally miscounted as dead). Slides of pupae were returned to 29°C during this recovery phase after wounding to maintain Gal4 activation.

Live imaging

Live imaging of pupae was performed using a Zeiss (Oberkochen, Germany) LSM410 raster-scanning inverted confocal microscope with a 63X 1.4NA or 40X 1.3 NA oil-immersion objective. Raster-scans were performed with a 2.26 s scan time per image with no interval

between scans. Live imaging of wing discs was performed on the same scope, with the confocal settings turned off to maximize imaging depth, using a 25X 0.8 NA air objective. Raster-scans were performed with a 2.26 s scan time per image with a 15 s interval between scans. Notum picture in Fig. 1A' was taken on the same scope at 10X 0.50 NA air objective.

All images are single optical slices in the z-plane of greatest signal clarity, with the exception of Ecadherin-GFP images collected for Chapter 3, Figure 4, Chapter 6 Figures 1, 2, and Chapter 7 Figures 1, 4, and 5 which were Maximum Intensity Projections. All radial calcium analysis was performed on single optical slices.

Images collected specifically for Chapter 4, Figure 7C–F, Chapter 6 Figures 1, 2, and Chapter 7 Figures 1, 4, 5 were captured on a Nikon Ti2 Eclipse with X-light V2 spinning disc (Nikon, Tokyo, Japan) with a 40X 1.3 NA oil-immersion objective.

Laser ablation

Laser ablation was performed using single pulses of the 3rd harmonic (355 nm) of a Q-switched Nd:YAG laser (5 ns pulse-width, Continuum Minilite II, Santa Clara, CA). Laser pulse energies were on the order of 1 μJ, but were varied day to day and based on focal plane of ablation in order to optimize consistent wound sizes. A separate computer-controlled mirror and custom ImageJ plug-in were used to aim and operate the ablation laser so that ablation could be performed without any interruption to live imaging. The frame during ablation was retroactively considered t = 0 s.

Puncture wounding

Multiple pupae were placed on a piece of double-sided tape (Scotch brand, catalog #665), ventral side down on a microscope slide, and each anterior pupal case was removed with fine tipped forceps to reveal the notum epithelium (as in Chapter 4, Figure 1A). The slide was mounted on the stage of an upright epifluorescence microscope (Zeiss Axio M2) and imaged with a 1 s interval on a 5x objective (Zeiss EC Plan-NEOFLUAR 420330-9901). Pupae expressing GCaMP6m were manually punctured with an electrolytically sharpened tungsten

needle (Fine Science Tools, No:10130) while imaging. The frame when the puncture occurred was retroactively considered t = 0 s. Unfortunately, many puncture wounds resulted in a bubble of hemolymph that pooled over the wound, obscuring the initial influx and first expansion from multiple samples. However, the distal calcium response was always speckled in gap-junction knockdowns and always absent in G_q-pathway knockdowns, recapitulating laser wounds.

Wing disc mounting

Wing discs from 3rd instar larvae were dissected in Schneider's *Drosophila* media (Gibco, Life Technologies, Ref:21720-024) and immediately mounted in a small bubble of Schneider's *Drosophila* media on coverslips (Fisherbrand, cat#125485R) for imaging. A pap pen (RPI, catalog #50-550-221) was used to trace a hydrophobic barrier around the wing discs on the coverslip. Two wing discs, control and experimental, were mounted side-by-side in the same media bubble. The control disc was identifiable by the presence of mCherry which was not present in the experimental disc. Images were taken to establish a baseline of GCaMP fluorescence, and then potential calcium activators were pipetted directly into the media bubble over the wing discs. The concentration of calcium activators in the text refers to the final concentration after addition to the media bubble. The image taken during pipetting was retroactively considered t = 0 s.

Protease inhibition experiments

To test whether Δ*Gbp1,2* Larval Extract elicits a calcium response in control wing discs via proteases, we pre-mixed protease inhibitor cocktails or vehicle-only controls either into the extract or media bubble before addition to the wing disc. Specifically, we used 1) Cell Signaling Technologies Protease inhibitor cocktail (Cell Signaling Technology, #5871S), which had no effect on the extract-mediated calcium response of Δ*Gbp1,2* Larval Extract when mixed at or below the 2x recommended concentration; at 3x recommended concentrations, the inhibitor itself elicited an ectopic calcium response on the discs, making it unusable for properly testing the extract-mediated calcium response. 2) MS-Safe Protease and Phosphatase inhibitor

(Millipore Sigma, MSSAFE), which had no effect on the extract-mediated calcium response of Δ*Gbp1,2* Larval Extract when mixed at or below the 1x recommended concentration; at 1.5x recommended concentrations, the inhibitor itself elicited an ectopic calcium response on the discs, making it unusable for properly testing the extract-mediated calcium response. 3) Two other protease inhibitors tested (Millipore Sigma, 539134 and Millipore Sigma, 539133) used DMSO as a vehicle, which itself induces an ectopic calcium response in wing discs at even small concentrations (1% final v/v). Therefore, both of these protease inhibitors were not usable for properly testing the extract-mediated calcium response.

Peptide synthesis

The amino acid sequence for Growth-blocking peptides 1–5 is shown below [155].

Gbp1 (CG15917): ILLETTQKCKPGFELFGKRCRKPA

Gbp2 (CG11395): SLFNLDPKCAEGLKLMAGRCRKEA

Gbp3 (CG17244): MVAMIDFPCQPGYLPDHRGRCREIW

Gbp4 (CG12517): ILLDTSRKCRPGLELFGVRCRRRA

Gbp5 (CG14069): MLLEIQKRCWAGWGLLAGRCRKLA

These sequences were sent to Genscript (Piscataway, NJ. USA) for peptide synthesis under conditions to maintain the disulfide bond. The lyophilized peptide was reconstituted in ultrapure water, diluted to a concentration of 0.1 μM, aliquoted, and frozen at -80°C.

Protease preparation

Cysteine protease Clostripain (Alfa Aesar, Thermo Fisher, Stock: J61362) was reconstituted in a TBS solution (10 mM Tris, 1 mM $CaCl_2$, 50 mM NaCl, 2.5 mM beta-mercaptoethanol) to a final concentration of 1mg/mL (18.9 μM). This was aliquoted and frozen at -20°C. Serine protease trypsin (Gibco, Life Technologies, Ref: 25300-054) arrived at a concentration of 0.05% w/v (21.4 μM) and was refrigerated at 4°C.

***ActinP-GCaMP6m* generation**

pBPw.Act5CP-GCaMP6m was generated from the GCaMP6m plasmid pGP-CMV-GCaMP6m (Addgene, originally in [223]) and the Actin5c promoter [224]. Importantly, this construct features the full 4.4 Kb genomic enhancer sequence for actin, containing all the regulatory elements to drive ubiquitous expression, rather than the more commonly used 2.6 Kb actin promoter sequence which is not highly expressed in the pupal notum. This 4.4 Kb promoter was obtained as a gift from Gary Struhl (Columbia University, New York, NY). The *pBPw.Act5CP-GCaMP6m* construct was injected by BestGene (Chino Hills, CA. USA) into *Drosophila* using PhiC31 integrase at the attP40 site at 25C6 on Chromosome 2, generating the *ActinP-GCaMP6m* fly line.

***Gbp1*$^{\Delta}$ generation**

The *Gbp1*$^{\Delta}$ null mutant was created by targeting two CRISPR-mediated double-stranded breaks to the *Gbp1* gene locus (www.crisprflydesign.org). The following gRNAs were chosen:

#1) ATTTGCTCCCATCATTTATC

#2) CGGAAAACGATGCAGAAAGC

gRNAs sequences with extensions to allow for BbsI digestion were synthesized as single-stranded DNA oligos and annealed to form overhangs, then ligated to a pCFD5 vector (Addgene, #73914) digested with BbsI (NEB, #R3539S). Both plasmids were sequence-verified then injected by BestGene (Chino Hills, CA. USA) into *vas-Cas9* expressing *Drosophila* embryos (Bloomington Stock 51324). *vas-Cas9* was crossed out of progeny and mutants were identified by PCR for the presence of a *Gbp1* deletion.

On sequencing, *Gbp1*$^{\Delta}$ was found to be missing 282 nucleotides, spanning the coding region corresponding to 94 amino acids from A22 to K116. This includes the C-terminal active peptide of the Gbp1 protein, which spans I95 to A118.

***Gbp2*$^{3\Delta FS}$ generation**

The *Gbp2*$^{3\Delta FS}$ null mutant was created by targeting two CRISPR-mediated double-stranded breaks in the *Gbp2* gene locus, using the protocol above. The following gRNAs were chosen:

#1) GAATATTCAACGCTGCCGTT

#2) AATTCCATACAACCGCGTCC

On sequencing, the *Gbp2*$^{3\Delta FS}$ allele was found to create multiple lesions: 8 missense mutations within the protein coding region generating the following amino acid substitutions: P41S, N42H, V51G, I61N, V94G, P150S, N192I, and S218P. Additionally, 3 small regions were deleted from the protein coding region: 30 nucleotides corresponding to Q236–Q246, 60 nucleotides corresponding to S252–T272, and 128 nucleotides corresponding to G284–R326. The last deletion induced a frameshift, creating multiple missense mutations and 4 stop codons in the final 391 nucleotides of the gene, thus preventing transcription of the region corresponding to the C-terminal active peptide of the Gbp2 protein, which spans S433 to A456.

Figure design

Figures were created in Affinity Designer (Serif (Europe) Ltd, West Bridgford, United Kingdom) and Inkscape (Inkscape.org).

QUANTIFICATION AND STATISTICAL ANALYSIS

Calcium signal intensity analysis

Fluorescence intensity of wing discs was measured using the Measure Stack plug-in in ImageJ. The region of interest was defined around the entire wing disc using the polygon selection tool. The mean fluorescence intensity for each disc was graphed in Microsoft Excel as a function of time, with 0 s corresponding to the frame when calcium activators were added to the wing disc media. The $\Delta F/F_0$ value for each experiment was defined as the disc's fluorescence intensity in the initial frame of the movie subtracted from the disc's maximum intensity, normalized to the initial frame intensity.

Calcium signal radius analysis

To quantify the spread of calcium signals from full-frame time-lapse images (Chapter 4, S6A, A'), the ImageJ Radial Profile Angle Plot plug-in was used on each image to determine the average GCaMP6m intensity profile as a function of distance from the center of the wound (Chapter 4, S6B, B'). A custom MATLAB script was then used to determine the distance from the wound at which the intensity dropped to half its maximum. This distance corresponds to the radius of the radially-averaged calcium wave and plotting radius for each video frame yields a graph of calcium signal expansion over time, which was graphed in Microsoft Excel (Chapter 4, S6A').

The only exception to this applies to the analysis for Chapter 4, 7D–F. Because these images were taken on a different scope, the custom MATLAB script was not optimized to determine radius vs time automatically, so these images were quantified by hand. Different control images were taken for this data-set than the controls in Figure 3, and this may explain any small discrepancies in spatial or temporal response values.

For all movies with an internal control, *pnr>mCherry.NLS* expression was used to define the experimental and control domains (as in Chapter 4, Figure 1B). The average calcium signal

within each domain was measured separately. After plotting calcium radius with respect to time, the Δradius value for each sample was defined as the maximum value of the control domain calcium radius minus the calcium radius of the *pnr*-expressing experimental domain at the same time point (as shown in Chapter 4, Figure 1E').

For movies without an internal control, R_{Max} was defined as the maximum value of the calcium radius and R_{1st} as the value of the calcium radius at the first expansion local maximum. Duration of distal calcium response was defined by the duration the calcium response remained greater than R_{1st}. Movies cut off before the distal calcium response dipped below R_{1st} were excluded from duration analysis. Start time was defined as the time after wounding where the calcium radius value increased for at least three consecutive frames (excluding the first expansion increase). Movies where this never occurred were excluded from start time analysis.

Statistical analysis

All statistical analysis was performed in GraphPad Prism (San Diego, CA. USA). Δradius values for all samples of each genotype were graphed in Prism, and statistical analysis was performed by one-way ANOVA with multiple comparisons of each genotype from Chapter 4, Figure 1, 2, and S1 simultaneously with respect to the control group from Chapter 4, Figure 1I. Values for radius, duration, and start time analyses in Chapter 4, Figure 3G–I and Chapter 4, Figure 7D–F were graphed in Prism and statistical analysis was performed by one-way ANOVA with multiple comparisons with respect to the control group. Similarly, $\Delta F/F_0$ values for all wing disc experiments were graphed in Prism, and statistical analysis was performed by Student's t-test in all cases except for Chapter 4, Figure 5C which was analyzed by two-way ANOVA with multiple comparisons of each genotype with respect to the control extract + control disc group. Each scatterplot displays the value for each sample as a point, with bars representing mean and SEM.

ImageJ analysis of radial zones of damage

The radius of plasma membrane damage was determined as previously described [14,113]. Briefly, the first frame of visible GCaMP6m fluorescence after wounding was used to determine the radius of calcium entry as a proxy for plasma membrane damage. The ImageJ Radial Profile Angle Plot plug-in was used on this image to determine the GCaMP intensity profile as a function of distance from the center of the wound. A custom MATLAB script was then used to determine the distance from the wound at which the intensity dropped to half its maximum. This distance corresponds to the radius of the radially-averaged calcium wave. This same method was applied to each frame in the first 30 seconds following a wound to find the radius of the "first calcium expansion" radius, determined as the maximum radius of GCaMP6m fluorescence within this time-frame.

The radii of all other zones of damage were found by drawing a circular region of interest in ImageJ, then using the "measure" tool in ImageJ to find the area. The radius was calculated based on $A = \pi r^2$. To reduced bias, each dual-channel image was split into separate single-channel images before measuring, ensuring the size of the zone of damage in the red channel does not influence the measurement of the zone of damage in the green channel and vice versa. The zone of "laser-induced rupture" was drawn around the area that has clearly lost mCherry.NLS fluorescence compared to the surrounding punctate nuclei, by the second frame after wounding. The zone of "delayed cell lysis" was drawn around the area that had completely lost all mCherry.NLS fluorescence by 90 seconds following wounding. The zone of "nuclear membrane damage" was drawn around the area that had lost punctate mCherry.NLS fluorescence by 90 seconds following wounding, but still retained diffuse mCherry signal within the cell. The zone of "Ecadherin loss" was drawn around the ring of Ecadherin-GFP that remained around the center of the wound, connected to fully intact cells at 5 minutes after wounding. The zone of "chromatin disruption" was drawn around the zone where Histone-GFP punctae had become disorganized from the rest of the epithelial sheet. Although measurement

of this zone was subjective, in many samples there was a clear delineation between Histone-GFP fluorescence that was disorganized and clumped in the center of the wound compared to organized nuclei that remained intact surrounding the wound.

Equations and confidence intervals for Chapter 3

The linear correlations, including confidence intervals and prediction bands, were found using Microsoft Excel and confirmed in Graphpad Prism. Briefly, the "LINEST" function in Microsoft Excel was used to calculate the linear regression values for the eleven equations presented in Fig 2–5, representing equations 1–11, as well as their inverse functions where the dependent and independent variables were swapped, representing equations 12–22 (S1 Dataset). Equations 1–22 were plotted in Graphpad Prism, with the 95% confidence intervals and 95% single-prediction bands determined automatically in the software. The equations to yield the 95% confidence intervals (i.e., predicted value +/- $CI_{95\%}$) and 95% single-prediction bands (predicted value +/- $SPB_{95\%}$) were confirmed to be the following, as described previously [225,226]:

$$CI_{95\%} = t_{crit} * s_{res} * \sqrt{\frac{1}{n} + \frac{(x - \bar{x})^2}{\sum(x_i - \bar{x})^2}}$$

and

$$SPB_{95\%} = t_{crit} * s_{res} * \sqrt{1 + \frac{1}{n} + \frac{(x - \bar{x})^2}{\sum(x_i - \bar{x})^2}}$$

Where t_{crit} is the critical t value for α=0.05, s_{res} is the standard error of the predicted y for each x is the root-mean-square error of the measured versus predicted y-values, n is the sample size, x is the value of x where the confidence intervals are evaluated, x is the average value of x.

To estimate the extent of one region of damage from any other given region of damage (e.g. Fig 6), some equations were combined together. For example, to determine the radius of

the first calcium expansion from a given radius of laser-induced rupture, equation 3 was combined with equation 7 to yield a new equation 23:

$$PM = m_1 * LR + b_1$$

(Eq 3)

$$1st = m_2 * PM + b_2$$

(Eq 7)

yields:

$$1st = m_2 * m_1 * LR + m_2 * b_1 + b_2$$

(Eq 23)

This method was used to derive equations 23–42, using the most efficient “path” from one known value to one unknown value. In the cases where two combinations of equations were equally valid “paths”, then the two combinations were averaged together. For example, to determine the radius of the Ecadherin loss from a given radius of laser-induced rupture, equation 1 and equation 8 can be combined or equation 2 and equation 9 can be combined. In this case, both were averaged together.

To determine the 95% confidence intervals of Equations 23–42, the uncertainties from each equation were propagated as described previously [227]. Briefly, the partial derivative with respect to each slope and intercept in the final equation was multiplied by the respective 95% confidence interval of the slope or intercept, and these were then summed in quadrature. Using y and x to represent a generic two-step path to calculate y given x, one can calculate the confidence interval of the predicted y-value at each x using:

$$CI_{y,95\%} \approx \sqrt{\left(\frac{\partial y}{\partial m_1}\right)_x^2 \sigma_{m_1}^2 + \left(\frac{\partial y}{\partial m_2}\right)_x^2 \sigma_{m_2}^2 + \left(\frac{\partial y}{\partial b_1}\right)_x^2 \sigma_{b_1}^2 + \left(\frac{\partial y}{\partial b_2}\right)_x^2 \sigma_{b_2}^2}$$

Where each partial derivative is evaluated at x, $\sigma_{m_i}^2$ is the 95% CI of the slope m_i and $\sigma_{b_i}^2$ is the 95% CI of the intercept b_i.

This process yielded the 42 linear equations designed to approximate any of the seven zones of damage from a measurement of any single zone. The supplemental information (of O'Connor et al. PLOS One, 2021)[136] includes an Excel dataset that contains all necessary regression information for all 42 equations (S2 Dataset). Further, it includes individual sheets where a single known radius value can be input for one zone of damage, and the approximate radius and 95% confidence intervals for the other six unknown zones of damage will be automatically calculated (S2 Dataset).

REFERENCES

1. Mandel, L. J., Bacallao, R. & Zampighi, G. Uncoupling of the molecular “fence” and paracellular “gate” functions in epithelial tight junctions. *Nature* 361, 552–555 (1993).

2. Brugués, A. *et al.* Forces driving epithelial wound healing. *Nat Phys* 10, 683–690 (2014).

3. Leoni, G., Neumann, P.-A., Sumagin, R., Denning, T. L. & Nusrat, A. Wound repair: role of immune–epithelial interactions. *Mucosal Immunol* 8, 959–968 (2015).

4. Gurtner, G. C., Werner, S., Barrandon, Y. & Longaker, M. T. Wound repair and regeneration. *Nature* 453, 314–321 (2008).

5. Epstein, F. H., Singer, A. J. & Clark, R. A. F. Cutaneous wound healing. *New Engl J Medicine* 341, 738–46 (1999).

6. Antunes, M., Pereira, T., Cordeiro, J. V., Almeida, L. & Jacinto, A. Coordinated waves of actomyosin flow and apical cell constriction immediately after wounding. *The Journal of cell biology* 202, 365–379 (2013).

7. Razzell, W., Evans, I. R., Martin, P. & Wood, W. Calcium flashes orchestrate the wound inflammatory response through DUOX activation and hydrogen peroxide release. *Current biology : CB* 23, 424–429 (2013).

8. Enyedi, B., Jelcic, M. & Niethammer, P. The Cell Nucleus Serves as a Mechanotransducer of Tissue Damage-Induced Inflammation. *Cell* 165, 1160–1170 (2016).

9. Xu, S. & Chisholm, A. D. A Gαq-Ca^{2+} signaling pathway promotes actin-mediated epidermal wound closure in C. elegans. *Current biology : CB* 21, 1960–1967 (2011).

10. Yoo, S. K., Freisinger, C. M., LeBert, D. C. & Huttenlocher, A. Early redox, Src family kinase, and calcium signaling integrate wound responses and tissue regeneration in zebrafish. *The Journal of cell biology* 199, 225–234 (2012).

11. Hunter, M. V., Willoughby, P. M., Bruce, A. E. E. & Fernandez-Gonzalez, R. Oxidative Stress Orchestrates Cell Polarity to Promote Embryonic Wound Healing. *Developmental cell* 47, 377-387.e4 (2018).

12. Hunter, M. V., Lee, D. M., Harris, T. J. C. & Fernandez-Gonzalez, R. Polarized E-cadherin endocytosis directs actomyosin remodeling during embryonic wound repair. *The Journal of cell biology* 210, 801–816 (2015).

13. Shabir, S. & Southgate, J. Calcium signalling in wound-responsive normal human urothelial cell monolayers. *Cell calcium* 44, 453–464 (2008).

14. Shannon, E. K. *et al.* Multiple Mechanisms Drive Calcium Signal Dynamics around Laser-Induced Epithelial Wounds. *Biophysical journal* 113, 1623–1635 (2017).

15. Stanisstreet, M. Calcium and wound healing in Xenopus early embryos. *Journal of embryology and experimental morphology* 67, 195–205 (1982).

16. Tu, C.-L., Celli, A., Mauro, T. & Chang, W. Calcium-Sensing Receptor Regulates Epidermal Intracellular Ca2+ Signaling and Re-Epithelialization after Wounding. *The Journal of investigative dermatology* 139, 919–929 (2019).

17. Klepeis, V. E., Cornell-Bell, A. & Trinkaus-Randall, V. Growth factors but not gap junctions play a role in injury-induced Ca2+ waves in epithelial cells. *Journal of cell science* 114, 4185–4195 (2001).

18. Clapham, D. E. Calcium signaling. *Cell* 131, 1047–1058 (2007).

19. Berridge, M. J., Lipp, P. & Bootman, M. D. The versatility and universality of calcium signalling. *Nat Rev Mol Cell Bio* 1, 11–21 (2000).

20. Benink, H. A. & Bement, W. M. Concentric zones of active RhoA and Cdc42 around single cell wounds. *The Journal of cell biology* 168, 429–439 (2005).

21. Davenport, N. R., Sonnemann, K. J., Eliceiri, K. W. & Bement, W. M. Membrane dynamics during cellular wound repair. *Molecular biology of the cell* 27, 2272–2285 (2016).

22. McNeil, P. L. & Ito, S. Gastrointestinal Cell Plasma Membrane Wounding and Resealing In Vivo. *Gastroenterology* 96, 1238–1248 (1989).

23. Welch, A. J., Motamedi, M., Rastegar, S., LeCarpentier, G. L. & Jansen, D. Laser Thermal Ablation. *Photochem Photobiol* 53, 815–823 (1991).

24. Hutson, M. S. & Ma, X. Plasma and Cavitation Dynamics during Pulsed Laser Microsurgery in vivo. *Phys Rev Lett* 99, 158104 (2007).

25. Ertel, E. A. *et al.* Nomenclature of Voltage-Gated Calcium Channels. *Neuron* 25, 533–535 (2000).

26. Maricq, A. V., Peterson, A. S., Brake, A. J., Myers, R. M. & Julius, D. Primary Structure And Functional Expression of the 5HT3 Receptor, A Serotonin-gated Ion Channel. *Science* 254, 432–437 (1991).

27. Wu, J., Lewis, A. H. & Grandl, J. Touch, Tension, and Transduction – The Function and Regulation of Piezo Ion Channels. *Trends Biochem Sci* 42, 57–71 (2017).

28. Kim, S. E., Coste, B., Chadha, A., Cook, B. & Patapoutian, A. The role of Drosophila Piezo in mechanical nociception. *Nature* 483, 209–212 (2012).

29. Hehlert, P., Zhang, W. & Göpfert, M. C. Drosophila Mechanosensory Transduction. *Trends Neurosci* 44, 323–335 (2020).

30. Trebak, M. & Putney, J. W. ORAI Calcium Channels. *Physiology* 32, 332–342 (2017).

31. Hogan, P. G. & Rao, A. Store-operated calcium entry: Mechanisms and modulation. *Biochem Bioph Res Co* 460, 40–49 (2015).

32. Lin, S.-Y. & Corey, D. P. TRP channels in mechanosensation. *Curr Opin Neurobiol* 15, 350–357 (2005).

33. Voets, T., Talavera, K., Owsianik, G. & Nilius, B. Sensing with TRP channels. *Nat Chem Biol* 1, 85–92 (2005).

34. Clapham, D. E. TRP channels as cellular sensors. *Nature* 426, 517–524 (2003).

35. Venkatachalam, K. & Montell, C. TRP Channels. *Annu Rev Biochem* 76, 387–417 (2007).

36. Ramsey, I. S., Delling, M. & Clapham, D. E. AN INTRODUCTION TO TRP CHANNELS. *Annu Rev Physiol* 68, 619–647 (2006).

37. Berridge, M. J. Inositol Trisphosphate and Diacylglycerol: Two Interacting Second Messengers. *Annu Rev Biochem* 56, 159–193 (1987).

38. Berridge, M. J. & Galione, A. Cytosolic calcium oscillators. *Faseb J* 2, 3074–3082 (1988).

39. Mikoshiba, K. IP3 receptor/Ca2+ channel: from discovery to new signaling concepts. *J Neurochem* 102, 1426–1446 (2007).

40. Smrcka, A. V., Hepler, J. R., Brown, K. O. & Sternweis, P. C. Regulation of Polyphosphoinositide-specific Phospholipase C Activity by Purified Gq. *Science* 251, 804–807 (1991).

41. Narciso, C. *et al.* Patterning of wound-induced intercellular Ca(2+) flashes in a developing epithelium. *Physical biology* 12, 056005 (2015).

42. Restrepo, S. & Basler, K. Drosophila wing imaginal discs respond to mechanical injury via slow InsP3R-mediated intercellular calcium waves. *Nature communications* 7, 12450–9 (2016).

43. Weinger, I., Klepeis, V. E. & Trinkaus-Randall, V. Tri-nucleotide receptors play a critical role in epithelial cell wound repair. *Purinergic signalling* 1, 281–292 (2005).

44. Newton, A. C. Protein Kinase C: Structure, Function, and Regulation (*). *J Biol Chem* 270, 28495–28498 (1995).

45. Nishizuka, Y. Studies and Perspectives of Protein Kinase C. *Science* 233, 305–312 (1986).

46. Luttrell, L. M., Daaka, Y. & Lefkowitz, R. J. Regulation of tyrosine kinase cascades by G-protein-coupled receptors. *Curr Opin Cell Biol* 11, 177–183 (1999).

47. Rebecchi, M. J. & Pentyala, S. N. Structure, Function, and Control of Phosphoinositide-Specific Phospholipase C. *Physiol Rev* 80, 1291–1335 (2000).

48. Fill, M. & Copello, J. A. Ryanodine Receptor Calcium Release Channels. *Physiol Rev* 82, 893–922 (2002).

49. Coronado, R., Morrissette, J., Sukhareva, M. & Vaughan, D. M. Structure and function of ryanodine receptors. *Am J Physiol-cell Ph* 266, C1485–C1504 (1994).

50. Denda, S. *et al.* Ryanodine Receptors Are Expressed in Epidermal Keratinocytes and Associated with Keratinocyte Differentiation and Epidermal Permeability Barrier Homeostasis. *J Invest Dermatol* 132, 69–75 (2012).

51. Degovics, D. *et al.* A novel target for the promotion of dermal wound healing: Ryanodine receptors. *Toxicol Appl Pharm* 366, 17–24 (2019).

52. Paul, D. L. New functions for gap junctions. *Curr Opin Cell Biol* 7, 665–672 (1995).

53. Sanderson, M. J., Charles, A. C., Boitano, S. & Dirksen, E. R. Mechanisms and function of intercellular calcium signaling. *Mol Cell Endocrinol* 98, 173–187 (1994).

54. Kim, W. T., Rioult, M. G. & Cornell-Bell, A. H. Glutamate-induced calcium signaling in astrocytes. *Glia* 11, 173–184 (1994).

55. Peracchia, C. Chemical gating of gap junction channels Roles of calcium, pH and calmodulin. *Biochimica Et Biophysica Acta Bba - Biomembr* 1662, 61–80 (2004).

56. Jørgensen, N. R., Geist, S. T., Civitelli, R. & Steinberg, T. H. ATP- and Gap Junction–dependent Intercellular Calcium Signaling in Osteoblastic Cells. *J Cell Biology* 139, 497–506 (1997).

57. Charles, A. C. *et al.* Intercellular calcium signaling via gap junctions in glioma cells. *J Cell Biology* 118, 195–201 (1992).

58. Sáez, J. C., Connor, J. A., Spray, D. C. & Bennett, M. V. Hepatocyte gap junctions are permeable to the second messenger, inositol 1,4,5-trisphosphate, and to calcium ions. *Proc National Acad Sci* 86, 2708–2712 (1989).

59. Verkhratsky, A. Physiology and Pathophysiology of the Calcium Store in the Endoplasmic Reticulum of Neurons. *Physiol Rev* 85, 201–279 (2005).

60. Burdakov, D., Petersen, O. H. & Verkhratsky, A. Intraluminal calcium as a primary regulator of endoplasmic reticulum function. *Cell Calcium* 38, 303–310 (2005).

61. BLAUSTEIN, M. P., JUHASZOVA, M., GOLOVINA, V. A., CHURCH, P. J. & STANLEY, E. F. Na/Ca Exchanger and PMCA Localization in Neurons and Astrocytes. *Ann Ny Acad Sci* 976, 356–366 (2002).

62. Guerini, D. The significance of the isoforms of plasma membrane calcium ATPase. *Cell Tissue Res* 292, 191–197 (1998).

63. Quednau, B. D., Nicoll, D. A. & Philipson, K. D. The sodium/calcium exchanger family—SLC8. *Pflügers Archiv* 447, 543–548 (2004).

64. Kiehart, D. P. Wound healing: The power of the purse string. *Curr Biol* 9, R602–R605 (1999).

65. Bement, W. M., Forscher, P. & Mooseker, M. S. A novel cytoskeletal structure involved in purse string wound closure and cell polarity maintenance. *J Cell Biology* 121, 565–578 (1993).

66. Martin, P. & Lewis, J. Actin cables and epidermal movement in embryonic wound healing. *Nature* 360, 179–183 (1992).

67. Abreu-Blanco, M. T., Verboon, J. M., Liu, R., Watts, J. J. & Parkhurst, S. M. Drosophila embryos close epithelial wounds using a combination of cellular protrusions and an actomyosin purse string. *J Cell Sci* 125, 5984–5997 (2012).

68. Wood, W. *et al.* Wound healing recapitulates morphogenesis in Drosophila embryos. *Nature cell biology* 4, 907–912 (2002).

69. Odland, G. & Ross, R. Human wound repair. I. Epidermal regeneration. *J Cell Biology* 39, 135–51 (1968).

70. Jin, M. *et al.* Ca2+-dependent regulation of rho GTPases triggers turning of nerve growth cones. *J Neurosci Official J Soc Neurosci* 25, 2338–47 (2005).

71. Clark, A. G. *et al.* Integration of Single and Multicellular Wound Responses. *Curr Biol* 19, 1389–1395 (2009).

72. Wales, P. *et al.* Calcium-mediated actin reset (CaAR) mediates acute cell adaptations. *eLife* 5, 990 (2016).

73. Yin, J., Xu, K., Zhang, J., Kumar, A. & Yu, F.-S. X. Wound-induced ATP release and EGF receptor activation in epithelial cells. *J Cell Sci* 120, 815–825 (2007).

74. Xu, S. & Chisholm, A. D. C. elegans Epidermal Wounding Induces a Mitochondrial ROS Burst that Promotes Wound Repair. *Dev Cell* 31, 48–60 (2014).

75. Dunnill, C. *et al.* Reactive oxygen species (ROS) and wound healing: the functional role of ROS and emerging ROS-modulating technologies for augmentation of the healing process. *Int Wound J* 14, 89–96 (2017).

76. Witte, M. B. & Barbul, A. Role of nitric oxide in wound repair. *Am J Surg* 183, 406–412 (2002).

77. Schäffer, M. R., Tantry, U., Gross, S. S., Wasserkrug, H. L. & Barbul, A. Nitric Oxide Regulates Wound Healing. *J Surg Res* 63, 237–240 (1996).

78. Rock, K. L., Latz, E., Ontiveros, F. & Kono, H. The Sterile Inflammatory Response. *Annu Rev Immunol* 28, 321–342 (2010).

79. Bianchi, M. E. DAMPs, PAMPs and alarmins: all we need to know about danger. *J Leukocyte Biol* 81, 1–5 (2007).

80. Mezzapelle, R., Venereau, E. & Bianchi, M. E. Stress and Alarmins. Report from the 9th iD&EAs meeting. *Cell Death Dis* 10, 937 (2019).

81. Kono, H. & Rock, K. L. How dying cells alert the immune system to danger. *Nat Rev Immunol* 8, 279–289 (2008).

82. Lotze, M. T. & Tracey, K. J. High-mobility group box 1 protein (HMGB1): nuclear weapon in the immune arsenal. *Nat Rev Immunol* 5, 331–342 (2005).

83. Müller, S. *et al.* The double life of HMGB1 chromatin protein: architectural factor and extracellular signal. *Embo J* 20, 4337–4340 (2001).

84. Kupper, T. S., Deitch, E. A., Baker, C. C. & Wong, W. C. The human burn wound as a primary source of interleukin-1 activity. *Surgery* 100, 409–15 (1986).

85. Sauder, D. N. *et al.* Interleukin-1 enhances epidermal wound healing. *Lymphokine Res* 9, 465–73 (1990).

86. Lim, S. Y., Raftery, M. J., Goyette, J., Hsu, K. & Geczy, C. L. Oxidative modifications of S100 proteins: functional regulation by redox. *J Leukocyte Biol* 86, 577–587 (2009).

87. Lee, K. C. & Eckert, R. L. S100A7 (Psoriasin) – Mechanism of Antibacterial Action in Wounds. *J Invest Dermatol* 127, 945–957 (2007).

88. Turrens, J. F. Mitochondrial formation of reactive oxygen species. *J Physiology* 552, 335–344 (2003).

89. Liou, G.-Y. & Storz, P. Reactive oxygen species in cancer. *Free Radical Res* 44, 479–496 (2010).

90. Niethammer, P., Grabher, C., Look, A. T. & Mitchison, T. J. A tissue-scale gradient of hydrogen peroxide mediates rapid wound detection in zebrafish. *Nature* 459, 996–999 (2009).

91. Burke, J. E. & Dennis, E. A. Phospholipase A2 structure/function, mechanism, and signaling. *J Lipid Res* 50, S237–S242 (2009).

92. Rämet, M., Lanot, R., Zachary, D. & Manfruelli, P. JNK signaling pathway is required for efficient wound healing in Drosophila. *Developmental biology* 241, 145–156 (2002).

93. Bosch, M., Serras, F., Martín-Blanco, E. & Baguñà, J. JNK signaling pathway required for wound healing in regenerating Drosophila wing imaginal discs. *Developmental biology* 280, 73–86 (2005).

94. Losick, V. P., Jun, A. S. & Spradling, A. C. Wound-Induced Polyploidization: Regulation by Hippo and JNK Signaling and Conservation in Mammals. *PloS one* 11, e0151251 (2016).

95. Cosolo, A. *et al.* JNK-dependent cell cycle stalling in G2 promotes survival and senescence-like phenotypes in tissue stress. *eLife* 8, 1169 (2019).

96. Gao, K. *et al.* Traumatic scratch injury in astrocytes triggers calcium influx to activate the JNK/c-Jun/AP-1 pathway and switch on GFAP expression. *Glia* 61, 2063–2077 (2013).

97. Takeda, K. & Akira, S. TLR signaling pathways. *Semin Immunol* 16, 3–9 (2004).

98. Lemaitre, B., Nicolas, E., Michaut, L., Reichhart, J.-M. & Hoffmann, J. A. The Dorsoventral Regulatory Gene Cassette spätzle/Toll/cactus Controls the Potent Antifungal Response in Drosophila Adults. *Cell* 86, 973–983 (1996).

99. Valanne, S., Wang, J.-H. & Rämet, M. The Drosophila Toll signaling pathway. *Journal of immunology (Baltimore, Md. : 1950)* 186, 649–656 (2011).

100. Chasan, R., Jin, Y. & Anderson, K. V. Activation of the easter zymogen is regulated by five other genes to define dorsal-ventral polarity in the Drosophila embryo. *Development* 115, 607–616 (1992).

101. Morisato, D. & Anderson, K. V. The spätzle gene encodes a component of the extracellular signaling pathway establishing the dorsal-ventral pattern of the Drosophila embryo. *Cell* 76, 677–688 (1994).

102. Patterson, R. A. *et al.* Serine Proteolytic Pathway Activation Reveals an Expanded Ensemble of Wound Response Genes in Drosophila. *Plos One* 8, e61773 (2013).

103. Capilla, A. *et al.* Toll pathway is required for wound-induced expression of barrier repair genes in the Drosophila epidermis. *Proc National Acad Sci* 114, E2682–E2688 (2017).

104. Shaw, T. J. & Martin, P. Wound repair at a glance. *J Cell Sci* 122, 3209–3213 (2009).

105. Reinke, J. M. & Sorg, H. Wound Repair and Regeneration. *Eur Surg Res* 49, 35–43 (2012).

106. Macfarlane, R. G. A. The blood clotting mechanism. The development of a theory of blood coagulation. *Proceedings of the Royal Society of London. Series B, Biological sciences* 173, 261–268 (1969).

107. Schmidt, A. Neue Untersuchungen über die Faserstoffgerinnung. *Archiv für die gesamte Physiologie des Menschen und der Tiere* 6, 413–538 (1872).

108. Torbet, J. The thrombin activation pathway modulates the assembly, structure and lysis of human plasma clots in vitro. *Thrombosis and haemostasis* 73, 785–792 (1995).

109. Darby, I. A., Laverdet, B., Bonté, F. & Desmoulière, A. Fibroblasts and myofibroblasts in wound healing. *Clin Cosmet Investigational Dermatology* 7, 301–311 (2014).

110. Park, S. *et al.* Tissue-scale coordination of cellular behaviour promotes epidermal wound repair in live mice. *Nat Cell Biol* 19, 155–163 (2017).

111. Brand, A. H. & Perrimon, N. Targeted gene expression as a means of altering cell fates and generating dominant phenotypes. *Dev Camb Engl* 118, 401–15 (1993).

112. Bainbridge, S. P. & Bownes, M. Staging the metamorphosis of Drosophila melanogaster. *Development* 66, 57–80 (1981).

113. O'Connor, J. T. *et al.* Proteolytic activation of Growth-blocking peptides triggers calcium responses through the GPCR Mthl10 during epithelial wound detection. *Dev Cell* (2021) doi:10.1016/j.devcel.2021.06.020.

114. Kiehart, D. P. *et al.* Cell Biology (Third Edition). *Part Imaging Techniques Sect 3confocal Microsc Living Cells Fixed Cells Sect 3 Confocal Microsc Living Cells Fixed Cells* 87–103 (2006) doi:10.1016/b978-012164730-8/50137-4.

115. Karin, M. & Clevers, H. Reparative inflammation takes charge of tissue regeneration. *Nature* 529, 307–315 (2016).

116. Eming, S. A., Wynn, T. A. & Martin, P. Inflammation and metabolism in tissue repair and regeneration. *Science* 356, 1026–1030 (2017).

117. Thuma, L., Carter, D., Weavers, H. & Martin, P. Drosophila immune cells extravasate from vessels to wounds using Tre1 GPCR and Rho signaling. *The Journal of cell biology* 217, 3045–3056 (2018).

118. Hellman, A. N., Rau, K. R., Yoon, H. H. & Venugopalan, V. Biophysical Response to Pulsed Laser Microbeam-Induced Cell Lysis and Molecular Delivery. *J Biophotonics* 1, 24–35 (2008).

119. McNeil, P. L. & Steinhardt, R. A. Loss, Restoration, and Maintenance of Plasma Membrane Integrity. *J Cell Biology* 137, 1–4 (1997).

120. Gault, W. J., Enyedi, B. & Niethammer, P. Osmotic surveillance mediates rapid wound closure through nucleotide release. *J Cell Biol* 207, 767–782 (2014).

121. Enyedi, B. & Niethammer, P. Mechanisms of epithelial wound detection. *Trends Cell Biol* 25, 398–407 (2015).

122. Stramer, B. *et al.* Live imaging of wound inflammation in Drosophila embryos reveals key roles for small GTPases during in vivo cell migration. *The Journal of cell biology* 168, 567–573 (2005).

123. Ma, Y., Xie, J., Wijaya, C. S. & Xu, S. From wound response to repair – lessons from C. elegans. *Cell Regen* 10, 5 (2021).

124. Richardson, R. *et al.* Adult Zebrafish as a Model System for Cutaneous Wound-Healing Research. *J Invest Dermatol* 133, 1655–1665 (2013).

125. Troutman, R. C., Véronneau-Troutman, S., Jakobiec, F. A. & Krebs, W. A new laser for collagen wounding in corneal and strabismus surgery: a preliminary report. *T Am Ophthal Soc* 84, 117–32 (1986).

126. Leeuwen, T. G. V., Jansen, E. D., Motamedi, M., Borst, C. & Welch, A. J. Optical-Thermal Response of Laser-Irradiated Tissue. 709–763 (1995) doi:10.1007/978-1-4757-6092-7_21.

127. Venugopalan, V., Guerra, A., Nahen, K. & Vogel, A. Role of Laser-Induced Plasma Formation in Pulsed Cellular Microsurgery and Micromanipulation. *Phys Rev Lett* 88, 078103 (2002).

128. Galko, M. J. & Krasnow, M. A. Cellular and Genetic Analysis of Wound Healing in Drosophila Larvae. *Plos Biol* 2, e239 (2004).

129. Burra, S., Wang, Y., Brock, A. R. & Galko, M. J. Wound Regeneration and Repair, Methods and Protocols. *Methods Mol Biology* 1037, 449–461 (2013).

130. Wu, Y. *et al.* A blood-borne PDGF/VEGF-like ligand initiates wound-induced epidermal cell migration in Drosophila larvae. *Current biology : CB* 19, 1473–1477 (2009).

131. Ramos-Lewis, W., LaFever, K. S. & Page-McCaw, A. A scar-like lesion is apparent in basement membrane after wound repair in vivo. *Matrix Biol* 74, 101–120 (2018).

132. Martin, P., Nobes, C., McCluskey, J. & Lewis, J. Repair of excisional wounds in the embryo. *Eye* 8, 155–160 (1994).

133. McNeil, P. L. & Ito, S. Molecular traffic through plasma membrane disruptions of cells in vivo. *J Cell Sci* 96 (Pt 3), 549–56 (1990).

134. Vogel, A. & Venugopalan, V. Mechanisms of Pulsed Laser Ablation of Biological Tissues. *Cheminform* 34, (2003).

135. Matsubayashi, Y., Coulson-Gilmer, C. & Millard, T. H. Endocytosis-dependent coordination of multiple actin regulators is required for wound healing. *J Cell Biol* 210, 419–433 (2015).

136. O'Connor, J., Akbar, F. B., Hutson, M. S. & Page-McCaw, A. Zones of cellular damage around pulsed-laser wounds. *Plos One* 16, e0253032 (2021).

137. Ponte, S. *et al.* Drp1-mediated mitochondrial fission regulates calcium and F-actin dynamics during wound healing. *Biol Open* 9, bio048629 (2020).

138. Franz, A., Wood, W. & Martin, P. Fat Body Cells Are Motile and Actively Migrate to Wounds to Drive Repair and Prevent Infection. *Developmental cell* 44, 460-470.e3 (2018).

139. Davidson, A. J. & Wood, W. Phagocyte Responses to Cell Death in Flies. *Csh Perspect Biol* 12, a036350 (2019).

140. Westman, J., Grinstein, S. & Marques, P. E. Phagocytosis of Necrotic Debris at Sites of Injury and Inflammation. *Front Immunol* 10, 3030 (2020).

141. Danjo, Y. & Gipson, I. K. Specific Transduction of the Leading Edge Cells of Migrating Epithelia Demonstrates That They are Replaced During Healing. *Exp Eye Res* 74, 199–204 (2002).

142. Radice, G. P. The spreading of epithelial cells during wound closure in Xenopus larvae. *Dev Biol* 76, 26–46 (1980).

143. McNeil, P. L. & Steinhardt, R. A. Plasma membrane disruption: repair, prevention, adaptation. *Annual review of cell and developmental biology* 19, 697–731 (2003).

144. Hander, T. *et al.* Damage on plants activates Ca2+-dependent metacaspases for release of immunomodulatory peptides. *Science (New York, N.Y.)* 363, eaar7486 (2019).

145. Levy, H. M. & Ryan, E. M. Evidence that calcium activates the contraction of actomyosin by overcoming substrate inhibition. *Nature* 205, 703–705 (1965).

146. Kong, D. *et al.* In vivo optochemical control of cell contractility at single-cell resolution. *EMBO reports* 20, e47755 (2019).

147. Gomes, P., Malfait, M., Himpens, B. & Vereecke, J. Intercellular Ca(2+)-transient propagation in normal and high glucose solutions in rat retinal epithelial (RPE-J) cells during mechanical stimulation. *Cell calcium* 34, 185–192 (2003).

148. D'hondt, C., Himpens, B. & Bultynck, G. Mechanical stimulation-induced calcium wave propagation in cell monolayers: the example of bovine corneal endothelial cells. *Journal of visualized experiments : JoVE* e50443 (2013) doi:10.3791/50443.

149. Narciso, C. E., Contento, N. M., Storey, T. J., Hoelzle, D. J. & Zartman, J. J. Release of Applied Mechanical Loading Stimulates Intercellular Calcium Waves in Drosophila Wing Discs. *Biophysical journal* 113, 491–501 (2017).

150. Balaji, R. *et al.* Calcium spikes, waves and oscillations in a large, patterned epithelial tissue. *Scientific reports* 7, 42786–14 (2017).

151. Hanlon, C. D. & Andrew, D. J. Outside-in signaling--a brief review of GPCR signaling with a focus on the Drosophila GPCR family. *Journal of cell science* 128, 3533–3542 (2015).

152. Chang-Graham, A. L. *et al.* Rotavirus induces intercellular calcium waves through ADP signaling. *Science (New York, N.Y.)* 370, eabc3621 (2020).

153. Yang, L. *et al.* Substance P promotes diabetic corneal epithelial wound healing through molecular mechanisms mediated via the neurokinin-1 receptor. *Diabetes* 63, 4262–4274 (2014).

154. Sung, E. J. *et al.* Cytokine signaling through Drosophila Mthl10 ties lifespan to environmental stress. *Proceedings of the National Academy of Sciences of the United States of America* 114, 13786–13791 (2017).

155. Tsuzuki, S. *et al.* Drosophila growth-blocking peptide-like factor mediates acute immune reactions during infectious and non-infectious stress. *Scientific reports* 2, 210–10 (2012).

156. Hayakawa, Y. Structure of a growth-blocking peptide present in parasitized insect hemolymph. *The Journal of biological chemistry* 266, 7982–7984 (1991).

157. Endo, Y., Ohnishi, A. & Hayakawa, Y. Mechanism of parasitism-induced elevation of haemolymph growth-blocking peptide levels in host insect larvae (Pseudaletia separata). *Journal of insect physiology* 44, 859–866 (1998).

158. Shears, S. B. & Hayakawa, Y. Functional Multiplicity of an Insect Cytokine Family Assists Defense Against Environmental Stress. *Frontiers in physiology* 10, 222 (2019).

159. Matsumoto, Y., Oda, Y., Uryu, M. & Hayakawa, Y. Insect cytokine growth-blocking peptide triggers a termination system of cellular immunity by inducing its binding protein. *The Journal of biological chemistry* 278, 38579–38585 (2003).

160. Koyama, T. & Mirth, C. K. Growth-Blocking Peptides As Nutrition-Sensitive Signals for Insulin Secretion and Body Size Regulation. *PLoS biology* 14, e1002392 (2016).

161. Gasteiger, E. *et al.* ExPASy: The proteomics server for in-depth protein knowledge and analysis. *Nucleic acids research* 31, 3784–3788 (2003).

162. Guruharsha, K. G. *et al.* A Protein Complex Network of Drosophila melanogaster. *Cell* 147, 690–703 (2011).

163. Gutenkunst, R. N. *et al.* Universally sloppy parameter sensitivities in systems biology models. *PLoS computational biology* 3, 1871–1878 (2007).

164. Frank, D. & Vince, J. E. Pyroptosis versus necroptosis: similarities, differences, and crosstalk. *Cell Death Differ* 26, 99–114 (2019).

165. Arcuino, G. *et al.* Intercellular calcium signaling mediated by point-source burst release of ATP. *Proc National Acad Sci* 99, 9840–9845 (2002).

166. Boucher, I., Rich, C., Lee, A., Marcincin, M. & Trinkaus-Randall, V. The P2Y2 receptor mediates the epithelial injury response and cell migration. *Am J Physiol-cell Ph* 299, C411–C421 (2010).

167. Sieger, D., Moritz, C., Ziegenhals, T., Prykhozhij, S. & Peri, F. Long-Range Ca2+ Waves Transmit Brain-Damage Signals to Microglia. *Dev Cell* 22, 1138–1148 (2012).

168. Zimmermann, H., Zebisch, M. & Sträter, N. Cellular function and molecular structure of ecto-nucleotidases. *Purinerg Signal* 8, 437–502 (2012).

169. Bement, W. M., Mandato, C. A. & Kirsch, M. N. Wound-induced assembly and closure of an actomyosin purse string in Xenopus oocytes. *Curr Biol* 9, 579–587 (1999).

170. Tsuzuki, S. *et al.* Switching between humoral and cellular immune responses in Drosophila is guided by the cytokine GBP. *Nat Commun* 5, 4628 (2014).

171. Cvejic, S., Zhu, Z., Felice, S. J., Berman, Y. & Huang, X.-Y. The endogenous ligand Stunted of the GPCR Methuselah extends lifespan in Drosophila. *Nat Cell Biol* 6, 540–546 (2004).

172. Lin, Y.-J., Seroude, L. & Benzer, S. Extended Life-Span and Stress Resistance in the *Drosophila* Mutant *methuselah*. *Science* 282, 943–946 (1998).

173. McCay, C. M., Crowell, M. F. & Maynard, L. A. The Effect of Retarded Growth Upon the Length of Life Span and Upon the Ultimate Body Size. *J Nutrition* 10, 63–79 (1935).

174. Gredilla, R. & Barja, G. Minireview: The Role of Oxidative Stress in Relation to Caloric Restriction and Longevity. *Endocrinology* 146, 3713–3717 (2005).

175. Franceschi, C., Garagnani, P., Vitale, G., Capri, M. & Salvioli, S. Inflammaging and 'Garb-aging.' *Trends Endocrinol Metabolism* 28, 199–212 (2017).

176. Zeng, Y. *et al.* Novel loci and pathways significantly associated with longevity. *Sci Rep-uk* 6, 21243 (2016).

177. Bergsbaken, T., Fink, S. L. & Cookson, B. T. Pyroptosis: host cell death and inflammation. *Nature reviews. Microbiology* 7, 99–109 (2009).

178. Fink, S. L. & Cookson, B. T. Apoptosis, pyroptosis, and necrosis: mechanistic description of dead and dying eukaryotic cells. *Infection and immunity* 73, 1907–1916 (2005).

179. Fantuzzi, G. & Dinarello, C. A. Interleukin-18 and interleukin-1 beta: two cytokine substrates for ICE (caspase-1). *Journal of clinical immunology* 19, 1–11 (1999).

180. Beloshistov, R. E. *et al.* Phytaspase-mediated precursor processing and maturation of the wound hormone systemin. *New Phytol* 218, 1167–1178 (2018).

181. Lemon, G., Gibson, W. G. & Bennett, M. R. Metabotropic receptor activation, desensitization and sequestration-I: modelling calcium and inositol 1,4,5-trisphosphate dynamics following receptor activation. *Journal of theoretical biology* 223, 93–111 (2003).

182. Girard, S., Lückhoff, A., Lechleiter, J., Sneyd, J. & Clapham, D. Two-dimensional model of calcium waves reproduces the patterns observed in Xenopus oocytes. *Biophys J* 61, 509–517 (1992).

183. Lechleiter, J., Girard, S., Peralta, E. & Clapham, D. Spiral Calcium Wave Propagation and Annihilation in Xenopus laevis Oocytes. *Science* 252, 123–126 (1991).

184. Bonnet, I. *et al.* Mechanical state, material properties and continuous description of an epithelial tissue. *J Roy Soc Interface* 9, 2614–2623 (2012).

185. Rauzi, M., Verant, P., Lecuit, T. & Lenne, P.-F. Nature and anisotropy of cortical forces orienting Drosophila tissue morphogenesis. *Nat Cell Biol* 10, 1401–1410 (2008).

186. Sugimura, K., Lenne, P.-F. & Graner, F. Measuring forces and stresses in situ in living tissues. *Development* 143, 186–196 (2016).

187. Ma, X., Lynch, H. E., Scully, P. C. & Hutson, M. S. Probing embryonic tissue mechanics with laser hole drilling. *Phys Biol* 6, 036004 (2009).

188. Dekraker, C., Boucher, E. & Mandato, C. A. Regulation and Assembly of Actomyosin Contractile Rings in Cytokinesis and Cell Repair. *Anatomical Rec* 301, 2051–2066 (2018).

189. Millard, T. H. & Martin, P. Dynamic analysis of filopodial interactions during the zippering phase of Drosophila dorsal closure. *Development* 135, 621–626 (2008).

190. Martin, P. & Parkhurst, S. M. Parallels between tissue repair and embryo morphogenesis. *Development* 131, 3021–3034 (2004).

191. Weavers, H., Evans, I. R., Martin, P. & Wood, W. Corpse Engulfment Generates a Molecular Memory that Primes the Macrophage Inflammatory Response. *Cell* 165, 1658–1671 (2016).

192. Zielke, N. *et al.* Fly-FUCCI: A Versatile Tool for Studying Cell Proliferation in Complex Tissues. *Cell Reports* 7, 588–598 (2014).

193. Losick, V. P., Fox, D. T. & Spradling, A. C. Polyploidization and cell fusion contribute to wound healing in the adult Drosophila epithelium. *Current biology : CB* 23, 2224–2232 (2013).

194. Losick, V. P. Wound-Induced Polyploidy Is Required for Tissue Repair. *Adv Wound Care* 5, 271–278 (2016).

195. Cao, J. *et al.* Tension Creates an Endoreplication Wavefront that Leads Regeneration of Epicardial Tissue. *Dev Cell* 42, 600-615.e4 (2017).

196. Fox, D. T. & Duronio, R. J. Endoreplication and polyploidy: insights into development and disease. *Development* 140, 3–12 (2012).

197. Holz, A., Bossinger, B., Strasser, T., Janning, W. & Klapper, R. The two origins of hemocytes in Drosophila. *Development* 130, 4955–4962 (2003).

198. Hoffmann, J. A. & Reichhart, J.-M. Drosophila innate immunity: an evolutionary perspective. *Nat Immunol* 3, 121–126 (2002).

199. Lavine, M. D. & Strand, M. R. Insect hemocytes and their role in immunity. *Insect Biochem Molec* 32, 1295–1309 (2002).

200. Sorrentino, R. P., Carton, Y. & Govind, S. Cellular Immune Response to Parasite Infection in the Drosophila Lymph Gland Is Developmentally Regulated. *Dev Biol* 243, 65–80 (2002).

201. Williams, M. J. Drosophila Hemopoiesis and Cellular Immunity. *J Immunol* 178, 4711–4716 (2007).

202. Moreira, S., Stramer, B., Evans, I., Wood, W. & Martin, P. Prioritization of Competing Damage and Developmental Signals by Migrating Macrophages in the Drosophila Embryo. *Curr Biol* 20, 464–470 (2010).

203. Vogel, A. Nonlinear absorption: intraocular microsurgery and laser lithotripsy. *Phys Med Biol* 42, 895–912 (1997).

204. Ryan, B. J. & Henehan, G. T. Avoiding Proteolysis During Protein Purification. *Methods Mol Biology Clifton N J* 1485, 53–69 (2017).

205. Wood, W., Faria, C. & Jacinto, A. Distinct mechanisms regulate hemocyte chemotaxis during development and wound healing in Drosophila melanogaster. *J Cell Biology* 173, 405–416 (2006).

206. Bootman, M. D. Calcium Signaling. *Csh Perspect Biol* 4, a011171 (2012).

207. Domínguez, D. C., Guragain, M. & Patrauchan, M. Calcium binding proteins and calcium signaling in prokaryotes. *Cell Calcium* 57, 151–165 (2015).

208. Wright, S. H. Generation of resting membrane potential. *Adv Physiol Educ* 28, 139–142 (2004).

209. Rusnak, F. & Mertz, P. Calcineurin: Form and Function. *Physiol Rev* 80, 1483–1521 (2000).

210. Hemenway, C. S. & Heitman, J. Calcineurin. Structure, function, and inhibition. *Cell Biochem Biophys* 30, 115–51 (1999).

211. Klee, C. B. & Vanaman, T. C. Advances in Protein Chemistry Volume 35. *Adv Protein Chem* 35, 213–321 (1982).

212. Chin, D. & Means, A. R. Calmodulin: a prototypical calcium sensor. *Trends Cell Biol* 10, 322–328 (2000).

213. Berridge, M. J. Inositol trisphosphate and calcium signalling. *Nature* 361, 315–325 (1993).

214. Clapham, D. E. Calcium signaling. *Cell* 80, 259–268 (1995).

215. Krysko, D. V., Leybaert, L., Vandenabeele, P. & D'Herde, K. Gap junctions and the propagation of cell survival and cell death signals. *Apoptosis* 10, 459–469 (2005).

216. Shafee, T. M. A., Lay, F. T., Phan, T. K., Anderson, M. A. & Hulett, M. D. Convergent evolution of defensin sequence, structure and function. *Cell Mol Life Sci* 74, 663–682 (2017).

217. Flock, T. *et al.* Selectivity determinants of GPCR–G-protein binding. *Nature* 545, 317–322 (2017).

218. Vlisidou, I. & Wood, W. Drosophila blood cells and their role in immune responses. *Febs J* 282, 1368–1382 (2015).

219. Usui-Aoki, K. *et al.* Targeted expression of Ip3 sponge and Ip3 dsRNA impaires sugar taste sensation in Drosophila. *Journal of neurogenetics* 19, 123–141 (2005).

220. Ogura, Y., Wen, F.-L., Sami, M. M., Shibata, T. & Hayashi, S. A Switch-like Activation Relay of EGFR-ERK Signaling Regulates a Wave of Cellular Contractility for Epithelial Invagination. *Dev Cell* 46, 162-172.e5 (2018).

221. Brodskiy, P. A. *et al.* Decoding Calcium Signaling Dynamics during Drosophila Wing Disc Development. *Biophysical journal* 116, 725–740 (2019).

222. Currie, D. A., Milner, M. J. & Evans, C. W. The growth and differentiation in vitro of leg and wing imaginal disc cells from Drosophila melanogaster. *Development* 102, 805 (1988).

223. Chen, T.-W. *et al.* Ultrasensitive fluorescent proteins for imaging neuronal activity. *Nature* 499, 295–300 (2013).

224. Struhl, G. & Basler, K. Organizing activity of wingless protein in Drosophila. *Cell* 72, 527–540 (1993).

225. Altman, D. G. & Gardner, M. J. Statistics in Medicine: Calculating confidence intervals for regression and correlation. *Br Medical J Clin Res Ed* 296, 1238 (1988).

226. Armitage, P., Berry, G. & Matthews, J. N. S. Statistical Methods in Medical Research, Fourth Edition. 187–207 (2008) doi:10.1002/9780470773666.ch7.

227. Ku, H. H. Notes on the use of propagation of error formulas. *J Res National Bureau Stand Sect C Eng Instrum* 70C, 263 (1966).